OBSERVATION OF ATMOSPHERIC CARBON MONOXIDE BY GROUND-BASED FTIR SPECTROMETER OVER ADDIS ABABA, ETHIOPIA

By

Gezahegn Sufa Daba

SUBMITTED IN PARTIAL FULFILLMENT OF THE
REQUIREMENTS FOR THE DEGREE OF
MASTER OF SCIENCE IN PHYSICS
AT
ADDIS ABABA UNIVERSITY
ADDIS ABABA, ETHIOPIA
JULY 2010

ADDIS ABABA UNIVERSITY
DEPARTMENT OF
PHYSICS

Supervisor: ______________________________
DR. GIZAW MENGISTU

Examiners: ______________________________
PROF. A.V.GHOLAP

____
DR. FELEKE ZEWGE

ADDIS ABABA UNIVERSITY

Date: **JULY 2010**

Author: **Gezahegn Sufa Daba**

Title: **Observation of Atmospheric Carbon monoxide by Ground-based FTIR Spectrometer over Addis Ababa, Ethiopia**

Department: **Physics**

Degree: **M.Sc.** Convocation: **JULY** Year: **2010**

Signature of Author

Table of Contents

List of Figures

Abstract

In this thesis tropospheric and stratospheric CO have been derived from FTIR spectrometer and analyzed since May 17, 2009. All the sources of error indicate that it is not too much to cause significant error in our result. The degree of freedom (DOFs) for CO is nearly 3 which means there are about 3 independent pieces of information from the measurement. The measurement is more sensitive to lower atmosphere than upper atmosphere. The minimum and maximum mixing ratio of CO in the troposphere have been observed in November 2009 and January 2010 respectively while the stratosphere CO VMR is minimum in May 2009 and maximum in February 2010. Inter-annual variation has been detected through a relative increase in CO VMR of May 2010 compared to May 2009. Our results have also shown that the enhancement of O_3 in conjunction with the enhancement of CO is associated with plumes in the upper troposphere on December 08, 2009. While stratosphere-troposphere exchange contributed to the enhancement of O_3 in the upper troposphere when lowest CO VMR is seen on January 21, 2010.

Acknowledgements

Above all, I would like to thank the almighty; God, for letting me accomplish this stage.

I am deeply indebted Dr. Gizaw Mengistu, my advisor, for his suggestions and support during this research. His tireless follow up and his support to his students is unforgettable.

I would also like to thank IMK (Karlsruhe Institute of Meteorology and Climate) particularly to Dr. Frank Hase and Dr. Thomas Blumenstock for helping me to handle the software.

I am also thankful to Habtamu Giday for his patient support in sending me journals.

The last but not the least thanks goes to my parents, especially to my mother who strongly supported me during the research.

Chapter 1

Introduction

Remote sensing is a very powerful tool to investigate our environment. It is the science of acquiring information about a particular target without being in contact with it, in a non-invasive manner. This is done by analyzing the influence of the target on the radiant energy passing through it, emitted or reflected by it. The identification of the nature of the target and the characterization of its composition is ensured by means of spectroscopy. It is also widely used in deriving atmospheric parameters, such as temperature, pressure and concentration of trace gas based on direct measurement of radiation emitted, absorbed and scattered by the atmosphere. The retrieval of atmospheric parameters from remote sensing data requires accurate calculations and determination of the received radiation for specific atmospheric conditions, since the sensor measures complicated functions of interest. These measurements do not give the actual state of the atmosphere with independent errors, but only the best estimate derivable from the measurement and prior knowledge about the state of the parameter. To analyze such atmospheric spectra requires reference spectroscopic information, allowing to know which species is detected (position in the spectra) and its concentration (intensity of the absorption). Such spectroscopic information is obtained in the laboratory by means of high resolution absorption spectroscopy in the gas phase. It is gathered in spectroscopic databases such as HITRAN (HIgh resolution TRANsmission molecular absorption database)[1].

As a rule, the sources of trace elements are found on the surface of the earth. From there, they reach the atmosphere and its systems of motion characterized by wind and turbulent exchange which distribute them in horizontal and vertical directions. They originate from soil erosion of rock material and sea spray which become air borne by atmospheric turbulence, smoke produced in natural fires, emission of volcanic gases and entrainment of biological products. Artificial sources related to the development of human civilization, are added to these natural sources. Today artificial sources in some cases significantly exceeded that of natural sources. In addition, the world wide population is on the increase, this rate of increase is accompanied by the fear that energy requirements and emission levels will rise. A wide range of chemicals can pollute the air, but the ones generally viewed as needing control measures are CO, SO_2, toxic organic, particulate, nitrogen oxides and volcanic compounds. The first four directly harm human welfare[2].

Although CO occurs naturally in the environment, it is an asphyxiating poison because it can displace the oxygen bound to the hemoglobin. If the concentration of CO inhaled by an individual is high it may result in headaches, shortness of breath, loss of consciousness, heart problems. CO also affects the radiative forcing by its influence on the concentrations of greenhouse gases such as CH_4 and O_3. Another source of anthropogenic CO is automotive transport. Individuals may be at greater risk of CO poisoning from malfunctioning stoves and space heaters in their homes. CO is produced whenever combustion is incomplete. The problem is particularly acute in poor countries where unvented and inefficient stoves are common[3].

Hence with the progress in the atmospheric research, it became apparent that precise quantitative measurements of chemical species present in the atmosphere are required in view of the many challenges encountered in modern era. In particular measurements of trace gases such as CO from space borne or ground-based instrument now a days become major objective of environmental research institution. Space borne measurements providing global observation of CO are highly valuable to infer its natural and anthropogenic sources. Ground-based FTIR is one of several instruments that provide accurate measurements of total column of many atmospheric species. In addition, it has been demonstrated by several research groups that high resolution infrared spectrometers with the ability to determine the concentration of many species simultaneously have important advantages compared to other techniques. Thus, high resolution FTIR spectroscopy has developed to an extremely valuable tool for the study of atmospheric chemistry[4].

The Network for the Detection of Atmospheric Composition Change (NDACC) is a worldwide network of observatories, for which primary objectives are to monitor the evolution of the atmospheric composition and structure, and to provide independent data for the validation of numerical models of the atmosphere and of satellite data[5]. NDACC also supports field campaigns focusing on specific processes at various latitudes and seasons. The composition of the tropical atmosphere and its changes over time are of significant importance for global climate. Currently large uncertainties in the budgets of many trace gases in the tropics exist, mainly due to a lack of measurements. Only a few stations in NDACC are situated in the tropical and subtropical belts. In particular, the only tropical NDACC stations at which FTIR measurements are performed are Mauna Loa (19.54°N, 155.6°W, 3459m a.s.l.) and Paramaribo (5.8° N, 55.2° W), both in the Northern Hemisphere[6]. To fill this gap we have recently installed FTIR instrument supplied by IMK-FZK (Institute of Metrology and Climate research center), Germany. The instrument is the first of its kind not only in Ethiopia but also in Africa. The spectrometer is located in AAU, Science Faculty ($9.01°N$ and $38.76°E$) at an altitude of 2443m above sea level.

The main objective of this thesis is to determine the partial and total column amount, and mixing ratio of carbon monoxide over Ethiopia, particularly Addis Ababa, by using high resolution FTIR. Moreover, analysis of CO time series, chemical and dynamical sources and sinks are investigated. In addition, the accuracy of derived CO is characterized by the vertical resolution and sensitivity of the retrieval.

The thesis is divided into nine chapters. In the second chapter there will be general discussion of the atmosphere and then followed by source and sinks of atmospheric CO in chapter three. There is a discussion of the absorption and emission of radiation in the fourth chapter. The fifth chapter deals with the instrumentation. This is followed by the radiative transfer in chapter six and retrieval theory in chapter seven. Finally result and discussion in chapter eight and conclusion in chapter five are given.

Chapter 2

The Atmosphere

2.1 Basic Quantities

In this paper we will use three principal measures of atmospheric composition: mixing ratio, number density, and partial pressure.

Mixing ratio in atmospheric chemistry is defined as the ratio of the amount (or mass) of the substance in a given volume to the total amount (or mass) of all constituents in that volume. The volume mixing ratio (VMR) for a species i is:

$$VMR = p_i/p \tag{2.1.1}$$

where pi is the partial pressure of species i and p is the sum the partial pressure of all constituents including water. Mixing ratios of trace gases are commonly given in units of parts per million by volume (ppmv), parts per billion by volume (ppbv), or parts per trillion by volume (pptv).

The number density n_i of a a species i is the number of molecules of i per unit volume of air. The degree of absorption or scattering depends on the number of molecules of gas along the path of the beam and therefore on the number density of the gas. Consider the atmosphere as extending from the Earths surface (z = 0) up to a certain top height (z = z_T) above which number densities are assumed negligibly small. Thus the integral over the depth of the atmosphere defines the atmospheric column of the gas as:

$$Column = \int_0^{z_T} n_i dZ \tag{2.1.2}$$

This atmospheric column determines the total efficiency with which the gas absorbs or scatters light passing through the atmosphere. The number density and the mixing ratio C_i of a gas are related by the number density of air n_a (molecules of air per cm^3 of air):

$$n_i = C_i n_a \tag{2.1.3}$$

Using this and the hydrostatic balance equation number density of altitude is given by

$$n_a(z) = n_a(0)e^{-z/H} \tag{2.1.4}$$

where $n_a(0) = 2.55 \times 10^{19} molecules cm^{-3}$ is the number density at the surface and H=RT/M_ag is the scale height.

The partial pressure P_i of a species i in a mixture of gases of total pressure P is defined as the pressure that would be exerted by the molecules i if all the other gases were removed from the mixture. Daltons law states that P_i is related to P by the mixing ratio C_i:

$$P_i = C_i P \tag{2.1.5}$$

For our applications, P is the total atmospheric pressure.

2.2 The Composition of the Atmospheric

The atmosphere is composed of a mixture of gases in the proportions shown in Table 5.1. As can be seen diatomic nitrogen (N_2) and oxygen (O_2) are the dominant constituents of the Earth's atmosphere approaching almost 99% by mass as well as by volume. Their compositions vary little with time, so they are treated as permanent gases. Argon (Ar)

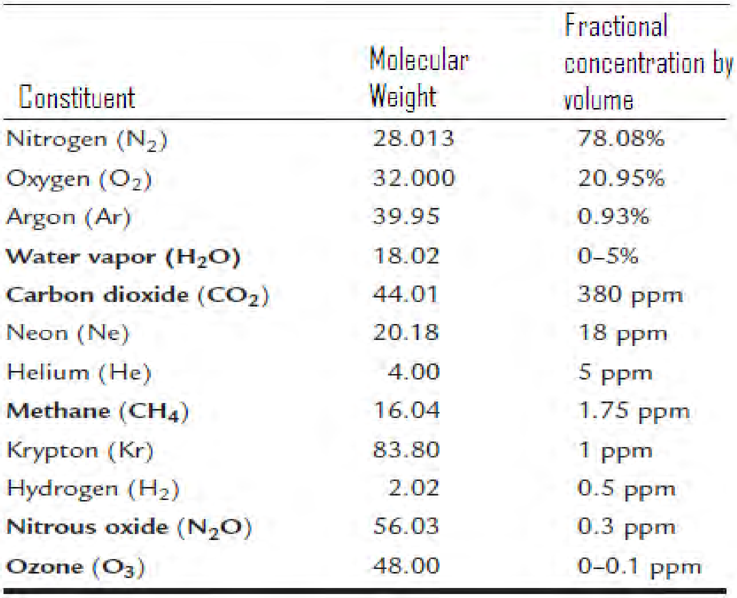

Constituent	Molecular Weight	Fractional concentration by volume
Nitrogen (N_2)	28.013	78.08%
Oxygen (O_2)	32.000	20.95%
Argon (Ar)	39.95	0.93%
Water vapor (H_2O)	18.02	0–5%
Carbon dioxide (CO_2)	44.01	380 ppm
Neon (Ne)	20.18	18 ppm
Helium (He)	4.00	5 ppm
Methane (CH_4)	16.04	1.75 ppm
Krypton (Kr)	83.80	1 ppm
Hydrogen (H_2)	2.02	0.5 ppm
Nitrous oxide (N_2O)	56.03	0.3 ppm
Ozone (O_3)	48.00	0–0.1 ppm

Table 2.1: Fractional concentrations by volume of the major gaseous constituents of the Earths atmosphere up to an altitude of 105 km, with respect to dry air Fractional

is present in much higher concentrations than the other noble gases (neon, helium, krypton, and xenon). Water vapor, carbon dioxide, and ozone are greenhouse gases which are highly effective at trapping outgoing radiation. Though they occur in small proportions, play very important roles in atmospheric processes because of their radiative and thermodynamic properties. Trace constituents CH_4, N_2O, CO, and chlorofluorocarbons (CFCs) are also significant contributors to the greenhouse effect. These gases enter the atmosphere through the burning of plant matter and fossil fuels, emissions from plants, and the decay of plants and animals. The chemical transformations that remove these chemicals from the atmosphere involve oxidation, with the hydroxyl (OH) radical playing an important role. Some of the nitrogen and sulfur compounds are converted into particles that are eventually scavenged by raindrops, which contribute to acid deposition at the Earths surface[7].

Water vapor is a highly variable constituent, with concentrations ranging from around 10 parts per million by volume (ppmv) in the coldest regions of the Earths atmosphere up to as much as 5% by volume in hot, humid air masses; a range of more than three orders of magnitude. Because of the large variability of water vapor concentrations in air, it is customary to list the percentages of the various constituents in relation to dry air. The presence of water in the atmosphere is especially important, because it can exist in three phases: vapour, liquid and solid. A change of phase involves either liberation or absorption of a large quantity of heat which affects atmospheric properties and behaviour[8].

2.3 The Vertical Structure of the Atmosphere

The vertical structure of the atmosphere can be determined as follows. Consider Fig.1.1 which depicts a vertical column of air of horizontal cross sectional area δA and height δz. If the pressure at the bottom of the cylinder is p_B, then that at the top is

$$\begin{aligned} p_T &= p(z+\delta z) \\ &= p(z)+\delta p \end{aligned}$$

where δp is the change in pressure moving from z to $z+\delta z$. Assuming δz to be small,

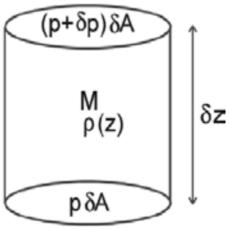

Figure 2.1: Vertical column of air of density ρ, horizontal cross-sectional area δA, height δz and mass M

$$\delta p = \frac{\partial p}{\partial z}\delta z$$

If the cylinder of air is not accelerating, it must be subjected to zero net force. Setting the net force to zero gives $\delta p + g\rho\delta z = 0$ which leads to [13]:

$$\frac{\partial p}{\partial z} + g\rho = 0 \tag{2.3.1}$$

Eq.(2.3.1) is the equation of hydrostatic balance[9]. It describes how pressure decreases with height in proportion to the weight of the overlying atmosphere. But it does not tell us what p(z) is, since we do not know a priori what $\rho(z)$ is. In order to determine p(z) we must use an equation of state to establish the connection between ρ and p, as described in the next section.

2.3.1 Vertical Structure of Pressure

From the equation of state of air, the density of air at a height z is

$$\rho(z) = \frac{p(z)}{RT(z)} \tag{2.3.2}$$

Hence Eq(2.3.1) becomes

$$\frac{\partial p}{\partial z} = -\frac{gp(z)}{RT(z)} \tag{2.3.3}$$

If T(z) = $T_\circ$, a constant (isothermal atmosphere), we then obtain

$$\begin{aligned} \frac{\partial p}{\partial z} &= \frac{gp(z)}{RT_\circ} \\ &= -\frac{p}{H} \end{aligned}$$

where H, the scale height, is a constant (neglecting the small dependence of g on z) with the value $H = RT_\circ/M_{air}g$. Thus the solution of Eq.(2.3.1) becomes

$$p(z) = p_s e^{-\frac{z}{H}} \tag{2.3.4}$$

where p_s is the pressure at the surface z=0. Thus pressure decreases upward exponentially with height, with e-folding height H. For the troposphere, if we choose a representative value $T_\circ$ = 253 K, then H = 7.4 km.

If the temperature is not constant (non-isothermal atmosphere), we can still define a local scale height:

$$H(z) \quad = \quad -\frac{RT(z)}{g}$$

where H(z) is the local scale height. Therefore using Eq(2.3.1)

$$p(z) = p_s e^{-\int_0^z \frac{dz'}{H(z')}} \tag{2.3.5}$$

2.3.2 Vertical Distribution of Temperature

The vertical profile is divided into four distinct layers as displayed in Fig.2.2. These are the troposphere, stratosphere, mesosphere, and thermosphere.

The troposphere is marked by generally decreasing temperatures with height, at an average lapse rate, of $\sim 6.5°Ckm^{-1}$. Tropospheric air, which accounts for $\sim 80\%$ of the mass of the atmosphere, is relatively well mixed and it is continually being cleansed or scavenged of aerosols by cloud droplets and ice particles, some of which subsequently fall to the ground as rain or snow. Embedded within the troposphere are thin layers in which temperature increases with height (i.e., the lapse rate is negative). Within these so-called temperature inversions it is observed that vertical mixing is strongly inhibited.

The stratosphere is relatively dry (cloudless region of the atmosphere). However it is rich in ozone as it is the main region of ozone production. It is formed as a by-product of the photo-dissociation (photolysis) of molecular oxygen.

$$O_2 + h\nu \quad \rightarrow \quad O + O \tag{2.3.6}$$

$$O + O_2 + M \quad \rightarrow \quad O_3 + M \tag{2.3.7}$$

where hν is the energy of incoming photons, and M is any third body needed to carry the excess energy. The O_3 molecule formed in that reaction itself strongly absorbs radiation in the wavelength range of 240-320 nm to decompose back to O_2 and O

$$\begin{aligned} O_3 + h\nu &\rightarrow O + O_2 \quad Chappuis \quad bands \quad (400 - 600nm) && (2.3.8) \\ &\rightarrow O(^1D) + O_2 \quad Hartley \quad bands \quad (< 320nm) && (2.3.9) \end{aligned}$$

$O(^1D)$ is quenched to ground-state atomic oxygen by collision with N_2 and O_2:

$$\begin{aligned} O(^1D) + M &\rightarrow O + M && (2.3.10) \\ & && (2.3.11) \end{aligned}$$

Finally, O and O_3 react to reform two O_2 molecules:

$$O + O_3 \rightarrow O_2 + O_2 \qquad (2.3.12)$$

Ozone absorbs UV radiation from the sun and with the low densities present at stratospheric altitudes, this absorption is an efficient mechanism of transferring kinetic energy to a relatively small number of molecules for which the air temperature becomes high. Ozone in the upper stratosphere therefore acts as a heat source. Some of the heat is transferred down by subsidence and radiation, although the stratosphere as a whole remains warm at the top (temperatures close to those at the earth's surface) and cold at the bottom and therefore very stable. This is because the ozone layer is very opaque to UV (see Fig.2.2). Most of the UV flux is absorbed in the upper parts of the layer and there is little left to be absorbed at lower altitudes. Over the tropics the average height of the tropopause is about 17km. The tropical tropopause is remarkably cold, with temperatures as low as $-80°C$ [8].

Mesosphere extends from the stratopause to the mesopause (from $\sim$ 80 to 90 km altitude); temperature decreases with altitude up to mesopause, which is the coldest point in the atmosphere.

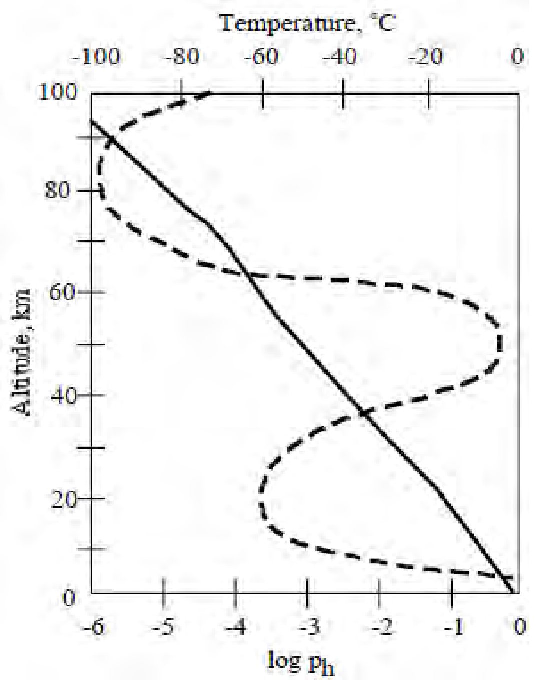

Figure 2.2: Variation of pressure (solid line) and temperature (dashed line) with altitude.

The layer above mesopause is the thermosphere, where the temperature is very high and very variable. It is here that very short wavelength UV is absorbed by oxygen both molecular and atomic oxygen thus heating the region. Molecules (including O_2as well as CO_2, the dominant IR emitter at this altitude) are dissociated (photolyzed) by high-energy UV ($\lambda < 0.1\mu m$). Therefore, because of the scarcity of polyatomic molecules, IR loss of energy is weak, so the temperature of the region gets very high (as much as 1000 K). The air is so tenuous that collisions are rare and there is no connection between temperature and thermal radiation. At and above these altitudes, the atmosphere becomes ionized (the ionosphere), causing reflection of radio waves, a property of the upper atmosphere which is of great practical importance [8].

Chapter 3

Atmospheric Carbon Monoxide

3.1 Sources of Atmospheric Carbonmonoxide(CO)

Carbon monoxide (CO) is one of the most widely distributed and commonly occurring air pollutants, with concentrations up to a few ppmv in polluted continental air masses. Each year, more CO is released into the atmosphere than any other pollutant, excluding CO_2, and the annual emission rate is increasing. It is emitted to the atmosphere naturally (e.g. from oceans, soils and plants, and as a result of forest fires, the atmospheric oxidation of methane and other nonmethane hydrocarbons and cosmic-ray neutrons), and anthropogenically as a result of fossil-fuel combustion, industrial processes, biomass burning and waste incineration. The anthropogenic inputs of CO have been estimated to be comparable with those from natural sources, but are steadily growing. This may have already caused the global concentrations of CO to double since the start of the Industrial Revolution, prior to which human activities did not significantly affect the global cycles of CO and other atmospheric trace gases. Khalil and Rasmussen suggested that the average CO concentration may have doubled even over the past 50 years or so, as a result of the increased anthropogenic emissions. Carbon monoxide has a lifetime of several weeks to a few months. In the troposphere CO originates from natural source or human activities, while in the stratosphere the oxidation of methane is the main source up to 35km. In the mesosphere, another source of CO is from the photodissociation of CO_2[10].

3.1.1 CO from Technological Sources

CO emissions arising from the partial combustion of hydrocarbon fuels, particularly petroleum products, have been responsible for significant declines in air quality in most cities of the world. CO concentrations measured in the tens of thousands of ppbv, more than a hundred times greater than background concentrations, have been regularly observed. From [11], Cullis and Hirschler recently estimated annual man-made emissions of CO to be of the order of 891.83 Tg yr^{-1} in 1979, having increased from 468.08 Tg yryr^{-1} in 1965. Around 80% of the emissions were attributed to the combustion of petroleum products with the majority of the remaining CO emissions being attributed to biomass burning. Cullis and Hirschler considered that CO emissions from coal combustion represented only $\sim 1 - 2\%$ of total CO emissions from technological sources. They also found, based on United Nations, OECD and other statistics, that overall petroleum consumption had more than doubled during the period 1965-79 [11]. By contrast Miiller (1990) considered, based on US EPA and OECD data, that CO emissions have declined during this same period [11]. Miiller (1990), using lower emission factors than Cullis and Hirschler (1989), derived an estimate of global CO emissions from technological sources of 373 Tg yr^{-1}. The substantial difference between these two estimates of global CO emissions from technological sources can be attributed to uncertainties in the emission factors associated with the consumption of the various fuels. Clearly, if we are to understand the global budget of CO, then the estimate of CO emissions from technological sources needs to be more clearly defined. An international effort to quantify the emissions of trace gases, particularly CO, from motor vehicles is warranted [11].

3.1.2 Biomass Burning

The international burning of land results in a major source of combustion products to the atmosphere. Most of this burning occurs in the tropics. Emissions from burning vegetation are typical of those from any uncontrolled combustion process and include CO_2, CO, NO_x, CH_4 and nonmethane hydrocarbons, and elemental and organic particulate matter. The quantity and type of emissions from a biomass fire depend not only on the type of vegetation but also on its moisture content, ambient temperature, humidity, and local wind speed. The effect of emissions from biomass burning on atmospheric chemistry and climate, particularly in the tropics, is critically important. Large-scale savanna burning in the dry season in Africa leads to regional-scale ozone levels that approach those characteristic of urban industrialized regions (60-100 ppbv)[11]. Accordingly, the flux of trace gases from biomass burning exhibits a strong seasonality in the tropics. Again, the seasonality in the flux of CO from biomass burning will act to reinforce the seasonality in CO concentrations induced by reaction with hydroxyl radicals[10].

3.1.3 Vegetation and Soils

CO is released directly from vegetation and soils. In both cases the release of CO is strongly dependent on temperature and to a lesser extent on soil moisture or precipitation. Annual CO fluxes for vegetation of 75 Tg CO yr^{-1} and for soil CO production of 15 Tg CO yr^{-1}, as calculated by Seiler and Conrad (1987) [11].

3.1.4 Oxidation of Methane

The oxidation of methane represents a major and increasing source of atmospheric CO. The principal oxidation reaction of methane, CH_4, is with the hydroxyl radical[12]:

$$CH_4 + OH \overset{O_2}{\longrightarrow} CH_3O_2 + H_2O \tag{3.1.1}$$

Followed by the following reactions:

$$CH_3O_2 + NO \overset{O_2}{\rightarrow} HCHO + HO_2 + NO_2 \tag{3.1.2}$$

$$HCHO + h\nu \overset{2O_2}{\rightarrow} CO + 2HO_2 \tag{3.1.3}$$

$$3(HO_2 + NO \rightarrow NO_2 + OH) \tag{3.1.4}$$

$$4(NO_2 + h\nu \overset{O_2}{\rightarrow} NO + O_3) \tag{3.1.5}$$

And thus, the net reaction becomes:

$$CH_4 + 8O_2 \rightarrow CO + H_2O + 2OH + 4O_3 \tag{3.1.6}$$

3.1.5 CO from the Oxidation of Nonmethane Hydrocarbons

Nonmethane hydrocarbons (NMHC) are produced in globally significant quantities by vegetation. It is considered that NMHCs are playing an important role in photochemical oxidant formation and in contributing, by reaction in the atmosphere, to the formation of organic acids to acidic deposition. Through rapid reaction with hydroxyl radicals in the troposphere oxidation of terpenes and isoprene contributes large quantities of CO to the troposphere [11].

3.2 Sinks for Atmospheric Carbonmonoxide

The major identified sinks of atmospheric CO are its oxidation in the troposphere, upward migration and oxidation in the stratosphere and upper layers of the atmosphere as well as uptake by soil[10].

3.2.1 Oxidation in the troposphere

The direct chemical reaction of CO with O_2 is much too slow to be of any significance. The oxidation of CO with the hydroxyl radical OH has been reported as the main mechanism responsible for the loss of CO in the atmosphere. In the neutral troposphere the major source of OH is the photolysis of O_3[10],

$$O_3 + h\nu(\lambda \leq 320nm) \rightarrow O(^1D) + O_2 \tag{3.2.1}$$

followed by the reactions:

$$O(^1D) + H_2O \rightarrow 2OH \tag{3.2.2}$$

$$CO + OH \rightarrow H + CO_2 \tag{3.2.3}$$

$$H + O_2 \rightarrow HO_2 \tag{3.2.4}$$

In the presence of sufficient NO,

$$HO_2 + NO \rightarrow OH + NO_2 \tag{3.2.5}$$

$$\tag{3.2.6}$$

which then photolyzes to produce O_3

$$NO_2 + h\nu(\lambda \leq 430nm) \rightarrow NO + O \tag{3.2.7}$$

$$O + O_2 \rightarrow O_3 \tag{3.2.8}$$

The net reaction is

$$CO + 2O_2 \rightarrow CO_2 + O_3 \tag{3.2.9}$$

If the NO concentration is very low, reaction 3.2.1 will not be very fast, and hence either the selg reaction of two radicals or the reaction of HO_2 with O_3 can begin

$$HO_2 + HO_2 \rightarrow H_2O_2 + O_2 \tag{3.2.10}$$

$$HO_2 + O_3 \rightarrow OH + 2O_2 \tag{3.2.11}$$

$$H_2O_2 + h\nu \rightarrow 2OH \tag{3.2.12}$$

The net reaction is

$$2CO + O_2 \rightarrow 2CO_2 \tag{3.2.13}$$

Finally, if HO_2 reacts with O_3 instead, then the net reaction becomes

$$CO + O_3 \quad \rightarrow \quad CO_2 + O_2 \tag{3.2.14}$$

From [10], Crutzen and Gidel used a two-dimensional photo-chemical model to evaluate the average concentrations of OH in the troposphere. Accordingly, they calculated an annual average global sink of CO of 2054 million tonnes (1226 and 828 million tonnes in the northern and southern hemispheres, respectively). Seiler and Conrad suggested a global sink of 1400-2600 million tonnes $year^{-l}$, with the tropical region (i.e. between $30°N$ and $30°S$) contributing 800-1600 million tonnes $year^{-l}$ as a result of the high concentrations of OH there[11]. Crutzen and Zimmermann estimated the average OH concentration in the troposphere to be about 7.5×10^{11} molecules m^{-3} and predicted a CO oxidation rate of 2050 million tonnes $year^{-1}$. The tropical belt, between $25°S$ and $25°N$, was estimated to contribute $\sim$ 70% to this global sink[10].

3.2.2 Transport to the Stratosphere

Carbon monoxide accumulated from the various sources in the lower atmosphere may eventually migrate, by convection, turbulence and mixing, to the upper atmosphere, where it is oxidized to CO_2. It has sometimes been suggested that the lower molecular weight of CO, compared with that of air, will cause a migration of the lighter density CO into the stratosphere. Above the tropopause, the reactions of CO with O, O_3, H_2O_2 or HO_2 to form CO_2 are believed also to be too slow to cause appreciable losses. Dissociation of CO can be excluded as a sink in the stratosphere. A likely process for the conversion of CO to CO_2 in the stratosphere is the reaction given in Eq.(3.2.14). However, other less well-known reactions may also contribute.

The effectiveness of the stratosphere as a chemical sink for CO depends, to a large extent, upon the rate at which CO can be transported into the stratosphere. The exchange of air between the troposphere and the stratosphere is limited by the tropopause layer, which acts as a barrier to convective transport. It has been suggested that the stratospheric sink mechanism could remove 11% of the tropospheric CO inventory per year. Seiler calculated a CO eddy-diffusion rate of 90 tonnes $year^{-1}$ in the northern hemisphere and estimated that the total global flux would amount to 110 million tonnes $year^{-1}$. In addition, he predicted that 7 million tonnes of CO are transported annually into the stratosphere with the vertical motion of the tropospheric air through the tropical tropopause. Seiler and Conrad estimated that the total CO flux into the stratosphere amounts to between 80 and 140 million tonnes $year^{-1}$, with 60-100 tonnes $year^{-1}$ taking place in the tropics [10].

3.2.3 Uptake by Soils

Tropical soils, which are rich in microbial population and organic matter, showed the greatest activity, and desert soils the least. Soils under cultivation were consistently less active than soils nearby under natural vegetation, mainly due to the lack of organic matter in the surface layer of the tilled soils. Because of their exposure to high levels of CO, roadside soils were higher in CO uptake capacity than similar soils in regions remote from roads. Seiler and Junge reported the results of laboratory and field tests concerning the uptake of CO by soils exposed to CO concentrations of between 0.2 and 0.3 ppmv, which are equivalent to the CO levels of continental air in unpolluted areas. The highest uptake rates of CO were found to occur at temperatures of $\sim 10°C$ over organic-rich soils, with values up to 0-9 mg $hour^{-1}m^{-2}$. At a temperature of $15°C$, which is a representative value for the mean soil temperature of the earth, the average rate of uptake of CO, for all types of soils tested, was 0.54 mg $h^{-1}m^{-2}$. By assuming this value to be true for the land areas in the tropical and temperate zones, the global CO consumption by soil was estimated to be 450 million tonnes $year^{-1}$(i.e. 300 and 150 million tonnes $year^{-1}$ in the northern and southern hemispheres, respectively). The experiments indicated that, with test atmospheres containing less than 2 ppbv of CO, soils act as a source of CO, rather than as a sink. Seiler therefore suggested that the global estimate for the CO uptake by soil of 450 million tonnes $year^{-1}$ is only a crude value because of the relationships found between the uptake rate and the concentration of CO in the atmosphere above the soil, the soil temperature and the type of soil. The uptake rates for heavily polluted regions will be considerably higher than the average value used above. However, the soil in the tropics may be a source, rather than a sink, for CO [10].

Seiler also deduced that the highest uptake rates occur in carbon-rich soils at a soil temperature of $30°C$. Carbon monoxide was found to be consumed only within a shallow surface layer a few centimeters thick. It was also discovered that a minimum soil moisture is required for the CO destruction. Conrad and Seiler estimated that the total sink strength of the soils world-wide is between 190 and 580 million tonnes $year^{-1}$. Seiler and Conrad suggest that the CO consumption by soils within humid tropical areas (i.e. tropical forests and grasslands) is 105 (± 35) million tonnes $year^{-1}$, compared with a total global uptake rate of 390 (± 140) million tonnes $year^{-1}$[11].

3.3 CO in the Upper Troposphere and Lower Troposphere

Tropical CO was measured by ALIAS(Aircraft Laser Infrared Absorption Spectrometer) on five ER-2 flight from Hawaii to the equator. It was found that CO is less variable in the tropics than at higher latitudes in the Northern Hemisphere. Over the central tropical Pacific Ocean($10°N$ to $3°S$, 150 to $160°W$), measured upper tropospheric CO is 60 ± 5 ppb with no seasonal variation. These mixing ratios are representative of the background tropical troposphere away from biomass burning [12].

In the tropical lower stratosphere, the CO mixing ratio decays with altitude due to photochemical loss. The vertical profile of CO is strongly affected by seasonal variations in the tropopause height. However, the potential temperature θ of the tropical tropopause varies less than tropopause height does. CO and θ are strongly anti-correlated in the tropics because adiabatic heating increases θ while photochemistry decrease the CO mixing ratio. The mean tropical tropopause of these ER-2 flight is at $\theta \approx 370 \pm 19K$ (altitude ranging from 15.5 to 17.2 km) with a corresponding mixing ratio of 58 ± 5 ppbv. By $\theta = 390K$, topical air has has only 45 ± 5 ppbv CO. The lowest mixing ratios measured by ALIAS in the tropics are 12 ± 2 ppbv at altitudes above 20km($\theta > 470k$)[12].

From the perspective of transport, the stratosphere can be divided in two layers based on potential temperature. The "overworld" is defined by $\theta > 380K$, and the stratospheric "middleworld" is bounded above by the $\theta = 380$ isentrope (i.e, surface of constant θ) and below by extra-tropical tropopause. In the extra-tropics, stratosphere-troposphere exchange is thought to occur by adiabatic quasi-horizontal mixing along isentropes, tropopause folding, and convection. However none of these mechanisms can transport significant material above the middleworld. Only in the tropics there is strong enough adiabatic heating for air parcels to ascend into the middleworld. It is seeming contradiction that up to 50% of the air in the tropical overworld has been entrained from the extra-tropical stratosphere. However this entertainment is nearly isentropic, so the extra-tropical overworld is the source of the entrained air. The entrained air originally entered the overworld through the tropical tropopause, but was transported poleward before being recycled back into the tropical overworld. Thus it is a reasonable assumption that all air parcel in the overworld entered the stratosphere through the tropical tropopause, and initially had 58 ± 5ppbv CO at $\theta = 380K$[12].

Chapter 4

The Absorption and Emission of Radiation

4.1 Transition Rates

When electromagnetic radiation falls on a molecule, the oscillating electric field of the radiation can in some cases disturb the potential energy of the molecule and allow it to escape from its stationary state i. The interaction between a molecule and a radiation field can be described by the time-dependent Schrödinger equation:

$$i\hbar\frac{\partial\Psi(t)}{\partial t} = (H_\circ + V(t))\Psi(t) \tag{4.1.1}$$

where $H_\circ$ is the time-independent Hamiltonian for the free molecule, whose solutions are the stationary states Ψ_i and Ψ_j. $\Psi(t)$ represents the time-dependent wave functions of the perturbed molecule which are linear combinations of the wave functions of the unperturbed molecule. V(t) is a time-dependent interaction potential. The corresponding general solution is:

$$\Psi = a_i(t)\Psi_i + a_j(t)\Psi_j \tag{4.1.2}$$

where a_i and a_j are weighting coefficients. Using these wave functions and the Schrödinger equation, the rate at which a system can be changed from one stationary state to another under the influence of a perturbing effect is given by

$$\frac{da_j}{dt} = -\frac{2\pi i}{h} e^{-(2\pi i/h)(\varepsilon_i - \varepsilon_j)t} \int_{-\infty}^{\infty} \psi_j^* V \psi_i dx \tag{4.1.3}$$

where ψ_i and ψ_j are functions of x and related to Ψ_i and Ψ_i respectively as

$$\Psi_i = \psi_i e^{-(2\pi i/h)\varepsilon_i t} \tag{4.1.4}$$

and

$$\Psi_j = \psi_j e^{-(2\pi i/h)\varepsilon_j t} \tag{4.1.5}$$

4.2 Interaction of Electromagnetic Radiation with a Molecular System

The electric field of the radiation oscillates at the point occupied by the molecule with a frequency ν. Using the exponential form of the equation yields

$$E_x = E_x^\circ (e^{2\pi i \nu t} + e^{-2\pi i \nu t}) \tag{4.2.1}$$

If the transitions are assumed to be induced by electric dipole interaction, V(t) in Eq.4.1.1 can be expressed as follows:

$$V(t) = E_x \mu_x \tag{4.2.2}$$

where μ_x the electric dipole moment of the molecule. Hence using 4.1.1, 4.2.1 and 4.2.2 one obtains

$$a_j = |\mu_{xij}|\, E_x^\circ [\frac{1 - e^{(2\pi i/h)(\varepsilon j - \varepsilon i + h\nu)t}}{\varepsilon j - \varepsilon i + h\nu} + \frac{1 - e^{(2\pi i/h)(\varepsilon j - \varepsilon i - h\nu)t}}{\varepsilon j - \varepsilon i - h\nu}] \tag{4.2.3}$$

where $|\mu_{xij}| = \int_{-\infty}^{+\infty} \psi_j^* \mu_x \psi_i$. The process of interest here is that in which the system goes from a lower energy level ε_i to a higher one ε_j (absorption process), thus Eq.4.2.3 becomes

$$a_j(t) = |\mu_{xij}|\, E_x^\circ [\frac{1 - e^{(2\pi i/h)(\varepsilon j - \varepsilon i - h\nu)t}}{\varepsilon j - \varepsilon i - h\nu}] \tag{4.2.4}$$

This yields

$$a_j^*(t)a_j(t) = \frac{4\pi^2}{h^2}\left|\mu_{xij}\right|^2 (E_x^\circ)^2 t \tag{4.2.5}$$

The energy per unit volume that is irradiated by the electromagnetic radiation (energy density) is given by

$$\rho = \frac{6}{4\pi}(E_x^\circ) \tag{4.2.6}$$

Using Eq(4.2.5) and Eq(4.2.6) give

$$\frac{d(a_j^* a_j)}{dt} = \frac{8\pi^3}{3h^2}\left|\mu_{xij}\right|^2 \rho \tag{4.2.7}$$

For isotropic radiation:

$$\begin{aligned} \frac{d(a_j^* a_j)}{dt} &= \frac{8\pi^3}{3h^2}(\left|\mu_{xij}\right|^2 + \left|\mu_{yij}\right|^2 + \left|\mu_{zij}\right|^2)\rho & (4.2.8) \\ &= \frac{8\pi^3}{3h^2}\left|\mu_{ij}\right|^2 \rho & (4.2.9) \end{aligned}$$

The rate of change of the system as a result of absorption of radiation under the perturbing effect of the electric field of the radiation is usually written with B_{ij}, called *Einstein's coefficient for induced absorption*. Introducing B_{ij} Eq(4.2.7) becomes:

$$\frac{d(a_j^* a_j)}{dt} = B_{ij}\rho \tag{4.2.10}$$

with

$$B_{ij} = \frac{8\pi^3}{3h^2}\left|\mu_{xij}\right|^2 \rho \tag{4.2.11}$$

In addition, if a relaxation process from a given state j to a lower energy state i is followed with emission of a photon of energy $E_j - E_i = h\nu$ in random direction, phase and polarization, then it is said to be spontaneous emission. The probability by units of time (transition rate) of such an event can be written as

$$\frac{dp_{ji}^{sp}}{dt} = A_{ji} \tag{4.2.12}$$

where A_{ji} *is the Einstein coefficient of spontaneous emission.*

If the incident radiation field can produce the emission of a second photon whose direction, phase and polarization are the same as that of the incident photon, provided state j is populated, it is said to be stimulated emission. Its probability is given by

$$\frac{dp_{ji}^{st}}{dt} = B_{ji}\rho \tag{4.2.13}$$

where B_{ji} is the *Einstein coefficient of stimulated emission.*

Now let us determine relationships between the three Einstein coefficients. Using Eq(4.1.12) and Eq(4.1.13), the probability of a system in state i emitting a quantum of radiation and undergoing a transition to state j will be

$$A_{ji} + B_{ji}\rho(\nu_{ij}) \tag{4.2.14}$$

For equilibrium to be maintained,

$$N_i B_{ij}\rho(\nu_{ji}) = N_j A_{ji} + N_j B_{ji}\rho(\nu_{ij}) \tag{4.2.15}$$

This leads to

$$\frac{N_j}{N_i} = \frac{B_{ij}\rho(\nu_{ij})}{A_{ji}} + B_{ji}\rho(\nu_{ij}) \tag{4.2.16}$$

From Boltzmanns distribution

$$\begin{aligned} \frac{N_j}{N_i} &= \frac{g_j}{g_i} e^{-\frac{E_j - E_i}{kT}} && (4.2.17) \\ &= \frac{g_j}{g_i} e^{-\frac{h\nu_{ij}}{kT}} && (4.2.18) \end{aligned}$$

where g_i and g_j are statistical weights of the lower and the upper energy levels respectively.

Using Plancks radiation law

$$\rho(\nu_{ij}) = \frac{8\pi h\nu_{ij}^3}{c^3}\left[\frac{1}{e^{h\nu_{ij}/kT}} - 1\right] \tag{4.2.19}$$

Using Eq(4.2.16),Eq(4.2.18) and Eq(4.2.19) we get the relationships between the Einstein coefficients:

$$\begin{aligned} A_{ji} &= \frac{8\pi h\nu_{ij}^3}{c^3} B_{ji} && (4.2.20) \\ B_{ij} &= \frac{g_j}{g_i} B_{ji} && (4.2.21) \end{aligned}$$

These relationships clearly show that, for a given transition, if one coefficient is known, the two others can be easily determined [13].

4.3 Absolute Intensity as a Function of the Einstein Coefficient

Considering I_ν is the intensity of radiation per unit frequency interval at frequency ν incident per unit area from a nearly parallel beam, then after passing through a path-length du of absorber, the change in intensity dI_ν will be

$$dI_\nu = -k_\nu I_\nu du \tag{4.3.1}$$

where k_ν is the absorption coefficient at frequency ν. Since each absorption line is not infinitely sharp but broadened by some factor, k_ν is varying across it over a range of frequency small compared with the line frequency. Over this frequency I_ν may be considered constant and Eq.4.3.1 may be integrated over frequency to give the total change dI in the energy in the beam:

$$\begin{aligned} dI &= \int dI_\nu d\nu && (4.3.2) \\ &= -I_\nu du \int_0^\infty k_\nu d\nu && (4.3.3) \\ &= -S I_\nu du && (4.3.4) \end{aligned}$$

where S has been written for $\int_0^\infty k_\nu d\nu$ and is known as the strength of the line.
The energy density ρ_ν of radiation in units of frequency is given by

$$\rho_\nu = \frac{I_\nu}{c} \tag{4.3.5}$$

The Einstein coefficient B_{ij} is defined such that $B_{ij}\rho_\nu$ is the probability per molecule of a transition from i to j per unit time in the presence of a radiation density ρ_ν per unit frequency interval at frequency ν. If the number of molecules per unit volume in the states i and j is N_i and N_j respectively, then the net rate of transition from i to j becomes

$$(N_iB_{ij} - N_jB_{ji})\rho_\nu = B_{ij}\rho_\nu(N_i - N_j\frac{g_i}{g_j}) \tag{4.3.6}$$

Since $h\nu$ energy is absorbed in each transition, the decrease in intensity becomes:

$$dI = -\frac{h\nu}{c}B_{ij}(N_i - N_j\frac{g_i}{g_j})I_\nu du \tag{4.3.7}$$

Using Eq(4.3.4), Eq(4.3.6) and Eq(4.3.7) we have

$$S_{ij} = -\frac{h\nu}{c}B_{ij}(N_i - N_j\frac{g_i}{g_j}) \tag{4.3.8}$$

To find the temperature dependence of the absolute intensity, let N is the total density of molecules and thus it can be written as

$$N = n_L\frac{T_\circ P}{TP_\circ} \tag{4.3.9}$$

where n_L is the density of molecules at standard temperature ($T_\circ = 273.15K$ and pressure $P_\circ = 1atm$). Hence Eq(4.3.8) becomes

$$S_{ij} = \frac{h\nu}{c}n_L\frac{T_\circ P}{TP_\circ Q(T)}e^{-hcE_i/kT}(1 - e^{-h\nu_{ij}/kT})g_gB_{ij} \tag{4.3.10}$$

4.4 Electric Dipole Transitions

In the previous section Eq(4.2.21) is the Eintein coefficient with electric dipole transition moment of (μ_{ij}). But this equation applies only to the non degenerate levels, i.e, $g_i = g_j = 1$. If we consider that both levels are degenerate, summations appear on the subcomponents of levels i and j. In addition, it is necessary to take into account that each sub-level i_k contributes a fraction $1/g_i$ to the population N_i of level i:

$$B_{ij} = \frac{2\pi^2}{3h^2c\epsilon_\circ}\frac{1}{g_i}\sum_{k=1}^{g_i}\sum_{l=1}^{g_j}|D(i_kj_l)|^2 \tag{4.4.1}$$

Comparison of Eq(4.2.21) and Eq(4.4.1) gives

$$g_i\left|D_{ij}\right|^2 = \sum_{k=1}^{g_i}\sum_{l=1}^{g_j}\left|\mu_{xij}\right|^2 \tag{4.4.2}$$

Thus,Eq(4.3.10) becomes

$$S_{ij} = \frac{2\pi^2}{3hc\epsilon_\circ}\frac{\nu}{c}n_L\frac{T_\circ P}{P_\circ TQ(T)}e^{-hcE_i/kT}(1-e^{-h\nu_{ij}/kT})g_i|D_{ij}|^2 \tag{4.4.3}$$

4.5 Vibrational Energy and Transitions

As seen in Fig.4.1 the bond between the two atoms in a diatomic molecule can be viewed as a vibrating spring in which, as the internuclear distance changes from the equilibrium value $\mathbf{r}_e$, the atoms experience a force that tends to restore them to the equilibrium position. The ideal, or harmonic, oscillator is defined as one that obeys Hookes law; that is, the restoring force F on the atoms in a diatomic molecule is proportional to their displacement from the equilibrium position. Substitution of the potential energy for this harmonic oscillator into the Schr$\ddot{o}$dinger wave equation gives the allowed vibrational energy levels, which are quantified and have energies ε_ν given by

$$\varepsilon_\nu = (\nu+\frac{1}{2})\bar{\omega}_{osc} \qquad cm^{-1}(\nu=0,1,2,....) \tag{4.5.1}$$

where $\bar{\omega}_{osc}$ is the wavenumber and ν is the vibrational quantum number. Some of these energy levels are shown in Fig.4.1. Further use of the Schr$\ddot{o}$dinger equation leads to the simple selection rule for the harmonic oscillator undergoing vibrational changes:

$$\Delta\nu = \pm 1 \tag{4.5.2}$$

However, real molecules do not exactly obey the laws of simple harmonic motion; real bonds, although elastic, are not so homogenous to obey Hook's law. Fig() shows diagramatically, the shape of the energy curve for a typical diatomic molecule, together with the ideal, simple harmonic parabola. A purely emperical expression which fits this curve

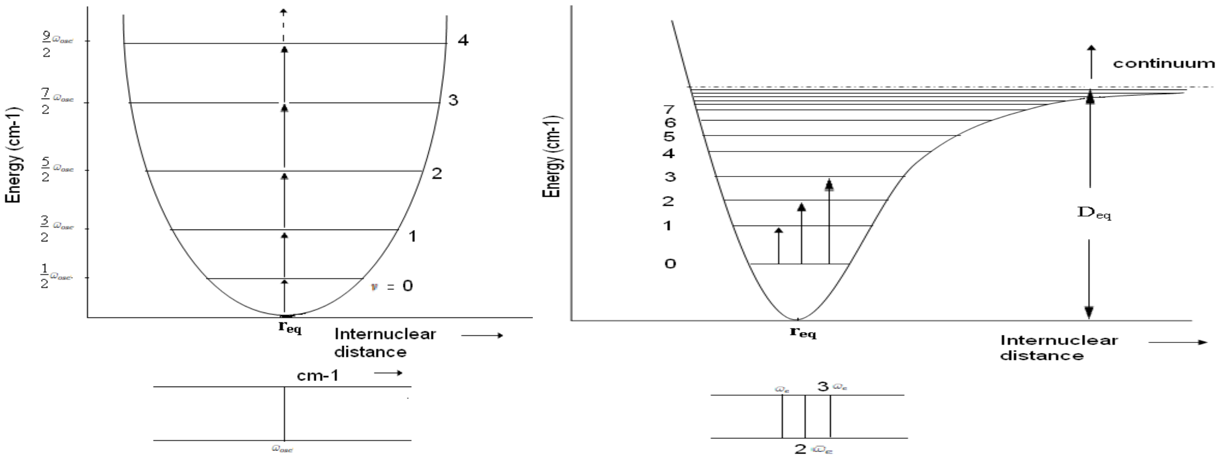

Figure 4.1: The allowed vibrational energy levels and transitions between them for a diatomic molecule undergoing simple harmonic motion

to a good approximation was derived by P.M. Morse, and it is called the Morse Function:

$$E = D_{eq}[1 - exp\{a(r_{eq} - r)\}]^2 \tag{4.5.3}$$

where a is a constant for a particular molecule and D_{eq} is the dissociation energy.

When Schrödinger equation is applied to Eq(4.5.3), the pattern of the allowed vibrational energy levels is found to be:

$$\varepsilon_\nu = (\nu + \frac{1}{2})\bar{\omega}_e - (\nu + \frac{1}{2})^2\bar{\omega}_e x_e + ...cm^{-1} \qquad (\nu = 0, 1, 2, ...) \tag{4.5.4}$$

where $\bar{\omega_e}$ is an oscillation frequency (expressed in wavenumber), and x_e is the corresponding anharmonicity constant which, for bond stretching vibrations, is always small and positive($\approx +0.01$), so that the vibrational levels crowed more closely together with increasing ν as seen in the Fig.4.1. The selection rules for anharmonic oscillator are found to be

$$\Delta\nu = \pm 1, \pm 2, \pm 3, ... \tag{4.5.5}$$

Thus they are the same as for the harmonic oscillator strength, with the additional probability of larger jumps. These, however, are predicted by theory and observed in practice to be of rapidly diminishing probability and normally only the lines of $\Delta\nu = \pm 1$,± 2 and

± 3, at the most, have observable intensity. Further, the spacing between the vibrational levels is of the order of $10^3 cm^{-1}$ and, at room temperature, the Boltzmann distribution gives us

$$\frac{N_{\nu=1}}{N_{\nu=0}} \approx 0.008 \tag{4.5.6}$$

i.e, the population of the $\nu = 1$ state is nearly 0.01 or 1% of the ground state population. Thus, to a very good approximation, we may ignore all transitions originating at $\nu = 1$ or more and restrict ourselves to the three transitions:

1. $\nu = 0 \rightarrow \nu = 1, \Delta\nu = +1$, with considerable intensity; $\Delta\varepsilon = \bar{\omega}_e(1 - 2x_e)cm^{-1}$.
2. $\nu = 0 \rightarrow \nu = 2, \Delta\nu = +2$, with small intensity; $\Delta\varepsilon = 2\bar{\omega}_e(1 - 3x_e)cm^{-1}$.
3. $\nu = 0 \rightarrow \nu = 3, \Delta\nu = +3$, with normally negligible intensity; $\Delta\varepsilon = 3\bar{\omega}_e(1 - 4x_e)cm^{-1}$.

These three transitions are shown in Fig.4.1. To a good approximation, since $x_e \approx 0.01$, the spectral lines are very close to the fundamental absorption($\bar{\omega}_e$), the first and the second overtones ($2\bar{\omega}_e$ and $3\bar{\omega}_e$). Although we have ignored transitions from $\nu = 1$ to higher states, we should note that, if the temperature is raised or if the vibration has a particularly low frequency, the population of $\nu = 1$ state may become appreciable. Thus, for $\nu = 1 \rightarrow \nu = 2$, $\Delta\nu = +1$, normally very weak, $\Delta\varepsilon = \bar{\omega}_e(1 - 4x_e)cm^{-1}$. Such absorptions are usually called hot bands since a high temperature is one condition for their occurrence[14].

4.6 Vibration-rotation

Molecules, of course, vibrate and rotate simultaneously. It is a good approximation that the total energy of the molecule (excluding translation) is the sum of the vibrational, rotational, and electronic energy of a molecule. Because we will be concerned only with low-energy irradiation we will neglect the possibility of exciting any of the electrons to higher states. To a first approximation, then, we expect the allowed energies to be the sum of a vibrational and a rotational part.

$$\varepsilon_{total} = \varepsilon_{rot} + \varepsilon_{vib} \tag{4.6.1}$$

The rotational energy levels of non-rigid molecule, if the force field is anharmonic, are given by

$$\varepsilon_{rot} = BJ(J+1) - DJ^2(J+1)^2 + H^3(J+1)^3 + K^4(J+1)^4 ... \qquad cm^{-1} \tag{4.6.2}$$

where D is centrifugal distortion constant and is given by

$$D = \frac{4B^3}{\bar{\omega}^2} \qquad cm^{-1} \tag{4.6.3}$$

and $\bar{\omega}$ is the vibrational frequency of the bond and H, K, etc are small constants dependent upon the geometry of the molecule. Taking the separate expressions for ε_{rot} and ε_{vib} from Eq(4.5.4) and (4.6.2) respectively we have:

$$\varepsilon_{total} = BJ(J+1) - DJ^2(J+1)^2 + H^3(J+1)^3 + K^4(J+1)^4 ... + (\nu + \frac{1}{2})\bar{\omega}_e - x_e(\nu + \frac{1}{2})^2\bar{\omega}_e \tag{4.6.4}$$

Ignoring the constants D, H, etc we get:

$$\varepsilon_{total} = BJ(J+1) + (\nu + \frac{1}{2})\bar{\omega}_e - x_e(\nu + \frac{1}{2})^2\bar{\omega}_e \tag{4.6.5}$$

The selection rules for the combined motions are the same as those for each separately; therefore we have

$$\Delta\nu = \pm1, \pm2, \qquad etc. \qquad \Delta J = \pm1 \tag{4.6.6}$$

From Born-Oppenheimer approximation, rotation is unaffected by vibrational changes, i.e B is identical in the upper and lower vibrational states. Hence making use of the selection rule for the transition $\nu = 0 \rightarrow \nu = 1$, we get

$$\Delta\varepsilon = \bar{\omega}_\circ + B(J' - J'')(J' + J'' + 1) \qquad cm^{-1} \tag{4.6.7}$$

where $\bar{\omega}_\circ$ is usually the band origin or band center and it is $\bar{\omega}_\circ = \bar{\omega}_e(1 - 2x_e)$. Lines to the the low frequency side of $\bar{\omega}_\circ$, correspond to $\Delta J = -1$ are referred to as the P branch and they are:

$$\Delta\varepsilon_{J,\nu} = \bar{\omega}_\circ + 2B(J''^{+1})cm^{-1}, J'' = 0, 1, 2, .. \tag{4.6.8}$$

while those to the high frequency side, $\Delta J = +1$, are the R branch and, they are:

$$\Delta\varepsilon_{J,\nu} = \bar{\omega}_\circ - 2B(J''^{+1})cm^{-1}, J' = 0, 1, 2, .. \tag{4.6.9}$$

Considering the possibility of degeneracy and Boltzmann distribution, the relative population of the levels at an energy will be

$$population = (2J + 1)\exp(-E_J/kT) \tag{4.6.10}$$

This shows that the maximum population of levels, and hence the intensity of transition, occurs at

$$J = \sqrt{kT/2Bhc} - \frac{1}{2} \tag{4.6.11}$$

which results in

$$\vec{\nu}_{max.intensity} = \bar{\omega}_\circ + 2B(\sqrt{kT/2Bhc} + \frac{1}{2}) \qquad for \qquad R \qquad branch; \tag{4.6.12}$$

$$\vec{\nu}_{max.intensity} = \bar{\omega}_\circ - 2B(\sqrt{kT/2Bhc} + \frac{1}{2}) \qquad for \qquad P \qquad branch. \tag{4.6.13}$$

The separation between the two maxima is

$$\Delta\bar{\nu} = \sqrt{8kTB/hc} + 2B \tag{4.6.14}$$

Since B is small compared with $\Delta\bar{\nu}$, we can write

$$\Delta\bar{\nu} \;\approx\; \sqrt{8kTB/hc}, B \approx hc(\Delta\bar{\nu})^2/8kTcm^{-1} \tag{4.6.15}$$

If we examine the vibrational spectrum of CO at 2143cm^{-1} under moderate resolution, we find that it consists of two peaks of different intensities which change with temperature. Higher resolution reveals that these peaks are simply the envelope of a series of lines which are approximately equally spaced, apart from a gap in the middle. The spacing between these lines close to 1.92118cm^{-1}, i.e, the same as the line spacing in the pure rotational spectrum derived in the microwave studies[14].

4.7 Breakdown of the Born-Oppenheimer Approximation: Interaction of Rotations and Vibrations

So far we have assumed that vibration and rotation can proceed quite independently of each other. A molecule vibrate some 10^3 times during the course of a single rotation, however, it is evident that the bond length (and hence the moment of inertia and B constant) also change continually during the rotation. It is evident from Fig.4.1 that an increase in the vibrational energy is accompanied by an increase in the bond length and hence the value of will depend on the ν quantum number. In general, the average bond length increases with the vibrational energy, B is smaller in the upper vibrational state than in the lower. That is,

$$B_\nu = B_e - \alpha(\nu + \frac{1}{2}) \tag{4.7.1}$$

where B_e is the equilibrium value of B and α is a small positive constant for each molecule.

Thus for the fundamental vibrational change, i.e, for the transition $\nu = 0 \to \nu = 1$, let the respective B values as $B_\circ$ and B_1 with $B_\circ > B_1$, hence,

$$\Delta\varepsilon \;=\; \bar{\omega}_\circ + B_1 J'(J'+1) - B_\circ J''(J''+1) cm^{-1} \tag{4.7.2}$$

Hence for R branch lines:

$$\Delta\varepsilon = \bar{\nu}_R = \bar{\omega}_\circ + (B_1 + B_\circ)(J'' + 1) + (B_1 - B_\circ)(J'' + 1)^2 cm^{-1} \qquad (J'' = 0, 1, 2, \tag{4.7.3}$$

and for P branch:

$$\Delta\varepsilon = \bar{\nu}_P = \bar{\omega}_\circ - (B_1 + B_\circ)(J' + 1) + (B_1 - B_\circ)(J' + 1)^2 cm^{-1} \qquad (J' = 0, 1, 2, \tag{4.7.4}$$

These two equations can be combined to into the expression

$$\bar{\nu}_{P,R} = \bar{\omega}_\circ + (B_1 + B_\circ)m + (B_1 - B_\circ)m^2 \qquad cm^{-1} \qquad t(m = \pm 1, \pm 2, ...) \tag{4.7.5}$$

where positive m values refer to the R branch and negative to P.

4.8 The Width and Shape of Molecular Spectral Lines

Since the spectrometer has a very high resolving power, it is found that the individual lines in a vibration-rotation band do not have zero width, but that each line is broadened out over a narrow frequency interval. Several factors can cause this broadening. These are:

1. the finite natural lifetime in an excited state;
2. collisions and mutual interactions between molecules; and
3. the Doppler effect of thermal motion of the molecules.

The fundamental property of a discrete line transition is the spectral absorption cross section, $\alpha(\nu)$, which measures the strength of the transition as a function of frequency. The value of $\alpha(\nu)$ depends on the absorber type, local temperature and pressure.

The absorber mass path between two points p_1 and p_2 is:

$$U(p_1, p_2) = \int_{p_1}^{p_2} u(s)ds \tag{4.8.1}$$

where u(s) is the absorber amount in the path ds.

The absorbtion coefficient is:

$$k_\alpha(\nu) = \alpha(\nu)N_\circ \tag{4.8.2}$$

where $N_\circ$ is the number concentration ($moleculem^{-3}$) of the species.

Each absorbtion line is not infinitely sharp but broadened by some factors to be discussed later. This means that, for any line, $\alpha(\nu)$ is varying across it over a range of frequency small compared with the line frequency. Hence, the strength of the line is

$$S = \int_0^\infty \alpha(\nu)d\nu \tag{4.8.3}$$

We shall describe line profiles in terms of a line shape factor, $\Phi(\nu - \nu_\circ)$, defined by

$$\Phi(\nu - \nu_\circ) = \alpha(\nu)/S \tag{4.8.4}$$

where $\nu_\circ$ is the central frequency of the unperturbed transition.

The shape factor for each transition (i.e., line) is normalized to unity,

$$\int \Phi(\nu - \nu_\circ) = 1 \tag{4.8.5}$$

the integral is over a single line, i.e., it includes contributions only from a single vibrational-rotational transition.

4.8.1 Natural Line Shape and Line Width

Natural broadening is the result of the probability of spontaneous emission between an upper state and a lower energy state. This probability limits the life-time in the upper state if the molecule is considered to be isolated from radiation fields and other particles. The life-time in a state and its energy are linked by the uncertainty principle ($\Delta t \Delta E \geq \hbar$). The intensity is given by the relationship

$$I(\nu) \sim A(\nu)A^*(\nu) \tag{4.8.6}$$

Thus, using the relation given in Eq(4.2.1) and Eq(4.8.6),

$$I(\nu) = \frac{I_\circ}{(\nu - \nu_\circ)^2 + \frac{1}{4\tau^2}} \tag{4.8.7}$$

The profile thus obtained is a Lorentzian profile. The profile has to be normalized because changing the profile must not change the area under it. The normalized line profile defined in Eq.4.8.5 is

$$\Phi(\nu - \nu_\circ) = kI(\nu) \tag{4.8.8}$$

where k is a constant of normalization to be determined using the following integral:

$$\int_0^\infty \Phi(\nu - \nu_\circ) = 1 \tag{4.8.9}$$

The integration gives $k = \Gamma/4\pi^2 I_\circ$ and the normalized line profile (line shape) due to the natural broadening is written as

$$\Phi_n(\nu - \nu_\circ) = \frac{\alpha_n}{\pi[(\nu - \nu_\circ)^2 + \alpha_n^2]} \tag{4.8.10}$$

where α_n is the natural line shape half width at half-maximum (HWHM) of the normalized Lorentzian profile. For a given transition (here $j \rightarrow i$), it is possible to give an estimate of the natural width, provided one knows the corresponding life-times of these states:

$$\alpha(\nu) = \frac{1}{4\pi c}(\frac{1}{\tau_i} + \frac{1}{\tau_j}) \tag{4.8.11}$$

where τ_i and τ_j are the life-times of the lower and the upper energy states involved in the molecular transition respectively.

The natural life time of the excited state of a molecule is of the order of $10^{-2} - 10^{-1} sec$. This is much longer than the life time between collisions in a gas at all ordinary pressures and so in practice, therefore, the line shapes we are concerned with are dominated by collisional effects[7].

4.8.2 Pressure Broadening

Collisions between molecules are the most important cause of line broadening in the lower atmosphere. An isolated molecule emits or absorbs an almost purely harmonic wave given by

$$f(\nu) = A cos 2\pi\nu_{\circ}ct \tag{4.8.12}$$

where c is the velocity of light and A is an arbitrary amplitude. During the period -t/2 to t/2, the distribution of amplitude $g(\nu)$ of the wave in the discrete wavenumber domain may be obtained from the Fourier cosine transform as follows:

$$\begin{aligned} g(\nu) &= (\frac{2}{\pi})^{1/2}\int_0^{t/2}(A cos 2\pi\nu_{\circ}ct')cos 2\pi\nu ct\prime dt\prime & (4.8.13)\\ &= \frac{A}{(2\pi)^{3/2}c}[\frac{\sin\pi(\nu+\nu_{\circ})ct}{\nu+\nu_{\circ}}+\frac{\sin\pi(\nu-\nu_{\circ})ct}{\nu-\nu_{\circ}}] & (4.8.14)\end{aligned}$$

Now we are dealing with lines whose widths are very small compared to $\nu_{\circ}$, so that the first term in Eq(4.8.14) may be neglected in comparison with the second. If a radiating molecule collides with another molecule, it alters the radiating harmonic wave train due to the intermolecular forces, and the frequency of the emitting molecules would be temporarily shifted by an appreciable amount. After the collision the molecule starts emitting at another phase and these new phases are now randomly distributed. From general statistical principles, the time between collisions is distributed according to Poissons law that the probability a collision occurs between t and t + dt is $e^{-t/t_{\circ}}$, where $t_{\circ}$ is the mean time between collisions. All the initial phases of the wave trains must be averaged. Thus, the absorption coefficient will be given by

$$k_{\nu} = A'\int_0^{\infty} g(\nu)^2 e^{-t/t_{\circ}}dt \tag{4.8.15}$$

where A' is a constant which may be determined by using Eq(4.8.14). Thus Eq(4.8.15) becomes:

$$k_{\nu} = \frac{S}{\pi}\frac{\alpha_p}{(\nu-\nu_{\circ})^2+\alpha_p^2} \tag{4.8.16}$$

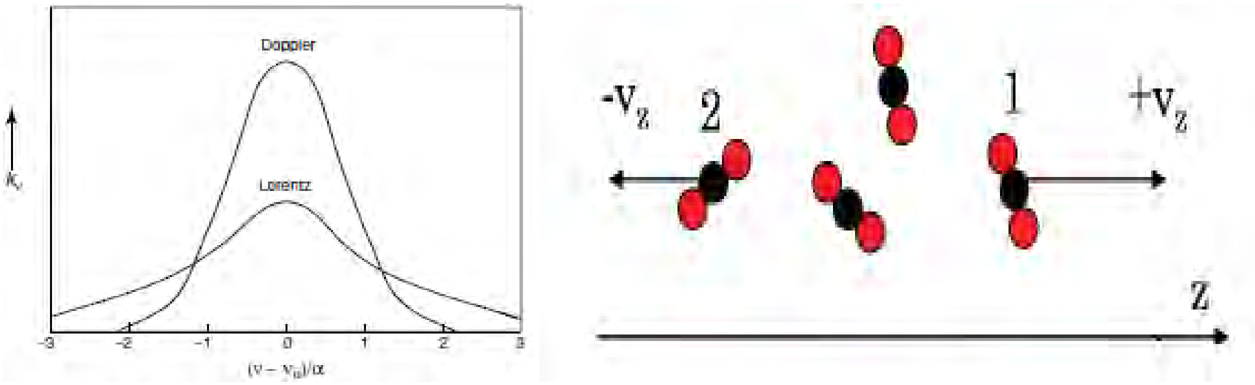

Figure 4.2: Left: Lorentz and Doppler line shapes for the same intensities and line widths. Right: molecules in motion due to thermal excitation. z is the axis of light propagation.

where $\alpha_p = \frac{1}{2\pi t_\circ}$ is the half width at half-maximum intensity due to pressure (pressure-broadened line width). Thus the shape of spectral lines due to collisions is given by the Lorentz profile. Fig.4.2 illustrates Lorentz profile. From kinetic theory of gases, α_p is dependent on pressure p and temperature T :

$$\alpha_p(p,T) = \alpha_p(p_\circ, T_\circ)\frac{p}{p_\circ}(\frac{T_\circ}{T})^{1/2} \tag{4.8.17}$$

where $p_\circ$ is the standard pressure (1013mb) and $T_\circ$ is the standard temperature(273K). Since α_p charaterizes collisional interactions, its value depends on the concentrations and masses of all the molecular species which are present. From pure kinetic theory,

$$\alpha_p = \sum_i n_i^2[(\frac{2kT}{\pi})(\frac{1}{m} + \frac{1}{m_i})]^{1/2} \tag{4.8.18}$$

where the summation is over all perturber species i, n_i is the number density of the i^{th} species of the perturber, m_i is its mass and m is the mass of the absorber. Hence, α_p is proportional to the number of molecules per unit volume and also proportional to the mean speed of the molecules.

In practice in the lower atmosphere $\alpha_p \gg \alpha_n$ so the Lorentz line width is nearly equivalent to the pressure-broadened line width. Therefore, Lorentz broadening and the Lorentz line width will refer to the Lorentzian line shape due to the convolution of natural and collision broadening. When natural and collision broadening are considered simultaneously, it can be shown that the combined line shape is also a Lorentzian with HWHM of α_L. Using Eq(4.8.8) the line shape becomes[15]

$$\Phi_L(\nu) = \frac{\alpha_L}{\pi(\nu^2 + \alpha_L^2)} \tag{4.8.19}$$

And the absorption cross-section for Lorentzian lines is:

$$\alpha(\nu) = \frac{S\alpha_L}{\pi(\nu^2 + \alpha_L^2)} \tag{4.8.20}$$

4.8.3 Doppler Line Shape and Line width

In the upper atmosphere (above 50km), where molecular collisions are much less frequent, Doppler broadening is the dominant factor. In gases at low pressures, the major contribution to the shape of absorption lines comes from the thermal motion of the absorbing molecules. If the molecules motion is in the direction of the light propagation or in the opposite way, the central wavenumber of the absorption lines will be shifted upward or downward respectively (see Fig.4.2). Depending on the direction of motion of the molecule with respect to the light propagation, the wavenumber $\nu_\circ$ is shifted to an effective wavenumber of absorption ν:

$$\nu = \nu_\circ(1 + \frac{\upsilon_z}{c}) \quad \textbf{for} \quad \textbf{molecule} \quad \textbf{1} \tag{4.8.21}$$

$$\nu = \nu_\circ(1 - \frac{\upsilon_z}{c}) \quad \textbf{for} \quad \textbf{molecule} \quad \textbf{2} \tag{4.8.22}$$

At thermodynamical equilibrium, the molecules of a gas follow a Maxwellian velocity distribution. At temperature T, the number of molecules in the level E_i per unit volume $N_i(\upsilon_z)d\upsilon_z$ having a velocity component between υ_z and $\upsilon_z + d\upsilon_z$ is equal to

$$N_i(\upsilon_z)d\upsilon_z = \frac{N_\circ^i}{\sqrt{\pi}\upsilon_p} e^{-(\upsilon_z/\upsilon_p)^2} d\upsilon_z \tag{4.8.23}$$

where $N_\circ^i$ is the total density of molecules in level E_i and $\upsilon_p = \sqrt{2kT/m} = \sqrt{2RT/M}$ is the most probable velocity, m is the mass of the molecule, R is the gas constant and M is the molar mass (in g mol^{-1}). Hence, from []

$$N_i(\nu)d\nu = N_\circ^i\sqrt{\frac{Mc^2}{2\pi\nu_{ij}^2RT}}e^{-\frac{Mc^2(\nu-\nu_{ij})^2}{2\nu_{ij}^2RT}}d\nu \tag{4.8.24}$$

The absorbed radiant power being proportional to the density of molecules $N_i(\nu)d\nu$, the intensity of a Doppler-broadened spectral line can be written as

$$I = I_\circ e^{-\frac{Mc^2(\nu-\nu_{ij})^2}{2\nu_{ij}^2RT}} \tag{4.8.25}$$

Following the same procedure of normalization explained in the previous section $\Phi_D(\nu - \nu_{ij}) = kI(\nu)$, we can obtain the normalized Doppler line profile[15]:

$$\Phi_D(\nu - \nu_{ij}) = \sqrt{\frac{Mc^2}{2\pi\nu_{ij}^2RT}}e^{-\frac{Mc^2(\nu-\nu_{ij})^2}{2\nu_{ij}^2RT}} \tag{4.8.26}$$

From Eq (4.8.26), we can calculate for the transition of wavenumber ν_{ij} at the HWHM $\alpha_D(\nu_{ij}) = |\nu_i - \nu_j|/2$ such that $\Phi(\nu_1 - \nu_{ij}) = \Phi(\nu_2 - \nu_{ij}) = \Phi_D(0)/2$:

$$\alpha_D(\nu_{ij}) = \frac{\nu_{ij}}{c}\sqrt{\frac{2\ln 2RT}{M}} \tag{4.8.27}$$

$$= 3.581x10^{-7}\nu_{ij}\sqrt{\frac{T}{M}} \tag{4.8.28}$$

This yields

$$\Phi_D(\nu - \nu_{ij}) = \sqrt{\frac{\ln 2}{\pi}}\frac{1}{\alpha_D}e^{-\ln 2(\frac{\nu-\nu_{ij}}{\alpha_D})^2} \tag{4.8.29}$$

4.8.4 The Voigt Profile

In the altitude region extending from about 20 to 50 km, effective line shapes are determined by both collision- and Doppler-broadening processes. The profile resulting of these two contributions is called the Voigt profile. If we assume these two processes are independent but occur simultaneously, then the net line shape of the total process will be the collision-broadened line shape, shifted by the Doppler shift. Thus the Voigt profile is the convolution of the Lorentz pressure profile and the Doppler profile [15]:

$$\Phi_v(\nu - \nu_{ij}) = \Phi_D(\nu) * \Phi_p(\nu - \nu_{ij}) \tag{4.8.30}$$

$$= \int_{-\infty}^{+\infty}\Phi_D(\nu\prime)\Phi_p(\nu - \nu_{ij} - \nu\prime)d\nu\prime \tag{4.8.31}$$

which yields

$$\Phi_v(\nu - \nu_{ij}) = \sqrt{\frac{\ln 2}{\pi^3}} \frac{\alpha_p}{\alpha_D} \int_{-\infty}^{+\infty} \frac{e^{-ln2(\nu\prime/\nu_{ij})^2}}{(\nu - \nu_{ij} - \nu\prime)^2 + \alpha_p^2} \tag{4.8.32}$$

or else:

$$\Phi_v(\nu - \nu_{ij}) = \sqrt{\frac{\ln 2}{\pi}} \frac{1}{\alpha_D} K(x, y) \tag{4.8.33}$$

where the complex error function

$$K(x, y) = \frac{y}{\pi} \int_{-\infty}^{+\infty} \frac{e^{-t^2}}{(x - t)^2 + y^2} dt \tag{4.8.34}$$

is the reduced Voigt profile, with

$$x = \sqrt{\ln 2} \frac{\nu - \nu_{ij}}{\alpha_D} \tag{4.8.35}$$

$$y = \sqrt{\ln 2} \frac{\alpha_p}{\alpha_D} \tag{4.8.36}$$

Chapter 5

The Michelson Interferrometer as a Spectrometer

5.1 Basic Principles

The essential piece of optical hardware in a FT-IR spectrometer is the interferrometer. The basic scheme of an idealized Michelson interferometer is shown in Fig.5.1. Infrared light emitted by a source is formed into a collimated beam by the entrance optics(aperture) and is then splitted by the beamsplitter to form two secondary beams. The beamsplitter is supposed to be ideal, that is, it allows half of the light to pass through while it reflects the other half. The reflected part of the beam travels to the fixed mirror M_1 through a distance x_1, is reflected there and hits the beamsplitter again after a total path length of $2x_1$. The same happens to the transmitted part of the beam. However as the reflecting mirror M_2, for this interferometer arm is not fixed at the same position x_1 but can be moved very precisely back and forth around x_1 by a distance $x_2 - x_1$. Thus, when the two halves of the beams recombine again on the beamsplitter they exhibit a path length difference or optical retardation. The difference between the two optical paths x_1 and x_2 is called optical path difference (OPD). It is equal to

$$\delta = 2(x_2 - x_1) \tag{5.1.1}$$

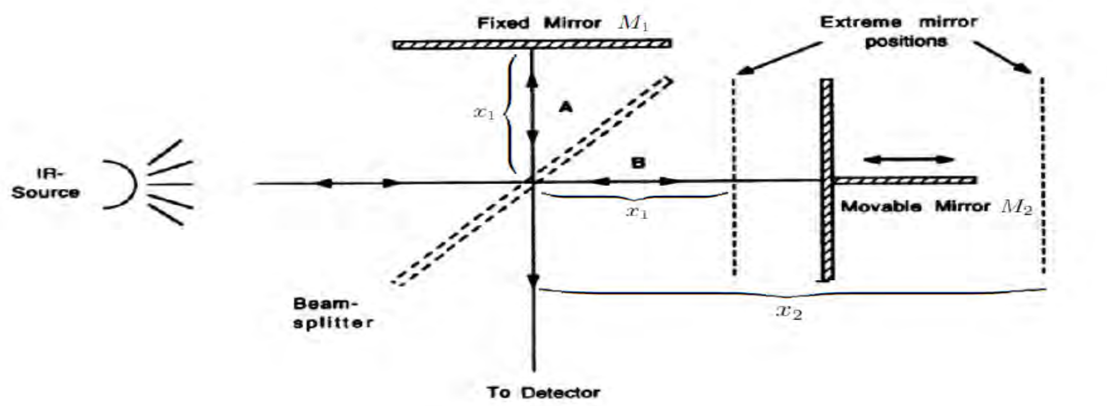

Figure 5.1: Schematic diagram of the optical layout of a Michelson interferometer.

The beam leaving the interferometer is finally focused on the detector D. The quantity actually measured is thus the intensity I(x) of the combined IR beams as a function of the moving mirror displacement δ, the so called interferrogram see Fig.5.1 The interference pattern as seen by the detector is shown in Fig.5.2 for the case of a single, sharp spectral line. The interferometer produces and recombines two wave trains with a relative phase difference, depending on the mirror displacement. These partial waves interfere constructively, yielding a maximum detector signal, if their optical retardation is an exact multiple of the wavelength of the source, $\delta = n\lambda$, where n=0, 1, 3,.... Destructive interference occurs when the retardation of the two mirrors is equal to $\delta = \frac{n\delta}{2}$ where n is odd. However, most sources are not monochromatic. Therefore, the signal must be viewed as a function of constructive and destructive interference from a polychromatic source[16].

Let R be the coefficient of reflection and T be the coefficient of transmission of the beam splitter. The amplitude of the electromagnetic wave at the location of the detector can be described by the superposition of the two secondary beams by the relation

$$A(x_1, x_2, \nu) = R.T.A\{\exp(i\omega t - 2\pi\nu x_1) + \exp(i\omega t - 2\pi\nu x_2)\} \tag{5.1.2}$$

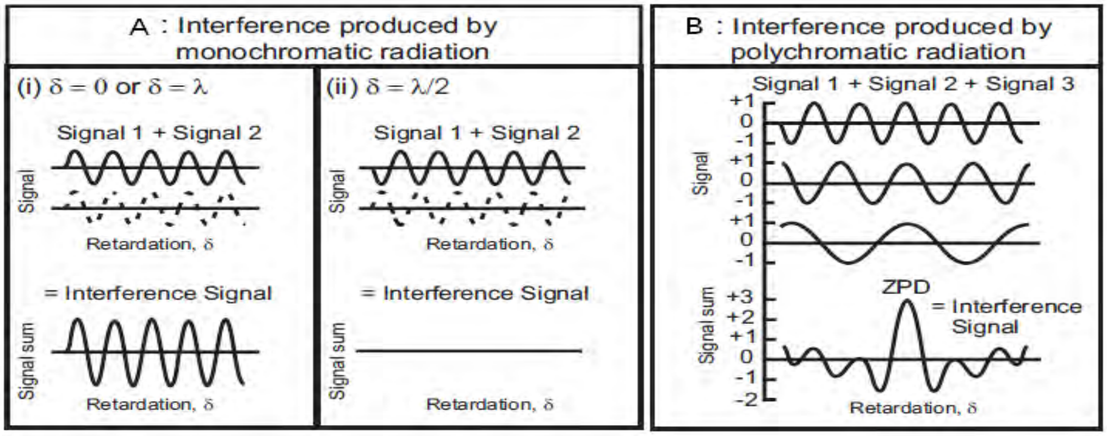

Figure 5.2: A)Schematic representation of the interference produced by adding monochromatic electromagnetic waves from the stationary mirror and movable mirror at different values of the optical path difference or retardation, δ. i) The optical path has a zero path difference (ZPD), $\delta = 0$ or λ causing the waves to interact constructively; ii) The optical path difference is one half of a wavelength, $= \lambda/2$, causing the waves to interact destructively.B)Schematic diagram showing how an interferogram is the sum of a series of electromagnetic waves of different wavelength (polychromatic radiation).

However it is the intensity not the amplitude that can be measured. The intensity of the interferogram, $I'(x_1, x_2, \nu)$ is a real and not a complex quantity which is given by the square of the amplitude. For monochromatic point source this can be written as

$$\begin{aligned} I'(x_1,x_2,\nu) &= \mathrm{A}(x_1,x_2,\nu).\mathrm{A}^*(x_1,x_2,\nu) \\ &= \mathrm{RTA}\{\mathrm{expi}(\omega\mathrm{t}\text{-}2\pi(\nu)x_1)+\mathrm{expi}(\omega\mathrm{t}\text{-}2\pi(\nu)x_2)\}.\mathrm{RTA}\{\mathrm{expi}(\omega\mathrm{t}\text{-}2\pi(\nu)x_1)+ \\ &\quad \mathrm{expi}(\omega\mathrm{t}\text{-}2\pi(\nu)x_2)\}^* \\ &= |\mathrm{RT}|^2\mathrm{A}^2(\nu)\{\exp(\mathrm{i}2\pi\nu(x_2-x_1))+\exp(\text{-}\mathrm{i}2\pi\nu(x_2-x_1))+2\}. \end{aligned}$$

We know that,

$$exp(i2\pi\nu(x_2 - x_1)) = \cos(2\pi\nu(x_2 - x_1)) + i\sin(2\pi\nu(x_2 - x_1)) \tag{5.1.3}$$

$$exp(-i2\pi\nu(x_2 - x_1)) = \cos(2\pi\nu(x_2 - x_1)) - i\sin(2\pi\nu(x_2 - x_1)) \tag{5.1.4}$$

Thus,

$$exp(i2\pi\nu(x_2 - x_1)) + exp(-i2\pi\nu(x_2 - x_1)) = 2\cos(2\pi\nu(x_2 - x_1)) \tag{5.1.5}$$

Hence,

$$I'(x_1, x_2, \nu) = 2 \mid RT \mid^2 A^2(\nu)(1 + cos2\pi\nu(x_2 - x_1)) \tag{5.1.6}$$

This can also be written as a function of the OPD:

$$I'(\delta) = 2 \mid RT \mid^2 A^2(\nu)(1 + cos2\pi\nu\delta) \tag{5.1.7}$$

Given that the beamsplitter splits up the incident light among the two secondary beams at any wave number equally,i.e, R=T=1/2, the intensity can be written as [17]:

$$I'(\delta) = 0.5I(\bar{\nu}_o)(1 + cos2\pi\nu\delta) \tag{5.1.8}$$

The exact position of the movable mirror has to be known with high precission while recording the interferogram. Taking the advantage of Eq.(5.1.7), the beam of a frequency stabilized monochromatic laser is added to the interferrometer. Knowing the exact frequency of the laser, the relative displacement of the movable mirror can easily be calculated by simply counting the interference fringes of the laser beam. Simultaneously, the signal from the laser can be used for the absolute calibration of the spectrum. this is known as the connes advantage of FT instruments. All path differences are measured relative to the maximum of the interferrogram, which gives the zero path difference (ZPD). Only in the case of ZPD; all frequencies interfere constructively.

In the Eq.(5.1.8), the first term is the intensity of the interferogram for a path difference of zero, where the maximum of the interferogram is located. The second term contains the modulation of the signal as a function of the OPD. The modulated part is the one which is of interest for spectroscopic measurement and hence, it is

$$I(\delta) = 0.5I(\bar{\nu}_o)\cos 2\pi\nu\delta \tag{5.1.9}$$

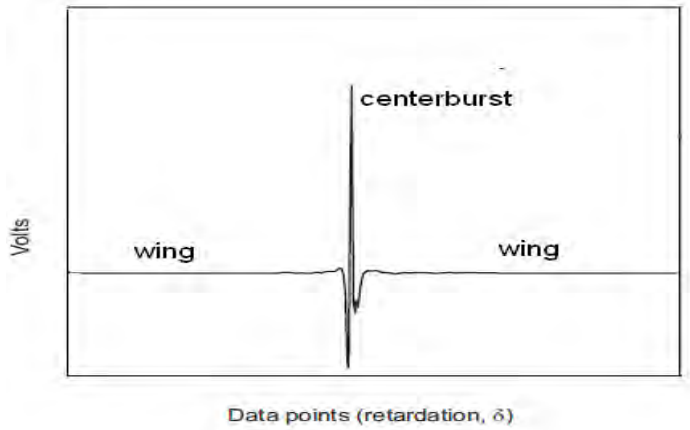

Figure 5.3: The interferogram of a broad band infrared source.The interferogram is generally recorded as voltage versus optical path distance units. The Y axis is in voltage since this is the unit in which the detector measures infrared intensity.

This equation defines the interferogram of a polychromatic source as a function of OPD, which is the raw data collected and illustrated in Fig.5.2. The interferogram shown in Fig.5.3 displays a sharp intensity spike at ZPD, called the centerburst, and low intensity at higher OPD in the wings of the interferogram. The high intensity of the centerburst is caused by all wavelengths constructively interfering at ZPD. All the component sinusoidal waves that comprise the interferogram have ZPD as a common point. As OPD is increased, sinusoidal waves of different frequency get out of phase with each other and destructively interfere. As a result, the interferogram's intensity drops off rapidly as the mirror moves away from the ZPD and into the wings.

However it is actually difficult to have a beamsplitter of 0.5 transmission coefficient and mirrors that fully reflect the incident light beam. Eq.5.1.9 can be written in more general way[18]:

$$I(\delta) = 2(1-T)TI(\tilde{\nu}_o)cos2\pi\tilde{\nu}_o\delta \tag{5.1.10}$$

where T and R are the transmission and the reflection coefficiont of the beamsplitter respectively. Another point to consider about the beamsplitter is the fact that its response is not the same at all the wavenumbers, beamsplitters are generally wavenumber dependent. It is an important fact to take into account when we will consider a non-monochromatic light beam. It is also important to take into account two other effects of wavenumber dependency. The first one is due to the response of the detector which is not the same at different wavenumber. The second effect is a consequence of the amplifier of the detector that contain filters used to cut light radiation outside the spectral range of interest. Usually Eq.(5.1.8) is written in the following simple form, considered as the starting equation in Fourier transform spectroscopy:

$$I(\delta) = B(\tilde{\nu}_o) cos 2\pi\tilde{\nu}_o\delta \tag{5.1.11}$$

where $B(\tilde{\nu})$ is the irradiance of the source at wavenumber $\tilde{\nu}_o$ taking into account the modification induced by the instrument characteristics.

Let us denote the spectral intensity simply by $B(\tilde{\nu})$ and extend the whole description to non-monochromatic sources. Taking the advantage of the superposition principle, the intensity $I(\delta)$ recorded in the interferogram is then described by the integral of $B(\tilde{\nu})$ over all wavenumbers [18]:

$$I(\delta) = \int_{-\infty}^{\infty} B(\tilde{\nu}) \cos 2\pi\tilde{\nu}\delta d\tilde{\nu} \tag{5.1.12}$$

The intensity $I(\delta)$ is directly measurable quantity and thus real in the mathematics sense. As a consequence, $B(\tilde{\nu})$ to be Hermitian,

$$B^*(\tilde{\nu}) = B(-\tilde{\nu}) \tag{5.1.13}$$

is valid. With this relation and Euler's theorem, Eq(5.1.13) becomes

$$\begin{aligned}
I(\delta) &= 2\int_0^{\infty} Re[B(\tilde{\nu}).e^{i2\pi\nu\delta}]d\tilde{\nu} \\
&= 2\int_0^{\infty} [\{\frac{1}{2}B(\tilde{\nu}).e^{i2\pi\nu\delta}\}^* + \frac{1}{2}B(\tilde{\nu}).e^{i2\pi\nu\delta}]d\tilde{\nu} \\
&= \int_{-\infty}^{0} B(\tilde{\nu}).e^{i2\pi\nu\delta}d\tilde{\nu} + \int_0^{\infty} B(\tilde{\nu}).e^{i2\pi\nu\delta}d\tilde{\nu} \\
&= \int_{-\infty}^{\infty} B(\tilde{\nu}).e^{i2\pi\nu\delta}d\tilde{\nu}
\end{aligned}$$

Data acquisition yields the interferogram $I(\delta)$, which must be converted into a spectrum by means of a mathematical operation called Fourier transformation. Thus, by performing the Fourier transform of the interferogram $I(\delta)$, we obtain the spectral irradiance,

$$\Im I(\delta) = B(\tilde{\nu}) = \int_{-\infty}^{\infty} I(\delta) e^{-i2\pi\tilde{\nu}\delta} d\delta \tag{5.1.14}$$

As $I(\delta)$ is a continuous function, it can be represented as a sum of its even and odd components by

$$I(\delta) = I_e(\delta) + I_o(\delta) \tag{5.1.15}$$

where $I_e(\delta)$ is the even component of $I(\delta)$, and $I_o(\delta)$ is the odd component of $I(\delta)$.
For an even function $I_e(\delta) = I_e(-\delta)$ and for an odd function $I_o(-\delta) = -I_o(\delta)$.
So that,

$$I(-\delta) = I_e(\delta) + I_o(-\delta) \tag{5.1.16}$$

Adding Eqs.(5.1.15) and (5.1.16) gives

$$I(\delta) + I(-\delta) = 2I_e(\delta) \tag{5.1.17}$$

and thus,

$$I_e(\delta) = \frac{1}{2}[I(\delta) + I(-\delta)] \tag{5.1.18}$$

Subtracting Eqs.(5.1.15) and (5.1.16) results in

$$I_o(\delta) = \frac{1}{2}[I(\delta) - I(-\delta)] \tag{5.1.19}$$

Hence, Eq.(5.1.15) becomes

$$I(\delta) = \frac{1}{2}[I(\delta) + I(-\delta)] + \frac{1}{2}[I(\delta) - I(-\delta)] \tag{5.1.20}$$

Using Eq(5.1.14) and (5.1.20) we get:

$$\begin{aligned} B(\tilde{\nu}) &= \int_{-\infty}^{\infty}[I_e(\delta)+I_o(\delta)][cos2\pi\tilde{\nu}\delta - isin2\pi\tilde{\nu}\delta]d\tilde{\delta} \\ &= \int_{-\infty}^{\infty} I_e(\delta)cos2\pi\tilde{\nu}\delta d\delta + \int_{-\infty}^{\infty} I_o(\delta)cos2\pi\tilde{\nu}\delta d\delta - i\int_{-\infty}^{\infty} I_e(\delta)sin2\pi\tilde{\nu}\delta]d\tilde{\delta} - i\int_{-\infty}^{\infty} I_o(\delta)sin2\pi\tilde{\nu}\delta]d \end{aligned}$$

Since $cos2\pi\tilde{\nu}\delta$ is an even function and sin$2\pi\tilde{\nu}\delta$ an odd function, the following integral expressions will be zero:

$$\int_{-\infty}^{\infty} I_o(\delta)cos2\pi\tilde{\nu}\delta d\delta \quad = \quad i\int_{-\infty}^{\infty} I_e(\delta)sin2\pi\tilde{\nu}\delta d\delta = 0$$

Hence,

$$\begin{aligned} B(\tilde{\nu}) &= \int_{-\infty}^{\infty} I_e(\delta)cos2\pi\tilde{\nu}\delta d\delta - i\int_{-\infty}^{\infty} I_e(\delta)sin2\pi\tilde{\nu}\delta d\delta \\ &= 2\int_{2}^{\infty} I_e(\delta)cos2\pi\tilde{\nu}\delta d\delta - i2\int_{0}^{\infty} I_e(\delta)sin2\pi\tilde{\nu}\delta d\delta \end{aligned}$$

If the interferogram is real and even function, the spectrum is real and positive. That is,

$$B(\tilde{\nu}) = \int_{-\infty}^{\infty} I(\delta)cos2\pi\tilde{\nu}\delta d\delta \tag{5.1.21}$$

$$= 2\int_{0}^{\infty} I(\delta)cos2\pi\tilde{\nu}\delta d\delta \tag{5.1.22}$$

Eq.(5.1.22) shows that it is possible to perform measurements with infinite path differences, this would be equivalent of being able to measure an interferogram ranging from 0 to ∞.

5.2 Finite Resolution and Instrumental Line shape

Calculating a Fourier transform involves performing a mathematical integral on the interferogram. Ideally, the limits of integral should be plus and minus infinity. This means one

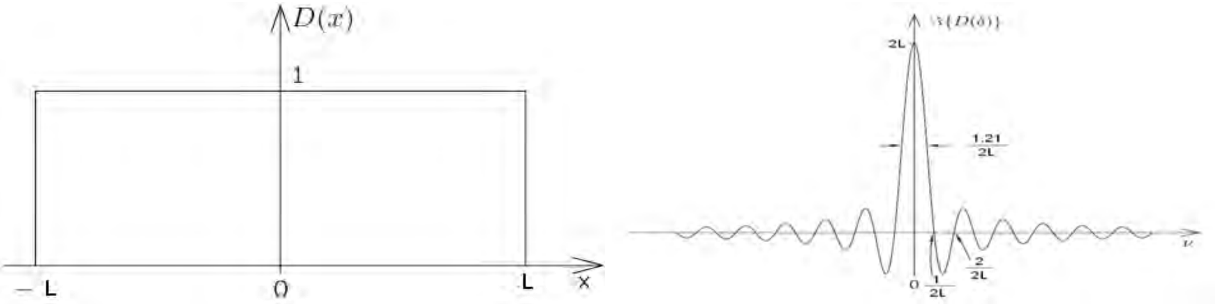

Figure 5.4: Left: the boxcar truncation function. Right: the Fourier transform of boxcar function.

must use an optical pathlength of infinity and collect an infinite number of data points to obtain an interferogram that will satisfy Fourier transform properly. This is impossible, so the interferogram and the integral must be truncated at some finite point, and the limits of interferogram are zero path difference(ZPD) and the maximum optical path difference (OPD). Thus, in the case of symmetrical OPD limits of $\pm\Delta$, Eq(5.1.22) becomes

$$B(\tilde{\nu}) = \int_{-\Delta}^{\Delta} I(\delta) cos 2\pi\nu\delta d\delta \tag{5.2.1}$$

which is equivalent to multiplying Eq(5.1.22) by the function

$$D(\delta) = \begin{cases} 1, & \text{if } |\delta| \leq \Delta; \\ 0, & \text{if } |\delta| > \Delta. \end{cases}$$

In view of the shape of this function (see Fig.5.4), $D(\delta)$ is often called a boxcar truncation function. Mathematically, an interferrogram $I_L(x)$, truncated at optical path difference x=L can be obtained by multiplying an interferrogram I(x) of infinite extension by a boxcar function D(x), i.e,

$$I_L(x) \;=\; I(x).D(x) \tag{5.2.2}$$

From this truncated interferrogram we can get the corresponding spectrum. According to the covolution theorem of Fourier analysis, the Fourier transform of I(x) measured with an infinitely long retardation and the Fourier transform of D(x). By definition, the Fourier transform of I(x) is the true spectrum, $B(\tilde{\nu})$,

$$B(\nu) = \int_{-\infty}^{\infty} e^{i2\pi\nu x} D(x) dx \tag{5.2.3}$$

Thus, the Fourier transform $G(\nu)$ of the truncated interferrogram $I_L(x)$ is

$$\begin{aligned} G(\nu) &= \int_{-\infty}^{\infty} e^{i2\pi\nu x} I_L(x) dx \\ &= \int_{-\infty}^{\infty} e^{i2\pi\nu x} I(x).D(x) dx \\ &= \int_{-\infty}^{\infty} B(k) d(\nu - k) dk \\ &= B(\nu) * d(\nu) \end{aligned}$$

Thus, according to this equation, the spectrum of a finite interferrogram can thus be obtained by convolving the spectrum $B(\nu)$ corresponding to the infinite OPD with the FT of the boxcar function. We can also see a very sharp, single spectral component that enters the interferogram is broadened by the FT-IR spectrometer according to the function D(x), i.e $D(\delta)$ determines how the spectrometer distorts an incoming sharp spectral line. For this reason, $D(\delta)$ is called instrumental line shape (ILS) function. The analytical form of the ILS corresponding to the boxcar truncation is derived as follows:
Using the boxcar truncation function and Eq(5.2.3), we get

$$\begin{aligned} \Im\{D(\delta)\} &= \int_{-L}^{L} 1.e^{-i2\pi\bar{\nu}\Delta} d\delta \\ &= \int_{-L}^{L} \cos(2\pi\bar{\nu}\Delta) + i \int_{-L}^{L} \sin(2\pi\bar{\nu}\delta) d\delta \\ &= \int_{-L}^{L} \cos(2\pi\bar{\nu}\Delta) \\ &= 2L \frac{sin(2\pi\bar{\nu}\Delta)}{2\pi\bar{\nu}\Delta} \end{aligned}$$

Therefore,

$$\Im\{D(\delta)\} = 2\Delta sinc(2\pi\bar{\nu}\Delta) \tag{5.2.4}$$

This function is shown in Fig.5.4. It is centered about $\bar{\nu} = 0$ and intersects the $\bar{\nu} - axis$ at $\bar{\nu} = \frac{n}{2\Delta}$, where n=1,2,3,..., so that the first intersection occurs at a wavenumber of $(2\Delta)^{-1}$. Besides a main maximum centered about $\nu = 0$, numerous additional peaks, called side lobes or 'feet' are present. These side lobes cause a 'leakage' of the spectral intensity, i.e, the intensity is not strictly localized but contributes also to these sidelobes. The largest sidelobe amplitude is 22% of the main lobe amplitude. As the sidelobes do not correspond to actually measured information but rather represent an artifact due to the abrupt truncation at x=L, it is desirable to reduce their amplitude. The process which attenuates the spurious 'feet' in the spectral domain is known as 'apodization' (originating from the Greek word $\alpha\pi 0\delta$, which means 'removal of the feet')[20].

5.3 Apodization

An unfortunate outcome of truncating the integral 5.1.22 is that the line shape of the peaks in the infrared spectrum are affected. Rather than obtaining the true peak shape, the absorptance bands are surrounded by sidelobes, which are sinusoidal undulations in the baselines. In order to reduce this effect, one can try to soften the cut-off of the interferogram at the maximum OPD by multiplying it with an apodization function. Apodization function is a weighting function whose value decreases with increasing OPD. As a result, it decreases the effect of truncation of the interferogram at L. The effect of apodization on an ideal monochromatic laser beam is illustrated in Fig.5.5a for the boxcar and Fig.5.5b for triangular apodization functions. Thus, apodization functions vary in how well they suppress sidelobes and how muchthey degrade resolution which will be discussed in the next they degrade resolution which will be discussed in the next section. Fig.5.5 shows that there is generally a trade-off between sidelobe minimization and improved line shape[21].

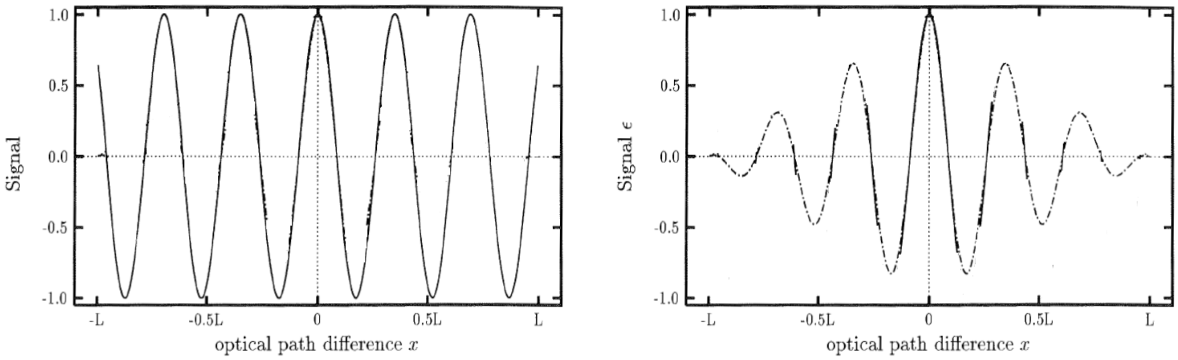

Figure 5.5: The effect of apodization on the line shape of an ideal monochromatic spectral line. a) The recorded interferogram is shown after apodization with boxcar apodization function, b)The recorded interferogram is shown after apodization with triangular function.

5.4 Apodization and Spectral Resolution

Previous results revealed that all apodization functions produce an ILS with a lower sidelobe level than the sinc function. However, one also sees that the main lobes of all ILS's in Fig.5.5b are broader than that of the sinc function in Fig.5.5a. Apodization functions vary in how well they suppress sidelobes, and how much they degrade resolution. There are different criteria used to decide when closely neighbored spectral lines are said to be just resolved. The well known are the Rayleigh criterion and FWHW criterion.

According to Rayleigh, two adjacent spectral lines of equal intensity, each with a $sinc^2$x ILS (which is the Fourier transform of the triangular apodization function), are considered to be just resolved when the center of one line is at the same frequency as the first zero value of the ILS of the other. However, if the same criteria is applied to a line having a sincx ILS, it is found that the two lines are not resolved, as shown in the Fig.5.6. Thus, the Full width at half height (FWHH) of the ILS defines the best resolution. This is because if two spectral lines are to appear resolved from one another, they must be separated by at least the distance of their FWHH, otherwise no 'dip' will occur between them. The

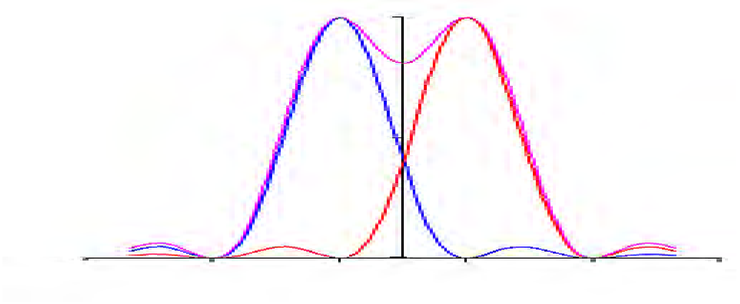

Figure 5.6: The resultant of two sinc^2 functions

function sincx, having the Fourier transform of the boxcar function, has a value of 0.5 at x=0.60335π. This yield the FWHH of the boxcar apodization to be

$$\Delta\nu = 2(\frac{0.603\pi}{2\pi L}) = \frac{0.603}{L}$$

But two lines with sincx line shapes are not resolved when they are separated by this amount. In practice, a dip of 20% is found when the two lines with a sincx ILS are separated by $\frac{0.73}{\Delta}$. Similarly, the function $sinc^2$x, which is the Fourier transform of the triangular apodization function, equals 0.5 at $x = 0.885885\pi$. And thus, the FWHH becomes

$$\Delta\nu = \frac{0.9}{L}$$

Hence, the resolution of the Fourier transform spectrometer is proportional to the maximum OPD. In the case of the IFS120M, the maximum OPD is 250cm. Consequently, the achievable resolution is $0.002cm^{-1}$ according to the Rayleigh criteria or $0.0024cm^{-1}$ if FWHH is applied. The choice of a particular appodization function depends therefore on what one is aiming at. The apodization functon that provides the heighest resolution, and does the worst job of suppressing sidelobes, is the boxcar function. Since our interest is to high resolution, we can live with the existence of sidelobes[21].

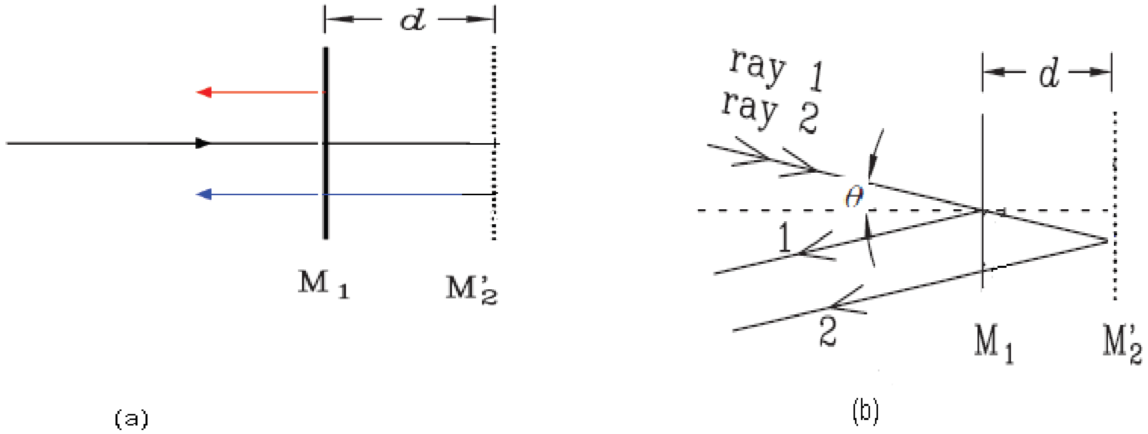

Figure 5.7: Optical path difference for different cases: a)ideal case presented on fig and b)rays 1 and 2 arrive in the mirrors at the angle θ.In both pictures,M_1 is the mirror , and M_2' is the image of the mirror M_2, of an interferometer.

5.5 Effects of an Extended Source

5.5.1 Circular Aperture

Considering the ideal spectrometer at the beginning, the light beam was assumed to be perfectly collimated. The only way to have such a light beam is using a punctual source, placed at the focus of a collimating lens or mirror. In this section we will deal with the effects of using a realistic source (i.e. an extended source) on the interferogram. Let us consider the basic description of the Michelson interferometer given on Figure 1.1b with a non-collimated beam. Imagine two rays coming to the two mirrors making angle α with respect to the optical axis. Taking the image of one of the mirrors formed by the beamsplitter in such a way that this image lies in the same direction as the other mirror, as shown in Fig.5.7b. If the distance between them is d, then the difference of the paths is $2d\cos\theta$. Fig.5.7a shows that the OPD for the perfectly collimated beam is 2d. Thus, the OPD is changed from 2d to $2d\cos\theta$. For a given wavenumber one can see that there

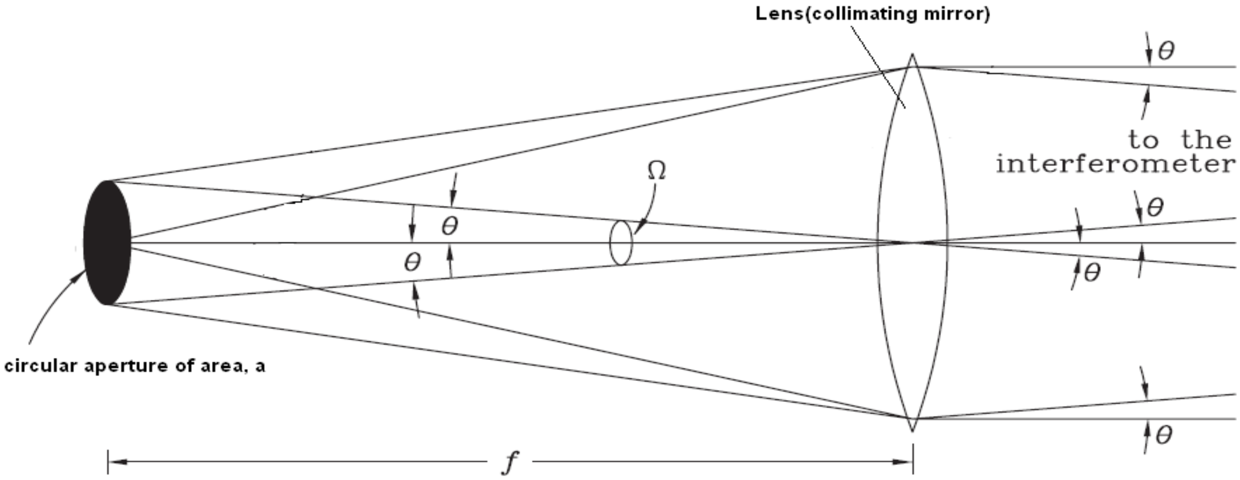

Figure 5.8: Extended radiation source at the focal point of the collimator lens with the focal length f. The area of the source is a. $\Omega = \pi\theta^2$ is the solid angle of the source.

is no longer a single OPD but an infinite set of path differences corresponding to each of the values of the divergent angle α. Let us consider a small circle in a circular radiation source, shown in Fig.5.8. The center of the circle is the center of the radiation source. Let the radial angle of the circle be θ, and the solid angle of the source limited by the circle Ω'.

is

$$r \approx f\theta$$

The area of the circle,

$$a = \pi r^2 \approx \pi(f\theta)^2$$

Thus the solid angle is

$$\Omega' \approx \frac{\pi(f\theta)^2}{f^2} = \pi\theta^2$$

Consequently,

$$\begin{aligned} \cos\theta &\approx \frac{f}{\sqrt{(f\theta)^2+f^2}} = \frac{1}{\sqrt{1+\theta^2}} \\ &\approx \frac{1}{\sqrt{1+\frac{\Omega'}{\pi}}} \approx 1-\frac{\Omega'}{2\pi} \end{aligned}$$

Thus, the OPD of the rays travelling in the direction α with respect to the optical axis is [22]

$$xcos\theta \approx x(1-\frac{\Omega'}{2\pi}) \tag{5.5.1}$$

Every point of an extended radiation source can be considered as a separate point source. If the radiation source is fully incoherent, we can expect that every source point follows the above equation separately. The optical path difference of radiation which is emitted from a circle which makes an angle α with respect to the optical axis is

$$x_\theta = xcos\theta \approx x(1-\frac{\Omega'}{2\pi})$$

where Ω' is the solid angle limited by the circle. Consequently the intensity which arrives in the detector from a circle at the angle α is

$$I_\theta(x) = \int_{-\infty}^{\infty} E(\nu)e^{i2\pi\nu x_\theta}d\nu$$

The whole intensity in the detector is obtained by integration over the whole solid angle of the radiation source:

$$\begin{aligned} I_\Omega(x) &= \int_0^\Omega I_\theta(x)d\Omega \\ &= \int_0^\Omega \int_{-\infty}^{\infty} E(\nu)e^{i2\pi\nu x(1-\frac{\Omega/}{2\pi})d\nu d\Omega/} \\ &= \int_{-\infty}^{\infty} \frac{E(\nu)}{-i\nu x}[e^{i2\pi x(1-\frac{\Omega}{2\pi})} - e^{i2\pi\nu x}]d\nu \\ &= \int_{-\infty}^{\infty} \frac{-E(\nu)}{i\nu x}(e^{-i\nu x\frac{\Omega}{2}} - e^{i\nu x\frac{\Omega}{2}})e^{i2\pi\nu x - i\nu x\frac{\Omega}{2}} \\ &= \int_{-\infty}^{\infty} \frac{E(\nu)}{i\nu x}2isin(\frac{\nu x\Omega}{2})e^{i2\pi\nu x-\frac{i\nu x\Omega}{2}}d\nu \end{aligned}$$

Therefore,

$$I_\Omega(x) = \Omega \int_{-\infty}^{\infty} E(\nu) sinc(\frac{\nu x \Omega}{2}) e^{i2\pi\nu x(1-\frac{\Omega}{4\pi})} d\nu \tag{5.5.2}$$

And Ω can be defined as follows:

$$\Omega \;=\; \int_0^{2\pi} d\varphi \int_0^{\alpha} \sin\theta d\theta = 2\pi(1-\cos\theta) \tag{5.5.3}$$

Considering weak divergence (α is small), it is possible to show, using Eq(5.5.3),that:

$$\Omega \;\approx\; \pi \tan^2\theta \tag{5.5.4}$$

Using some trignometric knowledge, Eq(5.5.4) and Fig.5.8 yields:

$$\Omega \;\approx\; \frac{\pi r^2}{f^2} \tag{5.5.5}$$

Therefore Eq(5.5.2) can be written as a function of the optical elements:

$$I(x) = \frac{\pi r^2}{f^2} \int_{-\infty}^{\infty} E(\nu) sinc(\frac{\nu x \pi r^2}{2f^2}) e^{i2\pi\nu x(1-\frac{r^2}{4f^2})} d\nu \tag{5.5.6}$$

We can see from Eq(5.5.6) that the light divergence induces two notable effects:

- There is a shift of the measured wavenumber from ν to ν'=$\nu(1-\frac{r^2}{4f^2})$; and
- The interferrogram is multiplied by a sinc function for each wavenumber. It corresponds to a convolution of the spectrum with a box function of width $\triangle\nu = \frac{\nu r^2}{2f^2}$ for each wavenumber.

We can see that another effect caused by the extended source, besides the shift of the measured wavenumber, is the broadening of the spectral lines. This is said to be aperture broadening[22].

5.5.2 Effect of beam divergence through the interferometer

In Section(5.5.1) it was stated that the beam through the interferometer must be perfectly collimated. In practice, a perfectly collimated beam could only be generated from an infinitely small source, so that no signal would be measured by the detector. To measure

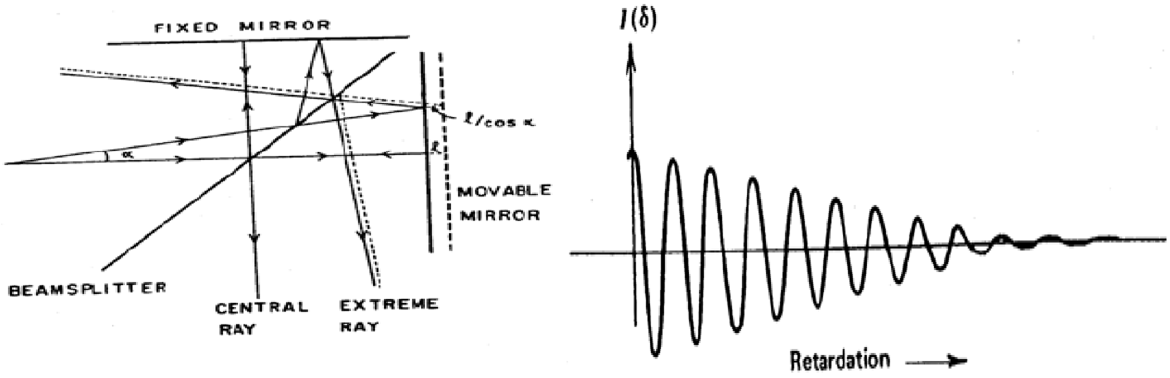

Figure 5.9: Left: schematic representation of a diverging beam passing through a Michelson interferometer. The angle between the central ray and the extreme ray is α, and the distance moved by the mirror is ℓ, corresponding to an optical retardation of 2ℓ for the central ray. Right: appearance of the interferogram of a beam of monochromatic radiation diverging rapidly as it passes through the interferometer.

a signal at the detector, a source of finite size must be used. In this section, the limits on source size are discussed, so that the largest possible throughput of radiation may be passed through the interferometer without degrading the spectrum in any way.

Consider the effect of a non-collimated beam of monochromatic light of wave length λ passing through the interferometer with a divergence half angle α. At zero retardation, the path difference between the central ray passing to the fixed and movable mirrors is zero, and there is no path difference for the extreme rays. Thus, there will be constructive interference for both beams. Let the movable mirror now be moved a distance ℓ(see Fig.5.9a).

The increase in retardation for the central ray is $\frac{2\ell}{cos\alpha}$. Therefore a path difference x has been generated between the central and extreme ray, where

$$
\begin{aligned}
x &= \frac{2\ell}{cos\alpha} - 2\ell \qquad (5.5.7)\\
&= 2\ell\frac{\ell - cos\alpha}{cos\alpha} \qquad (5.5.8)
\end{aligned}
$$

If α is small,

$$1 - cos\alpha \sim \frac{1}{2}\alpha^2 \tag{5.5.9}$$

And,

$$cos\alpha \sim 1 \tag{5.5.10}$$

Thus,

$$x = \ell\alpha^2 \tag{5.5.11}$$

As ℓ, the extreme rays will be out of phase with the central ray for the first time when

$$x = \frac{1}{2}\lambda \tag{5.5.12}$$

At this point, the fringe contrast at the detector completely disappears, and any further increase in ℓ will add no further information to the interferogram (Fig.5.9b). By Eq(5.5.12)

$$\ell = \frac{1}{2\triangle\bar{\nu}} \tag{5.5.13}$$

Using Eq(5.5.11) and (5.5.13)

$$\ell\alpha^2 = \frac{1}{2}\lambda = \frac{1}{2\nu} \tag{5.5.14}$$

And thus,

$$\ell\alpha_{max}^2 = \frac{1}{2\nu_{max}} \tag{5.5.15}$$

where α_{max} is the greatest beam half angle that can be passed through the interferometer with highest wavenumber ν_{max}. Therefore, using Eq(5.5.13) and (5.5.15), we get

$$\alpha_{max} = (\frac{\triangle\nu}{\nu_{max}})^{\frac{1}{2}} \tag{5.5.16}$$

or,

$$\triangle\nu = \frac{1}{2}\nu_{\circ}\alpha_{max}^2 \tag{5.5.17}$$

The maximum solid angle that can be tolerated is therefore

$$\Omega_{max} = 2\pi\alpha^2 = 2\pi\frac{\triangle\nu}{\nu_{max}} \qquad sterdians(sr) \tag{5.5.18}$$

The effect of having large solid angle is similar to the effect of appodization. For this reason, it has been called self-apodization [22].

Besides setting a limit on the resolution achievable, beam divergence also has the effect of shifting the wavenumber of the computed spectral line from its true state. Consider the interferograms due to central and extreme rays from a monochromatic source. The wavelength of the interferogram for the extreme ray is longer than that of the central ray. For a particular divergence half-angle α, the path difference between the central and extreme rays at a retardation $\Delta = 2\ell$ is given by[22]

$$x = \frac{1}{2}\alpha^2\Delta \tag{5.5.19}$$

Between $\delta = 0$ and this retardation there are n maxima in the (cosine) interferogram for the central ray, where

$$\Delta = n\lambda = \frac{n}{\nu} \tag{5.5.20}$$

For the extreme rays there is an increased retardation $(\Delta+x)$, and the effective wavelength of this ray is therefore changed to a value of λ', where

$$\Delta + x = n\lambda' = \frac{n}{\nu'} \tag{5.5.21}$$

Using Eq(5.5.19),(5.5.20) and (5.5.21), we get

$$\frac{\nu'}{\nu} = \frac{\Delta}{\Delta + x} = \frac{1}{1 + \frac{\alpha^2}{2}}$$

If α is small,

$$\frac{\nu'}{\nu} = 1 - \frac{1}{2}\alpha^2$$

Thus,

$$\nu' \;=\; \nu\{1-\frac{1}{2}\alpha^2\}$$

To a first approximation, the wavenumber of the line computed from this interferogram, ν'', is the mean of the wavenumbers of the central and extreme rays, that is,

$$\begin{aligned}\nu'' &\approx \frac{\nu+\nu'}{2} = \nu\{1-\frac{\alpha^2}{4}\}\\ &= \nu\{1-\frac{\Delta\nu}{4\nu_{max}}\}\end{aligned}$$

5.6 Mobile Mirror Misalignment

The alignment of the moving mirror in a Michelson interferometer can affect the quality of the spectrum. If the moving mirror is held at a different angle than the fixed mirror relative to the plane of the beamsplitter, then the image of the beam to the moving mirror will hit the plane of the detector at a different position than the beam that travelled to the fixed mirror, see Fig.5.10a. Consider the concentric rings forming the image of an extended source at the detector. If the images from the fixed and moving mirrors are not centered at the point on the detector, fringe contrast can be drastically reduced. Since the diameter of any ring is dependent on the wavelength of the retardation, short wavelength radiation from a polychromatic source will be affected more than long wavelength radiation(see Fig.5.10a) Spectra of a Globar source are shown for which the two mirrors in the interferometer are (a) well aligned, (b) in fair alignment, and (c) badly aligned. It can be seen that if the interferometer is out of alignment, the wavenumber at which the greatest intensity in the spectrum occurs is reduced. When the interferometer is badly out of alignment, all the information at high wavenumber is lost. To obtain good spectra at short wavelength, it is vital that the mirrors of the interferometer are maintained in good alignment[18].

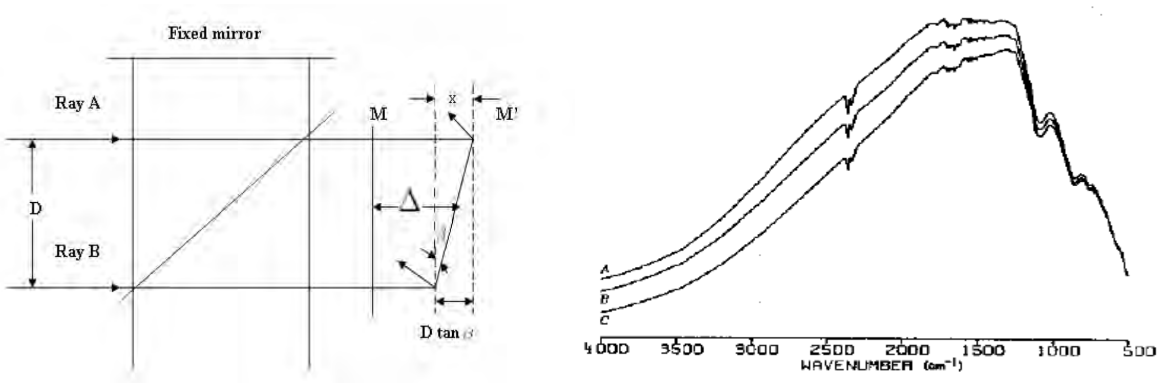

Figure 5.10: Left: schematic representation to demonstrate the effect of changing the plane of the moving mirror of an interferometer during a scan. Ray A and B represent the extreme rays of the collimated beam passing through the interferometer, and β is the angle by which the plane of the moving mirror tilts. Right: single-beam spectra measured (A) with the fixed mirror of the interferometer in a good alignment with the moving mirror, (B) with fixed mirror slightly out of alignment, and (C) with the fixed mirror well out of alignment.

5.7 Tilt Compensation

If the moving mirror of a Michelson interferometer is tilted, the amplitude of the interferogram is reduced. But when cube-corner retroreflectors is used as the moving element, the effect of tilt is essentially eliminated. The principle behind the operation of a cube corner is shown in Fig.5.11a. Even though cube corners eliminate the effect of mirror tilt, lateral displacements produce a shear that has a similar effect on the the interferogram. In practice, it is easier to meet the tolerance on lateral displacements than on tilts, so that retroreflectors experimentally have a definite advantage over plane mirrors[18].

5.8 Beamsplitters for Michelson interferometers

Consider a beam of monochromatic radiation intensity I entering a Michelson interferometer for which the beamsplitter has a reflectance R and a transmittance T. If there is no

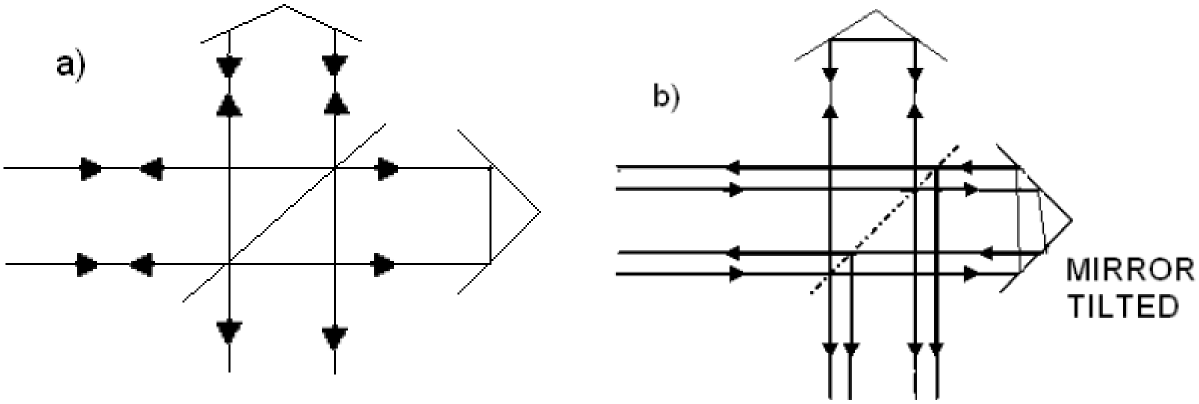

Figure 5.11: Principle of the corner retroreflector: a)Both retroreflectors are in good alighment so that there is no essential difference from the case of plane mirror Michelson interferometer. b) one of the retroreflectors is tilted. The concept of the "roof" retroreflector shown in this figure can be extended into three dimensions through the use of cube corners.

absorption of radiation,

$$R + T = 1 \tag{5.8.1}$$

As it is given in the Fig.5.12a, the intensity of the beam transmitted to the detector (the dc component of the interferogram) is (2RT)I, while that of the beam returning to the source is $(R^2 + T^2)I$. In order that there is no energy loss occurring at the beamsplitter, the sum of the intensities of these beams must be equal to I. For an ideal beamsplitter, the interferogram is given by the Eq.(5.8.1). The effect of nonideality of the beamsplitter material may be allowed for by multiplying the amplitude of the ac interferogram by a factor of $\eta(\nu)$, which is less than 1, so that

$$I(\delta) = 0.5\eta(\nu)I(\nu)cos2\pi\nu\delta$$

where $\eta(\nu) = 4RT$ and is known as the relative beamsplitter efficiency. For infrared spectrometry, $\eta(\nu)$ should be as close to unity as possible over as wide a spectral range as possible. The phase delay due to the beamsplitter is kept very low by adding compensator made of the same material as the beamsplitter substrate and of the same thickness

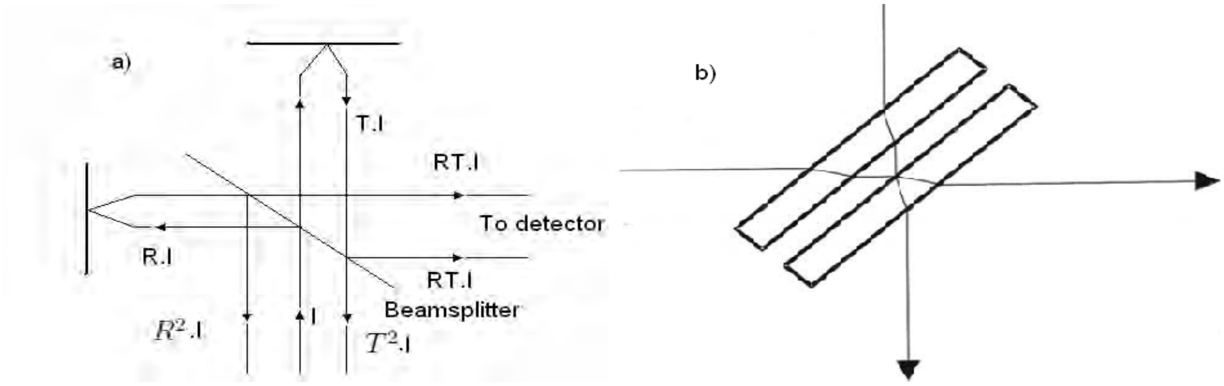

Figure 5.12: a)Modified ray diagram of a michelson interferometer in which beams traveling in opposite directions have been separated for clarity.b)Beamsplitter consisting of two plates(compensator and beam deviding plates)

under the same angle into the interferometer arm where light crosses the beamsplitter substrate only once. Generally, its reflectance is determined by the refractive index of the material, n, the thickness of the film, d(in cm), the angle of incidence of the beam, θ, and the wavenumber of the radiation, ν. The effect of internal reflections must be considered, together with the fact that phase shift 180° occur at external reflection surfaces whereas no phase shifts occur for internal reflection. The ray that is reflected from surface of the beamsplitter can interfere with the parallel ray, which has undergone internal reflection. Germanium(n=4.0) or silcon(n=3.6) films are generally used for mid-infrared spectrometery. The plate on which the film is deposited depends on the spectral range of interest[18].

5.9 Detectors

Infrared detectors are classified into thermal types and quantum types. Thermal detectors use the infrared energy as heat and their photo sensitivity is independent of wavelength. Thermal detectors do not require cooling, but have disadvantages that response time is slow and detection capability is low. Detection of radiation using quantum detector depends on the interaction of radiation with the electrons to be excited to a higher energy states. These quantum effects depend on the quantum nature of radiation. The energy of each photons is proportional to its wave number. A transition of electrons from one state to another will only occur if the wavelength is less than some critical value. In an n-type semiconductor, the electrons in the valence band are unable to contribute to the conduction. If excited to the conduction band, they can act as current carriers, as can the hole left behind in the valence band. To detect mid-infrared wavelength, a very small amount of excitation energy is needed. This results in the citation of electrons by thermal agitation of the solid. This is a random effect giving rise to electrical noise in the output. For good sensitivity,therefore it is necessary to cool the element. Thus, quantum detectors offer higher detection performance and a faster response speed, although their photo sensitivity is dependent on wavelength. In general quantum detectors must be cooled for accurate measurement. Major characteristic indicating infrared detectors performance are photo sensitivity, noise equivalent power (NEP) and detectivity(D^*)[23].

5.9.1 Photo Sensitivity (responsivity)

Photo sensitivity is the output voltage (or current) per watt of incident energy when noise is not a consideration[23]:

$$R = \frac{S}{PA} \tag{5.9.1}$$

where S is signal output (V) P is incident energy ($\frac{W}{cm^2}$) and A is detector active area (cm^2). Output signals from photovoltaic detectors are usually extracted as photocurrent. When light at a given wavelength enters a photovoltaic detector, the photocurrent I_{sc} is expressed by the following equation[]:

$$I_{sc} = \eta q \frac{PA}{h\frac{c}{\lambda}} = \frac{\eta q PA\lambda}{hc} \tag{5.9.2}$$

where q is electron charge η is quantum efficiency. Thus, the photo sensitivity R_λ is as follows:

$$R_\lambda = \frac{I_{sc}}{PA} = \frac{\eta q\lambda}{hc} = \frac{\eta\lambda}{1.24} \tag{5.9.3}$$

5.9.2 Noise Equivalent Power (NEP)

The sensitivity of infrared detectors is commonly expressed interms of the noise equivalent power(NEP) of the detector[23],

$$NEP = \frac{PA}{S/N \cdot \sqrt{\Delta f}} \tag{5.9.4}$$

where N is Noise output and Δ f is Noise bandwidth

5.9.3 Detectivity (D^*)

Detectivity is the photo sensitivity per unit active area of a detector. In many detectors, NEP is proportional to the square root of the detector active area []. So, generally,

$$D^* = \frac{S/N \cdot \sqrt{\Delta f}}{P.\sqrt{A}} = \frac{\sqrt{A}}{NEP}$$

Thus, it can be said that a larger value of D^* indicates a better detector element[18].

5.10 Parabolic Mirrors

Focusing features of optical elements should be independent of wavelength. This is possible for mirrors only. Light from a point source placed in a focus of a parabola (see Fig.5.13b) will be transformed after reflection into an ideally parallel beam. Accordingly, a parallel beam will be focused into a tiny focal spot. This is true for any section of the parabola. So, an off-axis section of the paraboloidal mirror can be cut out for convenience(see Fig.5.13b). The arrangement shown in the Fig.5.13b is described as a 90° off-axis mirror since the ray striking the center of the aperture and parallel to the main axis turns exactly at 90° and turns to a focal point. The distance from the point on the surface of the parabola at the center of the aperture, to the focal point, is the effective focal length(EFL) and it is exactly two times the focal length of the parabola:

$$EFL = 2f$$

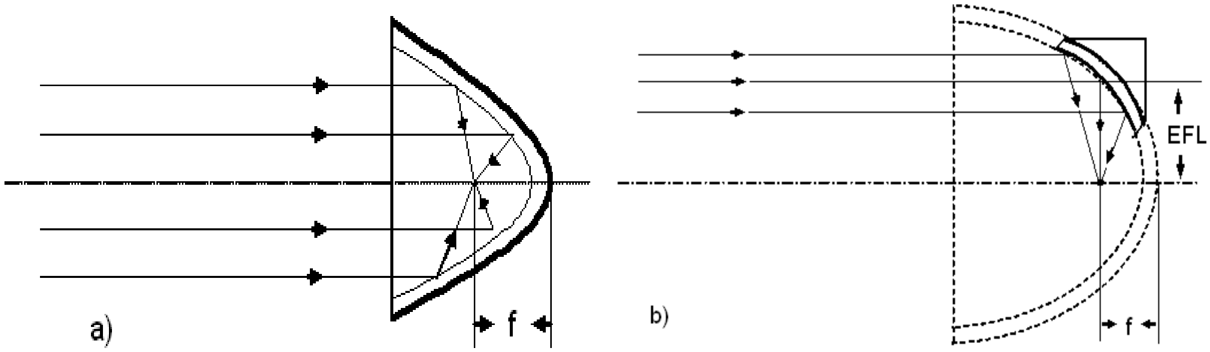

Figure 5.13: a)Light from a point source placed at the focus of parabola. b)section of off-axis parabola

If a finite source size, instead of a point source, is placed in the focal point of the parabola, the reflected beam will not be ideally parallel any more. On top of that it will suffer significant aberrations. Accordingly, a parallel incoming beam will be focused into, not a spot, but a blurred spot. The FTIR instruments use gold coated parabolic mirrors for focusing light external to the detector. These gold coated mirrors are very broadband, from 0.7 to 10 microns they reflect more than 98%, and it stays in this range up to 25 microns (bear in mind that for wavelengths shorter than 0.6 micron, gold is a bad reflector; its reflectivity drops abruptly to less than 40%. An important feature of mirrors in general also is that they do not have any dispersion; there is no chromatic aberration so the focal spot stays at the same place for any wavelength. They do have monochromatic aberrations[18].

5.11 Phase Effects

Up to now, the interferrogram was assumed to be an even function and therefore spectrum could be obtained using Eq(5.1.22). In practice, the interferrogram is not an even function and cannot be retrieved from the cosine Fourier transform of the spectrum. A phase shift term appears in the cosine function of Eq(5.1.22). Such an effect, known as phase error, appears mainly because of sampling effects (the zero path difference point is not accurately

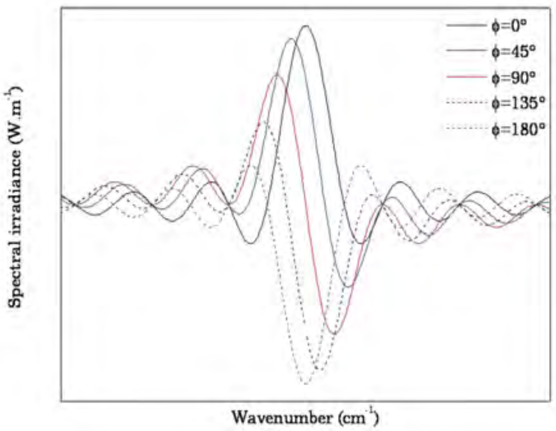

Figure 5.14: Effect of the phase error ϕ on the cosine Fourier transform of a boxcar truncation function for several values of ϕ

known), optical elements(some dispersive phenomena exist) and electronic filters designed to remove high-frequency noise from the interferogram have the effect of putting wave number dependent phase lag. Hence, an additional term often has to be added to the phase angle to describe the actual measured interferogram. The effect of phase shifts on an uncorrected interferrogram and , therefore, the spectrum, can be seen in Fig.5.14:

$$F(\tilde{\nu}) = 2\Delta \frac{\sin(2\pi\tilde{\nu}\Delta \pm \phi(\tilde{\nu})) \mp \sin\phi(\tilde{\nu})}{2\pi\tilde{\nu}\Delta} \tag{5.11.1}$$

Strictly speaking, the relation given in Eq(5.2.4) is exact for monochromatic interferograms only, because dispersion in the beamsplitter or other optical elements like filters introduce wavenumber dependent phase delay that affect the shape of a typical broadband interferogram. Thus, the calculated spectrum in Eq(5.11.1) is composed of a real($\Re(\tilde{\nu})$) and an imaginary part($\Im(\tilde{\nu})$):

$$\begin{aligned} E(\tilde{\nu}) &= \Re(\tilde{\nu}) + i\Im(\tilde{\nu}) && (5.11.2)\\ &= |E(\tilde{\nu})|\, cos(\phi(\tilde{\nu})) + i\,|E(\tilde{\nu})|\, sin(\phi(\tilde{\nu})) && (5.11.3)\\ &= |E(\tilde{\nu})|\, e^{i\phi(\tilde{\nu})} && (5.11.4)\end{aligned}$$

where $\phi(\tilde{\nu})$ is the phase spectrum and $\mid E(\tilde{\nu}) \mid$ is the amplitude spectrum. The phase spectrum can be obtained from Eq(5.11.2) as:

$$\phi(\tilde{\nu}) = \arctan \frac{\Im(\tilde{\nu})}{\Re(\tilde{\nu})} \tag{5.11.5}$$

In the most commonly used method of phase correction, which was developed by Mertz, the amplitude spectrum is calculated in reference to the largest data point in the interferogram. The calculated amplitude spectrum is then multiplied at each frequency by the cosine of the difference between the measured phase angle and the reference phase angle to yield the true phase-corrected spectrum [24].

5.12 Discrete Fourier Transform(DFT)

In practical measurements we do not deal with functions which are expressed as explicit mathematical expressions whose Fourier transforms are known. Instead, Fourier transforms are computed numerically. In practice, the measurement of a signal usually gives us a finite number of data, measured at discrete points. Consequently, also the integrals of Fourier transforms must be approximated by finite sums. The integral from $-\infty$ to ∞ is replaced by a sum from 0 to N-1. Calculation of a DFT is possible, if we record the signal I(x) at N equally spaced sampling points,

$$X_n = n\Delta x, \qquad n = 0, 1, ..., N-1 \tag{5.12.1}$$

The spectrum calculated from the discrete signal samples is given by a discrete approximation of $E(\nu)$ in Eq(5.14.2). The obtained spectrum is sampled in equal interval of $\Delta\nu$, so that,

$$\nu = k\Delta\nu \tag{5.12.2}$$

where k is non-negative integer.

Thus, the discrete version of Fourier transform is

$$S(k.\Delta\nu) = \sum_{n=0}^{N-1} I(n\Delta x)e^{i2\pi n\frac{k}{N}} \tag{5.12.3}$$

The spacing $\Delta\nu$ in the spectrum is related to Δx by

$$\Delta\nu = \frac{1}{N\Delta x} \tag{5.12.4}$$

Alternatively, if the set $S(k.\Delta\nu)$ of Fourier coefficients is known, we can construct the interferrogram $I(n\Delta x)$ by the inverse DFT(IDFT) equation as

$$I(n\Delta x) = \frac{1}{N}\sum_{n=0}^{N-1} S(k.\Delta\nu)e^{-i2\pi n\frac{k}{N}} \tag{5.12.5}$$

In practice, Eq(5.12.5) is seldom used directly because it is highly redundant. Instead a number of the so called fast Fourier transforms (FFT) are in use, the most common of which is the Cooley-Tukey algorithm. The aim of these FFT is to reduce the number of complex multiplications and sine and cosine calculations appreciably leading to a substantial saving of computer time. The price paid for the speed is that the number of interferrogram points N can not be chosen at will, but depends on the algorithm. In the case of the Cooley-Tukey algorithm, which is used by most FTIR manufacturers with slight modifications, N must be a power of two. For this reason and from the relation(5.12.4) it follows that spectra taken with a laser cotrolled FTIR spectrometers will show a sample spacing of

$$\Delta\nu = \frac{m * laserwavenumber}{2^N} \tag{5.12.6}$$

It should be noted that DFT only approximates the continuous Fourier transform, although it is a very good approximation if used with care. Blind use of Eq(5.12.6), however, can lead to three well-known artifacts: the picket-fence effect, aliasing and leakage[18].

5.13 Picket-Fence Effect: Zerofilling

The picket-fence effect becomes evident when the interferrogram contains frequencies which do not concide with the frequency sample points $k * \Delta\nu$. If, in the worst case, a frequency component lies exactly halfway between two sample points, an erroneous signal reduction by 36% can occur. In other words, one seems to be viewing the true spectrum through a picket fence, thereby clipping those spectral parts lying behind the pickets, i.e, between the sampling positions $k * \Delta\nu$. In practice, the problem is less extreme than stated above if the spectral components are broad enough to be spread over several sampling positions. The picket-fence effect can be overcome by adding zeros to the end of the interferogram before DFT is performed, thereby increasing the number of points per wave number in the spectrum. Thus zerofilling the interferogram has the effect of interpolating the spectrum, reducing the error. As a rule of thumb, one should always at least double the original interferogram size for practical measurements by zerofilling it, i.e, one should choose a zerofilling factor(ZFF) of two. In those cases, however, where the expected line width is similar to the spectral sample spacing (as e.g. in case of gas-phase spectra), a ZFF value of up to 8 may be appropraite. In the general case, if$(2^m - 1)$N zeros are added to an N-point interferogram, where m is an integer greater than 1, the bandwidth after the complex FFT will contain $2^{(m-1)}$N points, of which $\frac{1}{2}$N are linearly independent and the rest are interpolated. In addition, zerofilling does not introduce any error, for the fact that it does not change the ILS. To compute a spectrum from a zero-filled interferogram so that it has the same resolution and ILS as the spectrum computed from boxcar apodized, non-zero filled interferogram, only the measured data should be multiplied by the apodization function [].

5.14 Aliasing

The Eq(5.12.2) is the basic DFT-equation which describes how a spectrum sampled at wavenumbers $k.\Delta\nu$ can be computed from an interferrogram sampled at optical path differences $n.\Delta x$. Clearly we see that, the spectrum of a signal sampled with the sampling interval Δx is periodic with the period $\frac{1}{\Delta x}$, i.e,

$$E(\nu - \frac{k}{\Delta x}) \quad = \quad E(\nu) \tag{5.14.1}$$

with all integers k. In the calculated spectrum, the contributions of all the waves at frequencies $\nu - \frac{k}{\Delta x}$ are therefore superimposed. Thus, the spectrum computed from the sampled, not truncated interferogram is

$$E^{\Delta x}(\nu) \quad = \quad \sum_{n=-\infty}^{\infty} E(\nu - \frac{k}{\Delta x}) \tag{5.14.2}$$

If the signal, in addition to being discrete, is also truncated, we obtain that

$$\begin{aligned}
E_L^{\Delta x} \quad &= \quad \sum_{n=-\infty}^{\infty} E(\nu - \frac{k}{\Delta x}) = \sum_{-\infty}^{\infty} \delta(\nu - \frac{k}{\Delta x}) * E_L(\nu) && (5.14.3)\\
&= \quad \sum_{n=-\infty}^{\infty} \delta(\nu - \frac{k}{\Delta x}) * 2Lsinc(2\pi\nu\nu L) * E(\nu) && (5.14.4)\\
&= \quad \sum_{n=-\infty}^{\infty} 2Lsinc[2\pi\delta(\nu - \frac{k}{\Delta x})L] * E(\nu) && (5.14.5)\\
&= \quad W_L^{\Delta x} * E(\nu) && (5.14.6)
\end{aligned}$$

where

$$W_L^{\Delta x} \quad = \quad \sum_{n=-\infty}^{\infty} 2Lsinc[2\pi\delta(\nu - \frac{k}{\Delta x})L] \tag{5.14.7}$$

is the instrumental profile due to the truncation of the interferogram and the discrete sampling.

Let the true continuous spectrum is limited to a band $(-\nu_{max}, \nu_{max})$. If the sampling period is short, then the spectral band is not wider than the period of the computed spectrum caused by discrete sampling, that is, $2\nu_{max} \leq \frac{1}{\Delta x}$. In this case, the computed

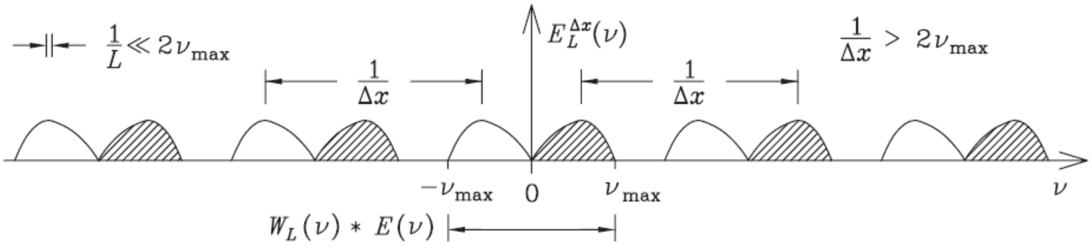

Figure 5.15: The spectrum $E_L^{\Delta x}(\nu), if \frac{1}{\Delta x} > 2\nu_{max}$

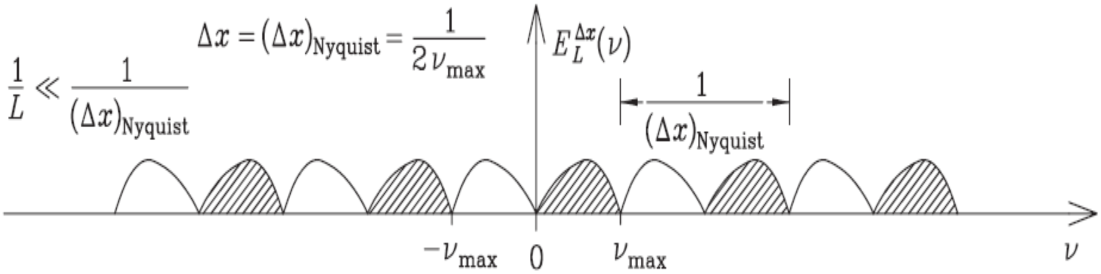

Figure 5.16: The spectrum $E_L^{\Delta x}(\nu)$ when the critical sampling interval$\Delta x = (\Delta x)_{Nyquist} = \frac{1}{2\nu_{max}}$

spectrum $E_L^{\Delta x}(\nu)$ consists of periodically recurring functions as shown in Fig.5.15. The critical sampling interval of an interferometric signal is the inverse of the Nyquist frequency

$$(\Delta x)_{Nyquist} = \frac{1}{2\nu_{max}} \tag{5.14.8}$$

If the sampling interval is smaller than this critical interval, then the spectral orders of the sampled signal do not overlap, and the spectrum is of the type shown in Fig.5.15, where the repeating functions $W_L(\nu) * E(\nu)$ are clearly distinct. The spectrum $E_L^{\Delta x}(\nu)$ of a signal which is sampled at exactly the critical sampling interval is shown in Fig.5.16. In this case, the period of the spectrum $E_L^{\Delta x}(\nu)$ is exactly equal to the bandwidth $2\nu_{max}$ of the true spectrum [18]. If the sampling interval is larger, that is, $\Delta x > \frac{1}{2\nu_{max}}$, then the spectrum $E_L^{\Delta x}(\nu)$is distorted due to aliasing, because the different spectral orders overlap

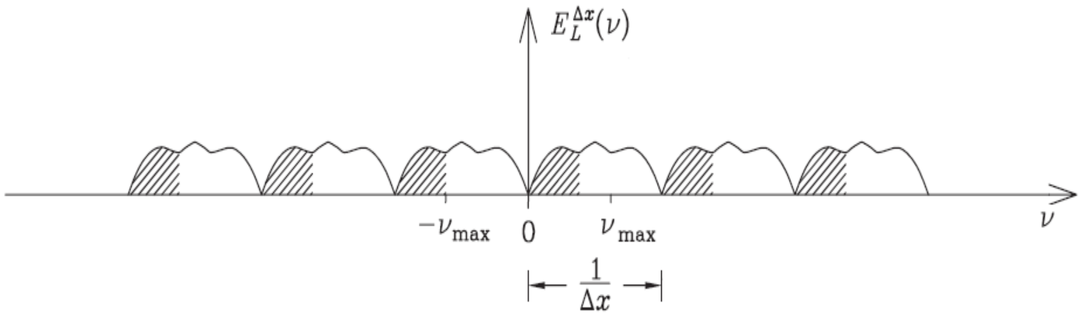

Figure 5.17: The spectrum $E_L^{\Delta x}(\nu)$ which is distorted by aliasing because the sampling interval is larger than the critical sampling interval

Figure 5.18: Measurement site and FTIR spectrometer.

as shown in Fig.5.17.

5.15 Measurement Site

The instrument is located in AAU, inside the science faculty, around Geophysical Observatory. The coordinate of the site is: 9.01 N, 38.76E . The site is at an altitude of 2443m above sea level according to the bench mark of the Observatory and use of GPS. The average pressure and temperature of the site as calculated by GODDARD are $\sim$ 760 hpa and $\sim$ 290 k, respectively[19].

Chapter 6

Radiative Transfer

6.1 Beer's Law and Optical Depth

Let us consider the fate of a beam of radiation passing through an arbitrarily thin layer of the atmosphere along a specific path, as depicted in Fig.6.2. For each kind of gas molecule and particle that the beam encounters, its monochromatic intensity is decreased. Consider the propagation of radiation of wavelength λ through a layer of thickness ds. The radiation traversing the medium will be weakened by its interaction with matter. If the intensity of radiation I_λ becomes $I_\lambda + dI_\lambda$ after traversing the thickness ds in the direction of its propagation, then

$$dI_\lambda = -k_\lambda \rho r I_\lambda ds \tag{6.1.1}$$

where ρ is the density of the air, r is the mass of the absorbing gas per unit mass of air and k_λ denotes the mass extinction cross section (in units of area per mass) for radiation of wavelength λ. The contributions of the various species of gases and particles are additive, as are the contributions of scattering and absorption to the extinction of the incident beam of radiation, i.e,

$$k_\lambda(extinction) = k_\lambda(scattering) + k_\lambda(absorption) \tag{6.1.2}$$

Let us integrate Eq(6.1.1) from the top of the atmosphere (z=∞) down to any level to determine what fraction of the incident beam or pencil of radiation has been attenuated due to absorption and/or scattering and how much remains undepleted. Using Fig.2.1b ds=secθdz. Thus,

$$\ln I_\lambda(\infty) - \ln I_\lambda(z) = sec\theta \int_z^\infty k_\lambda \rho dz \tag{6.1.3}$$

Taking the antilog of both sides we obtain

$$\ln I_\lambda(z) = \ln I_\lambda(\infty) e^{-\tau_\lambda sec\theta} \tag{6.1.4}$$

where

$$\tau_\lambda = \int_z^\infty k_\lambda \rho dz \tag{6.1.5}$$

This set of relationships and definitions, collectively referred to here as Beers law, or also known as Bouguers law, and Lamberts law, which states that the monochromatic intensity, I_λ decreases monotonically with path length as the radiation passes through the layer. The dimensionless quantity τ_λ referred to as the *normal optical depth* or *optical thickness* , which is a sum of the optical depth due to absorption and that due to scattering.

The transmissivity T_λ of the layer is $\frac{I_\lambda(z)}{I_\lambda(\infty)}$. And thus using Eq(6.1.4), transmitance is given by

$$T_\lambda = e^{-\tau_\lambda sec\theta} \tag{6.1.6}$$

It follows that, in the absence of scattering, the monochromatic absorptivity

$$A_\lambda = 1 - T_\lambda = 1 - e^{-\tau_\lambda sec\theta} \tag{6.1.7}$$

Assuming that the medium is homogeneous, so that k_λ is independent of the distance s, and defining the path length

$$u = \int_{z_B}^{z^T} \rho ds \tag{6.1.8}$$

where z_B and z^T are the heights of the bottom and top of the layer, Eq(6.1.6) can be expressed by

$$T_\lambda = e^{-\tau_\lambda} = e^{-k_\lambda u} \tag{6.1.9}$$

where

$$\tau_\lambda = k_\lambda u \tag{6.1.10}$$

is the slant path optical thickness and

$$A_\lambda = 1 - T_\lambda = 1 - e^{-k_\lambda u} \tag{6.1.11}$$

For overhead parallel beam radiation incident on an isothermal atmosphere in which the r, the mixing ratio of the absorbing gas, and k_λ, the volume absorption coefficient, are both independent of height. Thus, from Eq(6.1.1)

$$\frac{dI}{dz} = I_\lambda(\infty) T_\lambda k_\lambda r \rho \tag{6.1.12}$$

For isothermal layer, the density of air molecules varies with altitude as:

$$\rho = \rho_\circ e^{-z/H} \tag{6.1.13}$$

where $\rho_\circ$ is the density of air at see level. If we take the mean surface temperature as 288 K, then $\rho_\circ = 1.25 kgm^{-3}$. If we take the approximate mean value for the temperature of the troposphere and stratosphere, the scale height H for air in the atmosphere is found to be about 7.5 km. Substituting for T_λ and ρ into Eq.(6.1.12), we obtain

$$\frac{dI}{dz} = I_\lambda(\infty)(k_\lambda r \rho_\circ) e^{-z/H} e^{-\tau_\lambda} \tag{6.1.14}$$

From Eq(6.1.10), we obtain

$$\begin{aligned} \tau_\lambda &= (k_\lambda r \rho_\circ) \int_z^\infty e^{-z/H} dz && (6.1.15) \\ &= H(k_\lambda r \rho_\circ) e^{-z/H} && (6.1.16) \end{aligned}$$

Hence using this expression and Eq(6.1.14), we get

$$\frac{dI_\lambda}{dz} = \frac{I_\lambda(\infty)}{H} \tau_\lambda e^{-\tau_\lambda} \tag{6.1.17}$$

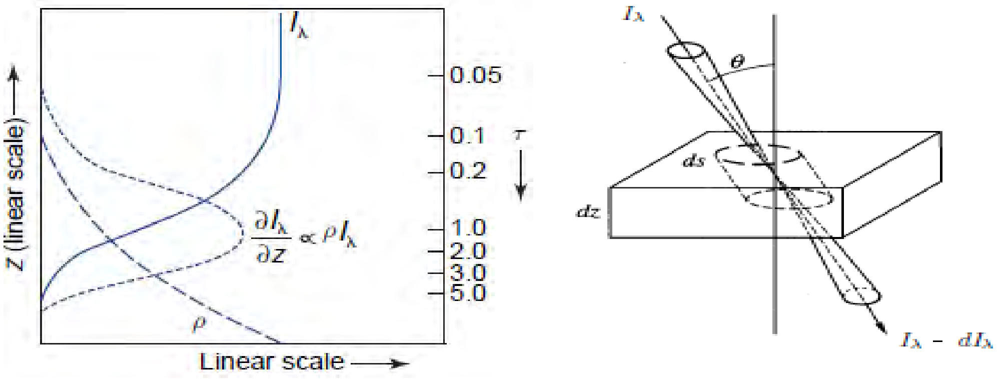

Figure 6.1: Left: vertical profiles of the monochromatic intensity of incident radiation, the rate of absorption of incident radiation per unit height, air density and optical depth, for k_λ and r independent of height. Right: extinction of incident parallel beam solar radiation as it passes through an infinitesimally thin atmospheric layer containing absorbing gases and/or aerosols.

Taking the second derivative of Eq(6.1.17) will give us

$$\frac{d}{dz}\frac{dI_\lambda}{dz} = \frac{I_\lambda(\infty)}{H} e^{-\tau_\lambda} \frac{d\tau_\lambda}{dz}(1-\tau_\lambda) \tag{6.1.18}$$

Now at the level where the absorption is strongest,

$$e^{-\tau_\lambda} \frac{d\tau_\lambda}{dz}(1-\tau_\lambda) = 0 \tag{6.1.19}$$

from which it follows that τ_λ=1. Hence, $\frac{dI_\lambda}{dz}$ decrease most rapidly around the level where $\tau_\lambda = 1$ commonly referred to as the level of unit optical depth(see Fig.2.1a). Well above the level of unit optical depth, the incoming beam is virtually undepleted, but the density is so low that there are too few molecules to produce appreciable amounts of absorption per unit path length. Well below the level of unit optical depth, there is no shortage of molecules, but there is very little radiation left to absorb. The larger the value of the absorption coefficient k_λ and the larger the secant of the zenith angle, the smaller the density required to produce significant amounts of absorption and the higher the level of unit optical depth. For small values of k_λ, the radiation may reach the bottom of the atmosphere long before it reaches the level of unit optical depth. For overhead parallel beam radiation incident upon an optically thick atmosphere, 80% of the energy

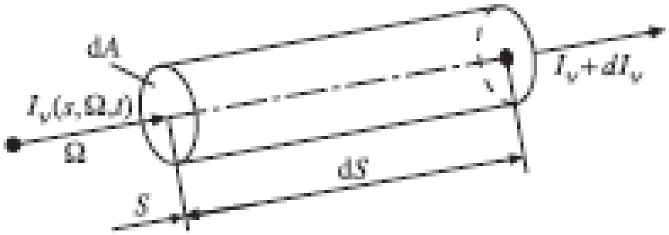

Figure 6.2: Schematic representation of the geometery of radiative transfer by a volume element

is absorbed at levels between τ_λ=0.2 and τ_λ=4.0 which corresponds to a geometric depth of three scale heights. The level of slant path unit optical depth is strongly dependent on the solar zenith angle. When the sun is exactly overhead, $\theta = 0°$; at the horizon $\theta = 90°$. As θ increases, the pathlength of the solar beam through the atmosphere increases. The optical depth of the atmosphere increases as the pathlength increases since the solar beam transects a longer section of the atmosphere, and there is proportionately more opportunity for extinction to occur [15].

6.2 The Radiative Rransfer Equation

Consider the emitting, absorbing and scattering medium characterized by the spectral absorption coefficient $k_\nu(\mathbf{r})$ and spectral scattering coefficient $\sigma_\nu(\mathbf{r})$. The beam of monochromatic radiation with intensity $I_\nu(\mathbf{r},\Omega)$ propagates in this medium in the observation direction Ω along the path s. We choose the elementary volume in the form of a cylinder with cross section dA, length ds, disposed in the vicinity of coordinate s, the axis of a cylinder coinciding with the direction of s (Fig.2.2). Let $I_\nu(s,\Omega)$ be the radiation intensity at point s, and $I_\nu(s,\Omega) + dI_\nu$ be the radiation intensity at point s+ds, and dI_ν be the variation (positive or negative) of the intensity flux when it passes the path ds. Thus, the radiant energy dE crossing the dA in time dt in the solid angle $d\Omega$ in the frequency range

$[\nu, \nu + d\nu]$ is

$$dE_\nu = I_\nu(s, \Omega) dA d\Omega d\nu dt \tag{6.2.1}$$

In addition, the increase of the energy of radiation in the cylinderical volume dAds propagating within the limits of the solid angle $d\Omega$ with respect to the direction **Omega** for the time interval dt within the frequency band $d\nu$ is

$$dE_\nu = W_\nu dAds s\Omega d\nu dt \tag{6.2.2}$$

where W_ν is the increment of the beam of energy in the volume.
Equating 6.2.1 and 6.2.2, we obtain

$$\frac{dI_\nu(s, \Omega)}{ds} \;=\; W_\nu \tag{6.2.3}$$

For an absorbing, emitting and scattering medium the quantity W_ν is formed by the components caused by increments and losses of radiation energy. Thus, from[] W_ν becomes

$$W_\nu = \gamma_\nu(s) I_{\nu B}[T(s)] - [\gamma_\nu(s) + \sigma_\nu(s)] I_\nu(s, \Omega) + \frac{1}{4\pi}\sigma(s) \int\int_{\Omega'} T_\nu(s, \Omega') p_\nu(\Omega' \to \Omega) d\Omega' \tag{6.2.4}$$

Thus, the basic radiative transfer equation becomes:

$$\frac{dI_\nu(s, \Omega)}{ds} + [\gamma_\nu(s) + \sigma_\nu(s)] = \gamma_\nu(s) I_{\nu B}[T(s)] + I_\nu(s, \Omega) + \frac{1}{4\pi}\sigma(s) \int\int_{\Omega'} T_\nu(s, \Omega') p_\nu(\Omega' \to \Omega) d\Omega' \tag{6.2.5}$$

Writing this equation in compact form gives

$$\frac{1}{\beta_\nu(s)} \frac{dI_\nu(s, \Omega)}{ds} + I_\nu(s, \Omega) = S_\nu(s) \tag{6.2.6}$$

where, $S_\nu(s)$, is the source function, $\beta_\nu(s)$, is the spectral extinction coefficient and they are given by

$$S_\nu(s) = (1 - \omega_\nu) I_{\nu B}[T(s)] + \frac{1}{4\pi}\omega \int\int_{\Omega'} T_\nu(s, \Omega') p_\nu(\Omega' \to \Omega) d\Omega' \tag{6.2.7}$$

where, ω_ν, is the spectral albedo and given by

$$\omega_\nu = \frac{\sigma_\nu(s)}{\gamma_\nu(s) + \sigma_\nu(s)} \tag{6.2.8}$$

and

$$\beta_\nu(s) = \gamma_\nu(s) + \sigma_\nu(s) \tag{6.2.9}$$

The remainder of this section is concerned with the absorption and emission of infrared radiation in the absence of scattering. This simplified treatment is justified by the fact that the wavelength of infrared radiation is very long in comparison to the circumference of the air molecules so the scattering efficiency is negligible. For absorbing and emitting medium, $\omega_\nu(s) = 0$ since $\sigma_\nu(s) = 0$. Thus, the radiative transfer equation for such media takes the form []:

$$\frac{1}{\beta_\nu}\frac{dI_\nu(s,\Omega)}{ds} + I_\nu(s,\Omega) = I_{\nu B}[T(s)] \tag{6.2.10}$$

6.3 Radiative Transfer Equation for Plane-Parallel Atmospheres

Many atmospheric radiative transfer calculations can be simplified through use of the plane-parallel approximation in which temperature and the densities of the various atmospheric constituents are assumed to be functions of height (or pressure) only. In this case, it is convenient to measure linear distances normal to the plane of stratification (see Fig.6.3a). If z denotes this distance, then the general equation of radiative transfer defined in Eq(6.2.10) becomes:

$$cos\theta\frac{dI(z;\theta,\phi)}{k\rho dz} = -I(z;\theta,\phi) + J(z;\theta,\phi), \tag{6.3.1}$$

where θ denotes the inclination to the upward normal, and ϕ the azimuthal angle in reference to the x axis. Introducing the normal optical thickness

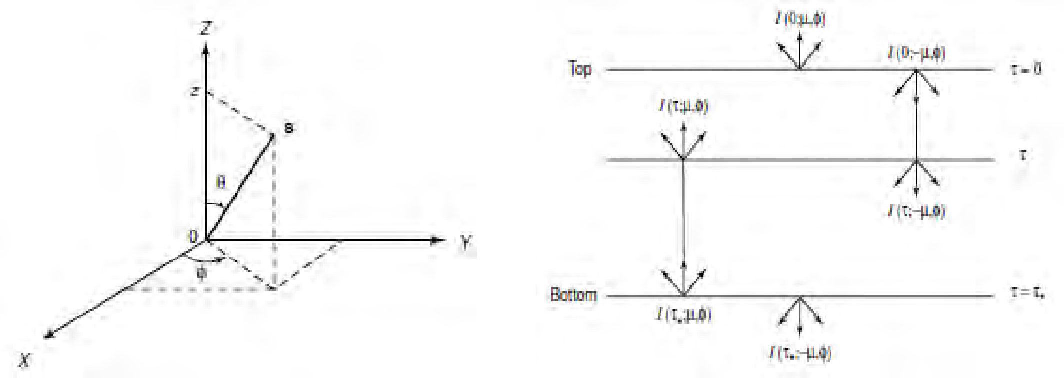

Figure 6.3: Left: geometry for plane-parallel atmospheres where and denote the zenith and azimuthal angles, respectively, and s represents the position vector. Right: upward(μ) and downward ($-\mu$)intensities at a given level τ and at top ($\tau = 0$) and bottom($\tau = \tau_*$) levels in a finite, plane-parallel

$$\tau = \int_z^{\infty} k\rho dz \tag{6.3.2}$$

$$d\tau = k\rho dz \tag{6.3.3}$$

Substituting 6.3.3 into 6.3.1 we obtain

$$u\frac{dI(\tau;\theta,\phi)}{d\tau} = -I(\tau;\theta,\phi) + J(\tau;\theta,\phi) \tag{6.3.4}$$

This is the differential form of the radiative transfer equation in a plane parallel atmosphere and is valid for all angles. We can decouple this equation into its constituents (upwelling and downwelling) by taking the boundary conditions into consideration. In addition, we distinguish two cases when transfer problems in plane-parallel atmospheres are considered: (i) the finite atmosphere which is bounded on two sides at $\tau = 0$ and at $\tau = \tau_*$ (say), see Fig.6.3b; and (ii) the semi-infinite atmosphere which is bounded on two side ($\tau = 0$) and extends to infinity in the direction $\tau \dashrightarrow \infty$.

We know that at the top of the atmosphere, sunlight is the only incident intensity from the hemisphere containing the sun. At the surface, we have constraint on the upwelling intensity due to thermal emission or the surface reflectivity. To obtain the upward intensity ($\mu > 0$) at level τ for the atmosphere with a finite optical thickness, multiply

Eq(6.3.4) by a factor of $e^{-\tau/\mu}$ and perform integration from τ to $\tau = \tau_*$. This leads to

$$I(\tau; \mu, \phi) = I(\tau_*; \mu, \phi) e^{-(\tau_* - \tau)/\mu} + \int_{\tau}^{\tau_*} J(\tau'; \mu, \phi) e^{-(\tau' - \tau)/\mu} \frac{d\tau'}{\mu} (1 \geq \mu > 0) \qquad (6.3.5)$$

The downwelling radiation component has $\mu < 0$. Thus, multiplying Eq(6.3.4) by $e^{\tau/\mu}$, replacing μ by $-\mu$ and integrating from $\tau = 0$ to τ, we obtain

$$I(\tau; -\mu, \phi) = I(0; -\mu, \phi) e^{-\tau/\mu} + \int_{0}^{\tau} J(\tau'; -\mu, \phi) e^{-(\tau - \tau')/\mu} \frac{d\tau'}{\mu} (-1 \geq \mu > 0) \qquad (6.3.6)$$

In particular for the emergent intensities we have

$$I(0; \mu, \phi) \;\; = \;\; I(\tau_*; \mu, \phi) e^{-\tau_*/\mu} + \int_{0}^{\tau_*} J(\tau'; \mu, \phi) e^{-\tau'/\mu} \frac{d\tau'}{\mu} \qquad (6.3.7)$$

and

$$I(\tau_*; -\mu, \phi) = I(0; -\mu, \phi) e^{-\tau_*/\mu} + \int_{0}^{\tau_*} J(\tau'; -\mu, \phi) e^{-(\tau_* - \tau')/\mu} \frac{d\tau'}{\mu} \qquad (6.3.8)$$

In the case of a semi-infinite atmosphere the foregoing equations reduce to [21]:

$$I(\tau; \mu, \phi) = \int_{\tau}^{\infty} J(\tau'; \mu, \phi) e^{-(\tau' - \tau)/\mu} \frac{d\tau'}{\mu} \qquad (6.3.9)$$

$$I(\tau; -\mu, \phi) = I(0; -\mu, \phi) e^{-\tau/\mu} + \int_{0}^{\tau} J(\tau'; -\mu, \phi) e^{-(\tau - \tau')/\mu} \frac{d\tau'}{\mu} \qquad (6.3.10)$$

$$I(\tau_*; -\mu, \phi) = \int_{0}^{\infty} J(\tau'; \mu, \phi) e^{-\tau'/\mu} \frac{d\tau'}{\mu}. \qquad (6.3.11)$$

Chapter 7

Retrieval theory

7.1 Inverse Method

For a discretized atmosphere, the analytical relationship between the measured radiance and the true atmospheric state, the forward radiative transfer equation, is given by:

$$\mathbf{y} = \mathbf{F}(x; \mathbf{b}) + \epsilon \tag{7.1.1}$$

where $\mathbf{F}$ represents the radiative transfer function, $\mathbf{y}$ is the measurement vector which contains the recorded radiances, $\mathbf{x}$ represents the state vector (i.e. the atmospheric parameters we want to retrieve, which is the carbon monoxide profile in our case), $\mathbf{b}$ are the other parameters which have an influence on the measurement (temperature and pressure profiles, instrumental properties, etc.) and ϵ is the measurement noise.

The retrieval of the vertical distribution of an atmospheric parameter from remote sensing measurements is generally performed by fitting forward model simulations to the available observations []. The fitting procedure consists in the minimization of a cost function, generally made of the summation of two terms. The first term is the chi-square that measures how the forward model calculated in $\mathbf{x}$ is able to reproduce the measurements within the errors and the second term constrains the retrieved profile to follow some feature of $\mathbf{x}_a$. This term can be used for example to penalize solutions that either oscillate beyond acceptable limits or deviate from an a-priori. The Tikhonov regularized solution of the retrieval problem can be obtained by minimizing the following cost function[25]:

$$f(\mathbf{x}) = (\mathbf{y} - \mathbf{F}(\mathbf{x}))^T \mathbf{S}_y^{-1} (\mathbf{y} - \mathbf{F}(\mathbf{x})) + \gamma(\mathbf{x} - \mathbf{x}_a)^T \mathbf{R}(\mathbf{x} - \mathbf{x}_a) \tag{7.1.2}$$

where $\mathbf{S}_y$ variance-covariance matrix (VCM) of $\mathbf{y}$, γ is a positive parameter characterizing the strength of the regularization, $\mathbf{x}_a$ an a priori state and $\mathbf{R}$ is a regularization matrix which is given by:

$$\mathbf{R} = \mathbf{B}_1^T \mathbf{B}_1$$

where $\mathbf{B}$ is a first order finite differences operator which is given by

$$\mathbf{B} = \begin{pmatrix} -1 & 1 & 0 & ... & 0 & 0 \\ 0 & -1 & 1 & ... & 0 & 0 \\ & & . & & & \\ & & & . & & \\ & & & & . & \\ 0 & 0 & 0 & ... & -1 & 1 \end{pmatrix},$$

In case of weak non-linearity of the forward model, the Gauss-Newton technique can be successfully applied (Press et al., 1992). Thus, the minimum of f(x) may be searched iteratively using the Gauss-Newton method, which provides the following expression of x at each iteration[25]:

$$\mathbf{X} = (\mathbf{S}_{\hat{X}}^{-1} + \gamma \mathbf{R})^{-1} (\mathbf{S}_{\hat{X}}^{-1} \hat{\mathbf{X}} + \gamma \mathbf{R} \mathbf{X}_a) \tag{7.1.3}$$

where $\hat{x}$ is the non-regularized state vector obtained when only the first term of f(x) is minimized and it is given by

$$\hat{\mathbf{X}} = \hat{\mathbf{X}}_\circ + (\mathbf{K}^T \mathbf{S}_y^{-1} \mathbf{K})^{-1} \mathbf{K}^T \mathbf{S}_{\mathbf{y}}^{-1} (\mathbf{y} - \mathbf{F}(\hat{\mathbf{X}}_\circ)) \tag{7.1.4}$$

with $\hat{\mathbf{X}}_\circ$ being the initial guess of the iteration and $\mathbf{K}$ is the Jacobian matrix of $\mathbf{F}(x)$ calculated in $\hat{\mathbf{X}}_\circ$, $K = \frac{\partial \mathbf{F}}{\partial \mathbf{X}}$. And $\mathbf{S}_{\hat{\mathbf{X}}}$ is its VCM which is given by

$$\mathbf{S}_{\hat{\mathbf{X}}} = (\mathbf{K}^T \mathbf{S}_y^{-1} \mathbf{K})^{-1} \tag{7.1.5}$$

Using the above equations we arrive at the retrieval equation which is used in the PROFFIT software [26]:

$$x_{i+1} = [k_i^T k_i + \sigma^2 \sum \gamma_i B_i^T B_i]^{-1} [k_i^T (\Delta y_i + k_i x_i) + \sigma^2 \sum \gamma_i B_i^T B_i x_a] \tag{7.1.6}$$

We used the inversion code PROFFIT for the retrieval of trace gas profile. It allows to choose between two regularization methods: the optimal estimation method and the Tikhonov-Phillips method. We used the later one because it allows to perform the whole inversion procedure on a logarithmic scale. This avoids negative VMR values. PROFFIT also allows a simple scaling of a given profile (climatological profile), which is often done for interfering gas.

7.2 Spectral Line Fit

To deduce the correct information from the measurement it is important to know the accurate ILS. In ground-based atmospheric sounding for which high-resolution spectrometers are used, the mixing ratio profile of a trace gas can be retrieved from the observed line shape because of the height-dependent pressure broadening. If the actual ILS is left undetermined and simply assumed to be perfect, a substantial systematic error might be introduced. Therefore an independent measurement of the ILS is needed.

In the preceding chapter we have seen that an idealized FTIR spectrometer with finite circular FOV shows a sinc-shaped ILS which leads to modulation loss and a linear phase shift which leads to a somewhat reduced modulation frequency along the interferogram. The ILS of a real FTIR-spectrometer is equivalent to a complex modulation efficiency in interferogram domain, which allows for variation in amplitude and phase orientation of the measured cosine-like modulation with respect to the pure cosine response of the ideal interferometer for monochromatic input along OPD.

We used the software called LINEFIT which allows us to deduce the ILS from low-pressure gas cell measurements. The software uses appropriate regularizing constraints to achieve an optimal ILS reconstruction in the interferogram domain. A detailed description is given in [27]. The cell measurement was made using HBr cell. The radiation source (globar) was at $1000°C$. The beam was focused on the cell which was placed near the focal point of the parabolic mirror which focuses the beam toward the aperture. In addition to the spectrum with HBr cell, measurement was also made without the cell but with the same source. These two measurements were ratiod together and given as an input for LINEFIT with the corresponding microwindows of HBr.

7.3 HITRAN Database

The HITRAN (HIgh resolution TRANsmistion) database provides the parameter required to compute absorption coefficient for all atmospheric constituents of interest.
A simplified form of line strength from[15] is

$$S_i(T) = S_{i,\circ}(T_\circ)(\frac{T_\circ}{T})^m \exp[\frac{E_i^{''}}{k}(\frac{1}{T_\circ} - \frac{1}{T})] \tag{7.3.1}$$

where m is is an empirical parameter of order unity and $E_i^{''}$ represents the energy of the lower state of each transition.

HITRAN provides two half widths, the self-broadened half width ($\alpha_{s,\circ}$) and air-broadened or foreign-broadened half width ($\alpha_{s,\circ}$) at the reference temperature and pressure. Thus the pressure-broadened half width of transitions of radiatively active species A at arbitrary pressure and temperature scales as[15]

$$\alpha_p(p,T) = (\frac{T_\circ}{T})^n(\frac{p-p_A}{p_\circ}\alpha_{f,\circ} + \frac{p_A}{p_\circ}\alpha_{s,\circ}) \tag{7.3.2}$$

where n is an empirical fitting parameter supplied by HITRAN and p_A is the partial pressure of species A. For minor trace gases, $p_A \ll p$ and $p_A \ll p_\circ$ so $p - p_A \approx p$ and $p_A/p_\circ \approx 0$. For such gases, Eq(7.3.2) simplifies to

$$\alpha(p,T) \approx \alpha_\circ \frac{p}{p_\circ}(\frac{T_\circ}{T})^n \tag{7.3.3}$$

HITRAN also supplies a parameter $\delta(p_\circ)$ to calculate the line center frequency $(\tilde{\nu}_\circ)$ change due to pressure-shifting:

$$\tilde{\nu}^* = \tilde{\nu}_\circ + \delta(p_\circ)\frac{p}{p_\circ} \tag{7.3.4}$$

In this thesis the latest HITRAN database (HITRAN 2008) is used. But the line parameters of CO are kept unchanged and are the same as HITRAN 2004 [25]. This database contains the parameters of all isotopes of CO ($^{12}C^{16}O,^{13}C^{16}O,^{12}C^{18}O,^{12}C^{17}O,^{13}C^{18}O and ^{13}C^{17}O$). The line intensity of $^{12}C^{16}O$ and the exponent n for the dependence of air-broadened half-widths have been updated for all CO transitions [15].

7.4 Microwindow Selection

Microwindows are set of narrow spectral interval (2 cm^{-1} width in our case) that are selected as those that contain the best information on the target parameters and are less affected by systematic error, such as for instance uncertain spectroscopic data, interference of non-target species, NLTE and line mixing effects . On the other hand, a large microwindow can introduce large systematic errors due to instrumental features or errors or omissions in the spectroscopy of interfering lines. Furthermore, reducing the microwindow width reduces uncertainties due to interfering gases. We used automatic line finding

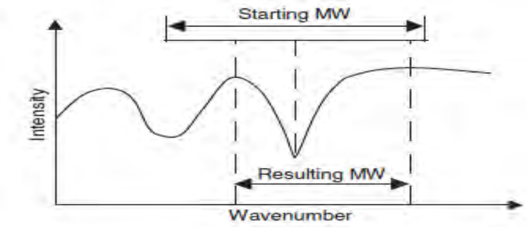

Figure 7.1: Example of a spectrum demonstrating the choice of the microwindow size.

code to find the microwindows. The code allows to vary the width of the microwindow so that we can vary the width to find the optimized size (see Fig.7.1). Detailed description is given in [28]. Therefore the PROFFIT analysis is performed in the microwindow of (2215.5 - 2215.8 cm^{-1}). The most interfering species are found to be H_2O, CO_2, O_3 and N_2O.

7.5 Error Analysis

Assuming a linearization of the forward and inverse model about some reference state and spectrum, respectively - the difference between the retrieved and the real state of the atmosphere can be written as

$$\begin{aligned}\hat{x} - x = (A - I)(x - x_a) & \text{........... smoothing} \\ + A_e(e - e_a) & \text{....................interference} \\ + G_y k_b(b - \hat{b}) & \text{..................model parameter} \\ + G_y \varepsilon & \text{..............................retrieval error}\end{aligned}$$

where G_y is retrieval gain matrix showing the sensitivity of the retrieval to the measurement, $k_b = \frac{\partial F}{\partial b}$ is the sensitivity of the forward model to non-retrieved parameter[28].

7.5.1 Smoothing Error

The VMR profile retrieved using PROFFIT incorporates atmospheric information from both our spectroscopic measurements and an a priori profile. Accordingly, uncertainty in the a priori profile in a discretized layering scheme will contribute to the uncertainty in the retrieved profile and, depending on the exact a priori profile used in the retrieval, the resulting error is called smoothing error, S_s, which tends to have both systematic and random components. The smoothing error quantifies how strongly fine structures of the true atmospheric state are smoothed by the observing system due to the limited altitude resolution captured in the measurement. The smoothing error covariance, S_s, is computed as

$$S_s = (I - A)S_a(I - A)^T \tag{7.5.1}$$

7.5.2 Spectral Noise

To correctly account for the influence of spectral noise on the retrieval it is prudent to consider the statistical impacts of the algorithms used to compute spectra from the recorded interferograms. These algorithms can introduce off-diagonal elements into the large measurement noise covariance matrix, S_ϵ, and therefore introduce computational difficulties into the retrieval. So, S_ϵ, is taken to be diagonal with elements defined as the square of the reciprocal of the SNR. Thus, the covariance of the retrieval noise is

$$S_m = G_y S_\epsilon G_y^T \tag{7.5.2}$$

7.5.3 Interference (Interfering Species Error)

The error on the retrieval of a target gas coming from the uncertainties in the vertical distribution of the interfering species has been calculated by performing retrievals using an ensemble of vertical profiles of every significant interferer separately, representing the uncertainties in its a priori profile. Consequently, we drive an error covariance matrix, S_e, based on the obtained set of retrieved target profile difference relative to the reference profile, which represents the contribution of the interfering species uncertainties to the random error. Thus,

$$S_e = A_{xe} S_{ea} A_{xe}^T \tag{7.5.3}$$

7.5.4 Viewing Geometry

This is the uncertainty associated with the solar zenith angle (SZA). Since the sun tracker mirror could not track the sun exactly, the field of view of the instrument could be offset from the center of the sun by up to 0.25^o (the radius of the solar disc is 0.25°)[30].

7.5.5 Atmospheric Temperature

The source of temperature data is from GODDARD automailer system. Temperature measurements were performed for 12 UT, while the FTIR measurements are conducted at any time during daylight. This introduces another source of uncertainty. Since molecular line parameters are temperature dependent, our retrieval is influenced in the temperature profile. The temperature dependence of the line strength yields interactivities in the retrieved zenith column amount (ZCA).

7.5.6 Line Parameter Error

Spectroscopic line parameter and uncertainities were taken from HITRAN 2008 database. Accordingly, it is reported that the root mean square error of CO is about 1.3%[1].

Chapter 8

RESULTS AND DISCUSSION

8.1 Characterization of Measurement and Retrieval Error

We categorized the errors into: systematic error and statistical error. As seen in Fig.8.1, the errors in CO VMR vary as a function of altitude. The estimated error values for some layers are summarized in Table 8.1 and Table 8.2. Systematic error is found to be greater than the random error for each layers. Most of the systematic error has come from the spectroscopic uncertainty and the lowest error is from the LOS. The total column is

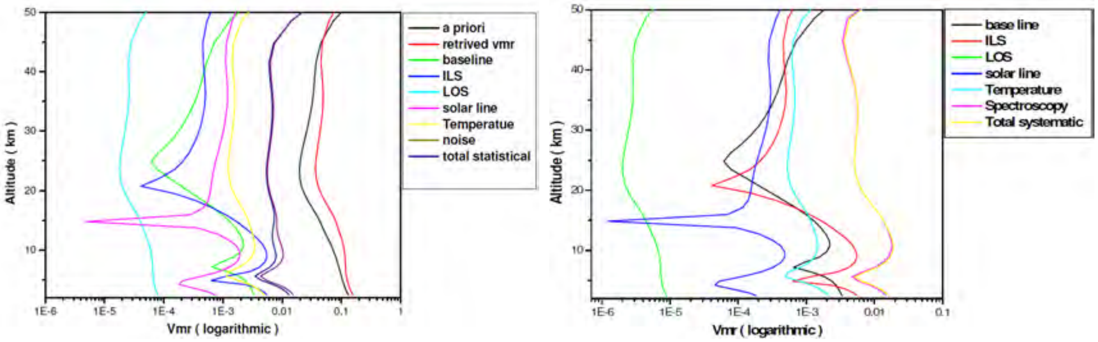

Figure 8.1: Left: altitude variation of statistical error and right: systematic error

Altitude (km)	Baseline error	ILS distortion	LOS error	Solar line intensity error	Temperature error	Spectroscopy	Total systematic error
2.45 - 2.94	1.07	1.24	0.008	0.02	0.51	7.08	7.28
2.94 - 3.56	1.08	1.02	0.008	0.003	0.47	6.85	7.02
3.56 - 4.21	1.05	0.63	0.008	0.006	0.40	6.31	6.44
4.21 - 4.90	0.95	0.06	0.008	0.004	0.32	5.48	5.57

Table 8.1: Systematic error budget for the retrieval of CO VMR profile (%).

Altitude (km)	Baseline error	ILS distortion	LOS error	Solar line intensity error	Temperature error	Noise	Total statistical error
2.45 - 2.94	1.07	1.25	0.07	0.06	1.18	4.65	5.07
2.94 - 3.56	1.08	1.02	0.07	0.01	1.08	4.29	4.67
3.56 - 4.21	1.05	0.63	0.07	0.02	0.93	3.67	3.98
4.21 - 4.90	0.95	0.06	0.07	0.02	0.76	2.83	3.08

Table 8.2: Statistical error budget for the retrieval of CO VMR profile (%).

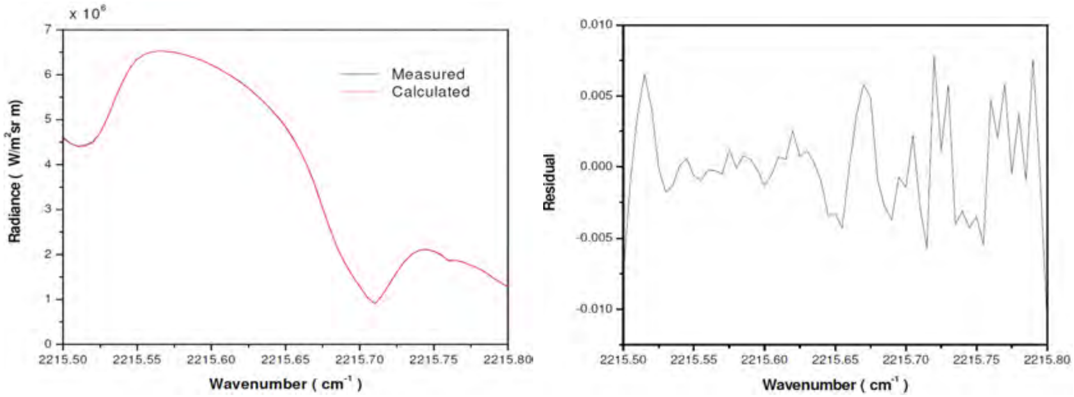

Figure 8.2: Left: spectral radiance in the micro window of 2215.5 - 2215.8 cm^{-1} of the spectrum 100127. Right: spectral fit residuals from the microwindow of 2215.5 - 2215.8 cm^{-1} for a spectra recorded on January 27, 2010 with SZA of 31^o.

characterized by systematic error of 2.7%. Ranking the source of statistical error, measurement noise has shown the largest error and the lowest is due to LOS error. Statistical error of the total column is 5.0%.

HBr gas cell is used to check for the well being of the instrument. Using the globar as a source of IR radiation, up to 100 scans are coadded to get spectra of both with and without the presence of HBr cell. The HBr spectra is ratioed with the background to find the absorptance of HBr. LINEFIT software uses this result as an input to calculate modulation efficiency and phase error. Accordingly, the modulation efficiency is found to be nearly unity during the measurement period. The phase error is between 0.01 and -0.04 rad during the measurement period. Moreover, the residual in the spectral fit is well below 1% and comparable to values of other gases reported by Mathhias Schneider[30]. Hence all the results indicate that the misalignment is not much to cause significant error in our result.

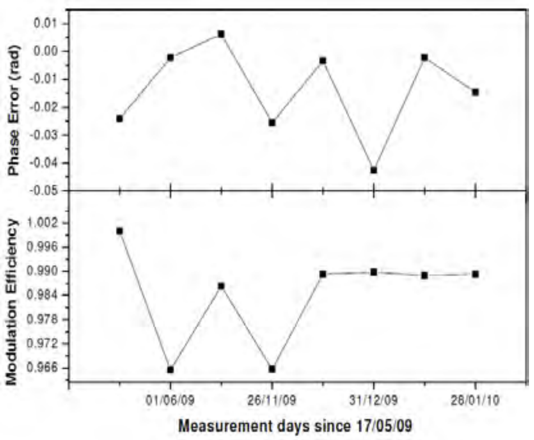

Figure 8.3: Modulation efficiency and phase error.

8.2 Information Content and Vertical Resolution

The rows of the averaging kernel matrix define the vertical resolution of the retrieval (full width at half maximum), the trace of the matrix defines the number of statistically independent elements that can be retrieved, or degrees of freedom for signal (DOFs) and the diagonal elements represent a measure of the sensitivity of the CO retrieval at a given profile grid point to the true CO VMR and thus the peak of each averaging kernel gives the altitude of maximum sensitivity to each layer. The DOFs for the CO retrieval is nearly 3 which means there are about 3 independent pieces of information from the measurement. The averaging kernels shown in Fig.8.4, left have been calculated for micro-window of 2215.5 - 2215.8 cm^{-1}, an OPD of 100 cm, and a SZA of 31° for a retrieval of CO from spectrum taken on 4^{th} of February 2010. It shows that the measurements are more sensitive to lower atmosphere than upper atmosphere reaching a maximum value of 0.2 with a corresponding altitude of $\sim 4km$. And the peak of the averaging kernel in the troposphere decreases with altitude, 0.15 for 2.450 - 4.896 km, 0.13 for 2.450 - 11.700 km, 0.11 for 2.450 - 17.120 km and 0.08 for 2.450 - 24.810 km. Values close to zero (typically < 0.05) indicate that there is no significant sensitivity to the CO abundance at the corresponding altitude. So in terms of sensitivity, mesosphere is more important

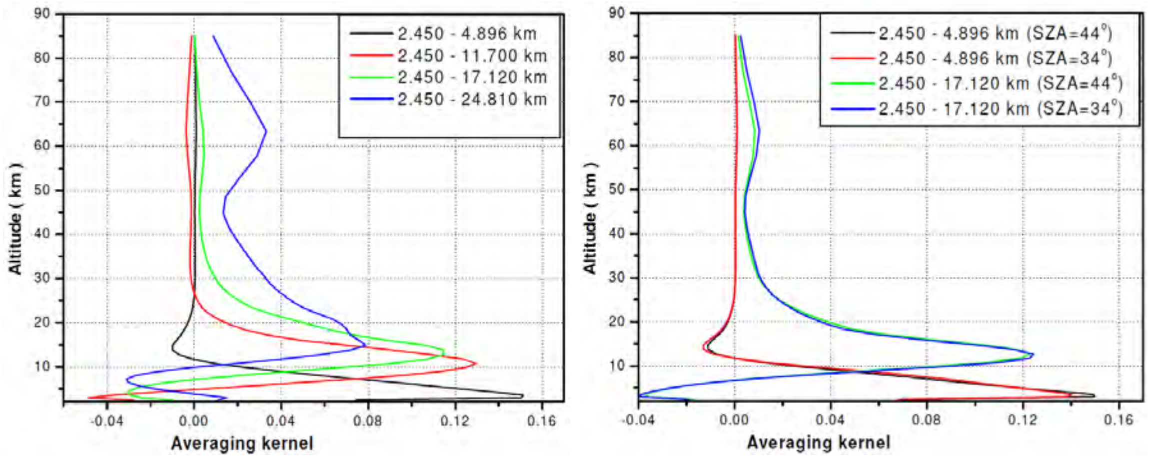

Figure 8.4: Left: averaging kernels for the retrieval of CO for the altitude range 2.450 - 4.896 km, 11.700 km, 2.450 - 17.120 km and 2.450 - 24.810 km . Right: averaging kernels for 2.450 - 4.896 km and 2.450 - 17.120 km CO retrievals for solar zenith angles (SZAs) of 37° and 46°.

than stratosphere. The vertical resolution decreases until $\sim 25km$ with a corresponding altitude of 35 km. Averaging kernels for a SZA of 37° and 46° of February 01, 2010 is given in Fig.8.4, right. It can be seen that the vertical shape of the kernel changes with SZA. In addition, the DOFs is 2.8 for 37° and 2.9 for 46°. So the averaging kernel of a given measurement day is averaged over repeated measurements of that day. The vertical resolution of CO profile ranges from 3 to 9 km in the troposphere and increases to 15 km in the lower stratosphere as shown in Fig.8.5, left. Above 25 km, the vertical resolution increases to 19 km near the stratopause. Upper most mesosphere has shown a resolution of 15 km. Since the measurement shows weak resolution for the mesosphere the next discussion is only dedicated to troposphere and stratosphere.

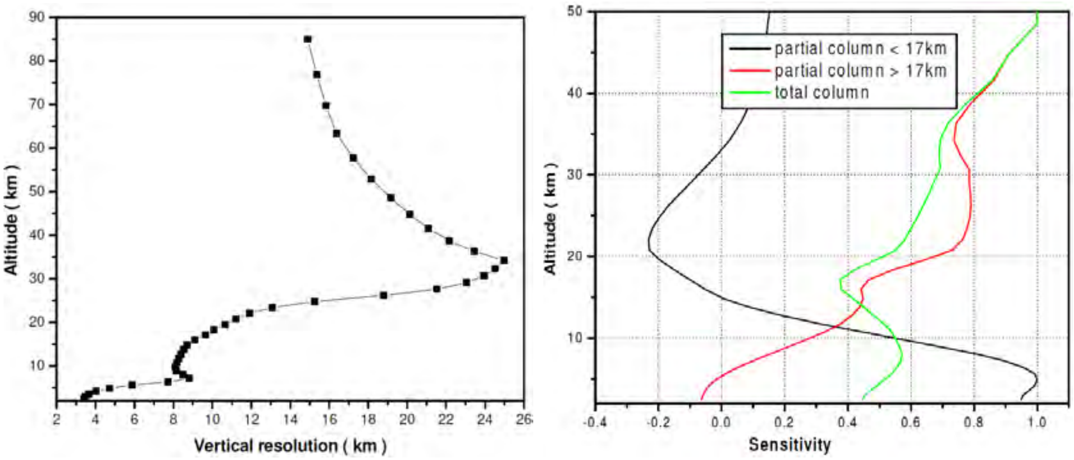

Figure 8.5: Left: the full width at half-maximum of the averaging kernel representing the vertical resolution of the measurement. Right: sensitivity of partial column.

8.3 Seasonal Variation of CO Distribution in the Troposphere

An over all comparison of all data sets is presented in the following figures since the start of the measurement. Monthly averages of tropospheric mixing ratios are also shown in Fig.8.6, left and given in Table 8.3. The topographic map of Ethiopia (not given here) shows the central portion of Ethiopia is mountainous, and Addis Ababa is surrounded by peaks with elevations up to 3300 m. This suggests that pollutants may become trapped in the valley under conditions of atmospheric stagnation. Ethiopia has a monsoonal climate with rainfall distributions that vary with elevation. According to [31], precipitation in Addis Ababa is greatest in August and least in November and December. Based on this seasonality, air pollution is likely worst between October and February. The result in Fig.8.6, left indicated that in the lower most troposphere CO mixing ratios were in the range 127 - 198 ppbv during the measurement. The minimum and maximum mixing ratios were seen in November 2009 and January 2010 respectively. Eventhough there is less significant increase of the mixing ratio in November 2010 and December 2010 between the altitudes 6 km and 8 km, low tropospheric mean in comparison to high boundary layer

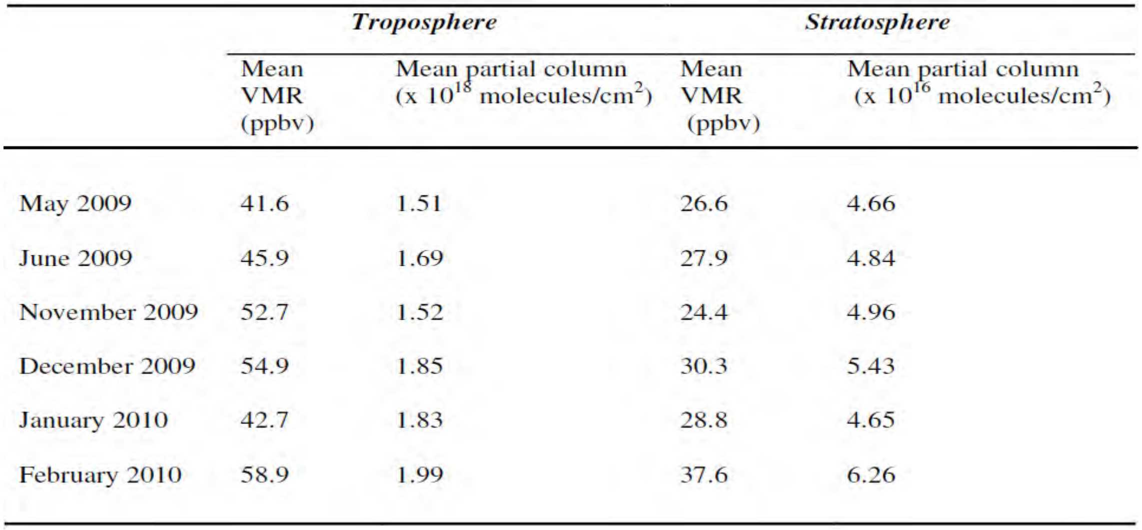

	Troposphere		*Stratosphere*	
	Mean VMR (ppbv)	Mean partial column (x 10^{18} molecules/cm^2)	Mean VMR (ppbv)	Mean partial column (x 10^{16} molecules/cm^2)
May 2009	41.6	1.51	26.6	4.66
June 2009	45.9	1.69	27.9	4.84
November 2009	52.7	1.52	24.4	4.96
December 2009	54.9	1.85	30.3	5.43
January 2010	42.7	1.83	28.8	4.65
February 2010	58.9	1.99	37.6	6.26

Table 8.3: Monthly averages of VMR and partial column of the troposphere and stratosphere

mixing ratios reflects a decrease of CO mixing ratio with height. In January 2010 CO profiles was decreased significantly with a difference of 156 ppbv between the surface and near tropopause. In November 2009, the difference between mixing ratios in the boundary layer and lower troposphere is ∼23 ppbv indicating lowest variability. The VMR of CO is found to have its lowest maximum least when compared to the rest of months. In the middle and upper troposphere (> 6 km), minimum and maximum VMR is measured during May 2009 and February 2010 respectively. The atmosphere is relatively well mixed during January 2010 measurement of the middle atmosphere. Crutzen and Carmichael from [32] stated that biomass burning is believed to be the most important source of CO in the tropics. Intense biomass burning takes place in the sub-saharan Africa (northern hemisphere) between December and February. This result is also confirmed in Fig.8.6, left. Fig.8.6, left shows lower tropospheric CO has its maximum in January 2010. As seen in Fig.8.6, right, a seasonal maximum (179 ppbv) and minimum (42 ppbv) appear in winter and late spring respectively. CO of 52 ± 10 ppbv is derived from the measurement with no apparent variation. This shows that CO is less variable with season in the upper troposphere. The seasonal variation of tropospheric CO is largely driven by the seasonal

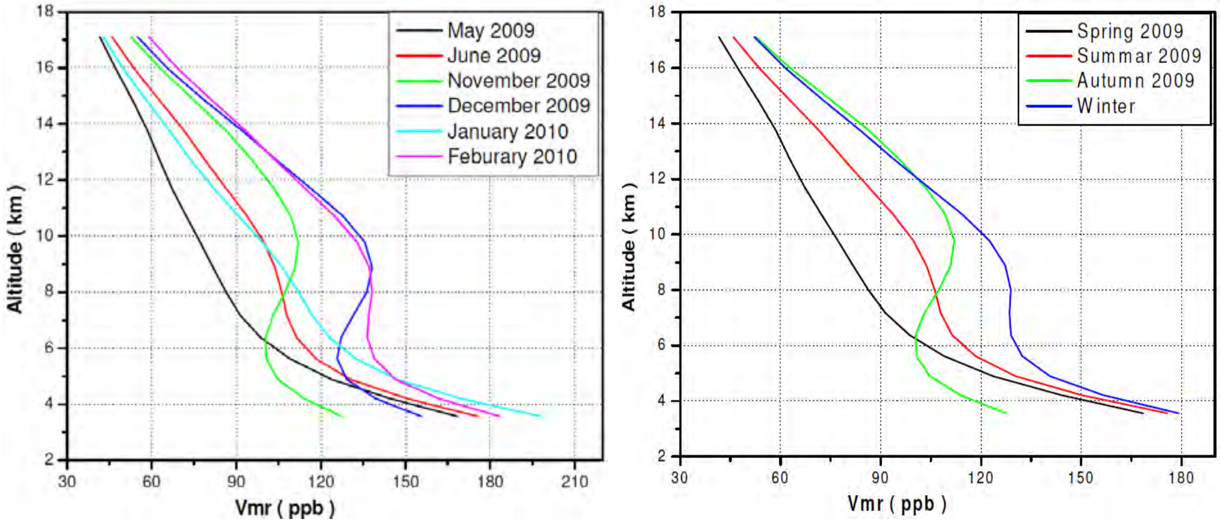

Figure 8.6: Seasonal and monthly variation CO mixing ratio

variation in OH concentration; smaller OH concentration and hence a longer lifetime of CO during winter result in an accumulation of CO toward spring until loss by OH surpasses CO emission and photochemical production. In spring, both photochemical CO destruction and vertical mixing increase. As a result, the CO negative vertical gradient, which is typical for winter - early spring, is transformed into a well mixed atmosphere in late spring - early summer, i.e there is great difference between the mixing ratios of the boundary and the tropopause. During June, the mixing ratio of the entire troposphere has a mean value of ∼99 ppbv. In the absence of additional CO sources, the steady state level could be maintained through the rest of summer until the time when the photochemistry declines and man-made CO begins to accumulate again. However, biomass burning , which usually occur in the dry season, generates plumes containing combustion by-products. These plumes transport enhanced CO to the altitude near to the surface. The lifted parcels of polluted air migrate causing some spikes of CO mixing ratios and enhanced total columns which is to be discussed next.

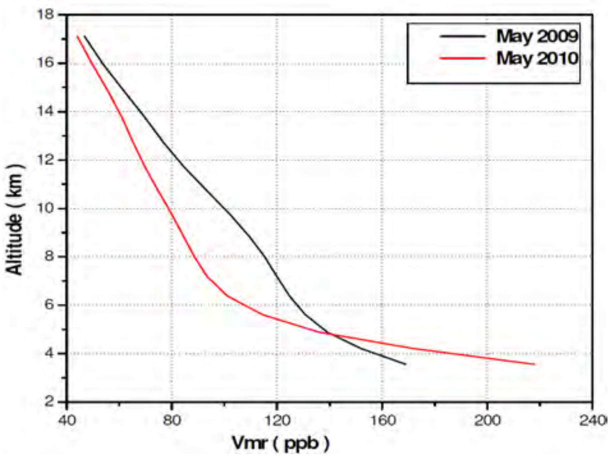

Figure 8.7: Comparison of the profile of CO at the end of May(both 2009 and 2010)

8.4 Inter-annual Variation

At the end of both May 2009 and May 2010, there was a relatively clear sky so that observation were possible during this time. Fig.8.7 shows the comparison between the two in the troposphere. For the altitude up to 4 km, late May 2010 has shown an increased CO mixing ratio with a difference of 50 ppbv in the lower most troposphere. One possible reason for their difference is that there may be a relative increase in anthropogenic emission in May 2010. In addition the mean VMR is dependent up on the time of observation. According to [31], a relative stable atmospheric condition is seen in the morning but increased CO mixing ratio is recorded in the early afternoon-which suggests the effect of vehicle emission during this time. So in May 2010, one of the spectra were measured in the afternoon in search of clear sky. This might have also caused the average CO VMR to be high in the lower troposphere. But the emission is only confined to lower troposphere so that above 4 km CO has a relatively higher VMR for a given tropospheric layer in May 2009.

8.5 Tropospheric Time Series

Monthly and seasonal profile of CO have already been discussed in the preceding section. But the CO profile also varies on inter-daily basis for a given month. Fig.8.8, left shows that the comparison of the vertical profile of CO during the measurement period 04 - 06 January 2010. It can be seen from the figure that the vertical variability is different for different days. So the CO VMR is expected to vary for the rest of days of measurement. Fig.8.8, right shows the evolution of the mixing ratio of CO during the measurement period. In the right panel of Fig.8.8, 49 days of measurement have been included. In the earlier discussion, VMR is compared among months and seasons by averaging the VMR of the measurement days for the corresponding months and seasons. We can also have a look on the mean VMR variation from day-to-day measurement. Comparison among tropospheric layers for all days of measurement is given on Fig.8.9, left and right. The white region (gap) in the plots show days of no measurement due to cloud. The dominant source of CO are the oxidation of CH_4 and other hydrocarbons, biomass burning, and direct anthropogenic emissions. Figs.8.9, left and 8.9, right show that maximum VMR is seen in the lower troposphere for it is near to sources and decreases with altitude for all days. The lower layer has shown maximum VMR (437 ppbv) of all other layers. At present there are no data to estimate the potential contributions of different CO source in Addis Ababa. Although not comprehensive, the list of CO emission includes light and heavy-duty motor vehicles, industry, home heating and cooking, etc. Relative maximum for each layer is seen for those days which belong to the winter season. This season is the dry season when biomass burning rises so that a relative maximum is detected for each layer. Especially, for the reason to be stated later, December 08, 2009 has shown maximum VMR for those layers above 6 km. In contrast, relative minimum VMRs of the layers is observed during the thirty-eighth day (January 21, 2010) of measurement. In general, averaging over all days of measurement, tropospheric CO mixing ratio has a mean

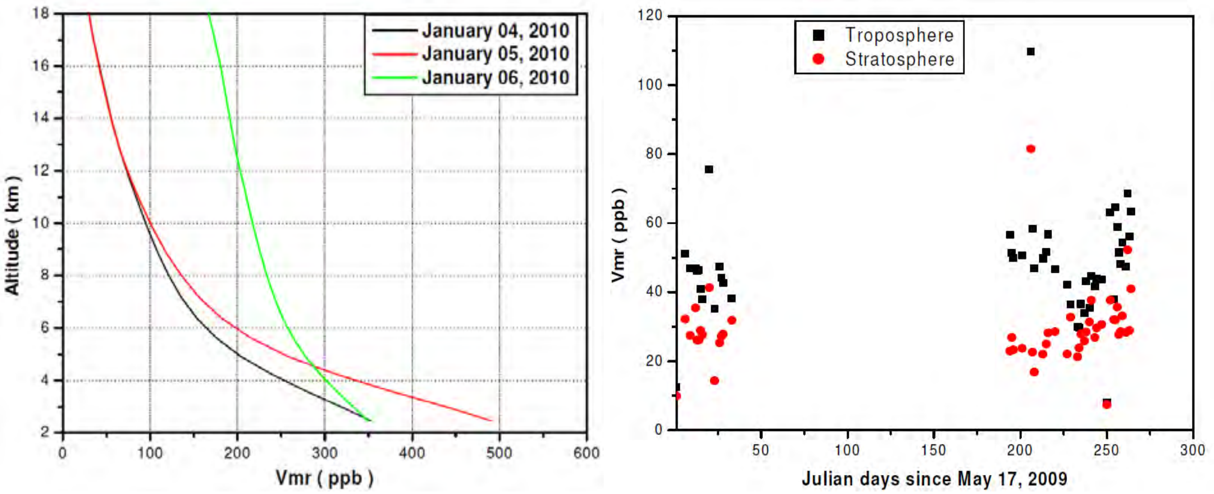

Figure 8.8: Left: tropospheric profile of CO for three days (04 - 06, January 2010). Right: time series of CO mixing ratio in the troposphere and stratosphere

value of 47 ppbv. In addition the variation of VMR is resulted from the variation of the partial column amounts between tropospheric layers. Fig.8.10, left shows the comparison between the partial column of tropospheric layers. Fig.8.10, right shows the partial column for the altitude range of 2.450 - 17.120 km. It indicates that the tropospheric mean CO column amount is ranging from 6.3×10^{17} to $2.8 \times 10^{18} molecules/cm^2$ with a mean value of $1.8 \times 10^{18} molecules/cm^2$. This result can be compared to the partial column amount of different altitude range shown in Fig.8.10, left. We observe from Fig.8.10, left that the partial column amount decreases with altitudes. The partial columns are found to be 37% in the lower troposphere (2 - 5 km) and only 6% for altitude above 14 km indicating that more than 92% is below 14 km.

An intense plume of CO is associated with the savanna burning that takes place in the sub-saharan Africa during December-February period [32]. CO columns are highest during winter (see Fig.8.6, right), indicating the direct effect of biomass burning. In spring (May 2009), savanna fires decrease in intensity due to precipitation (due to deep convection in the source region). In the tropics, CO from biomass burning events can be

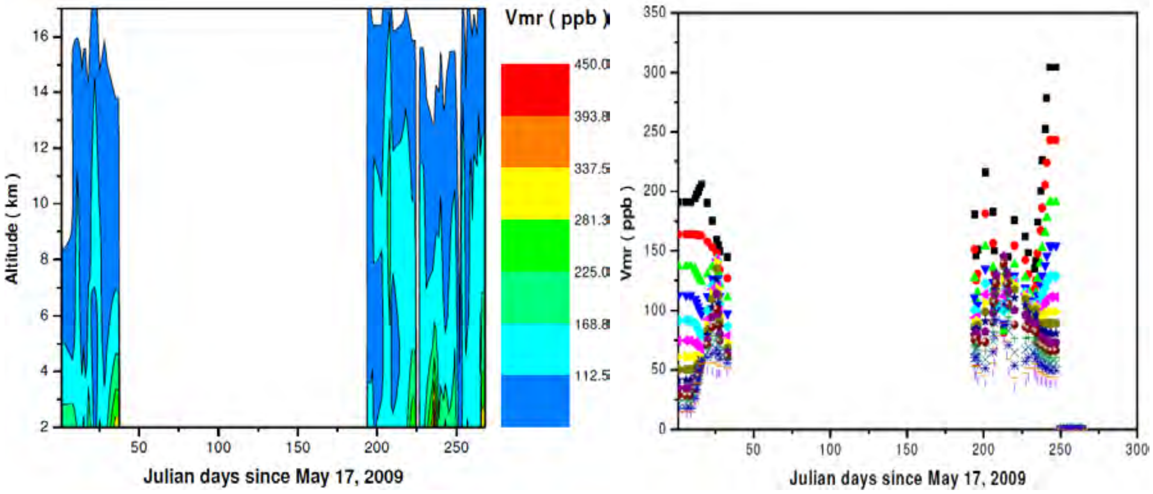

Figure 8.9: Time series of CO mixing ratio in the troposphere (including days of no measurement)

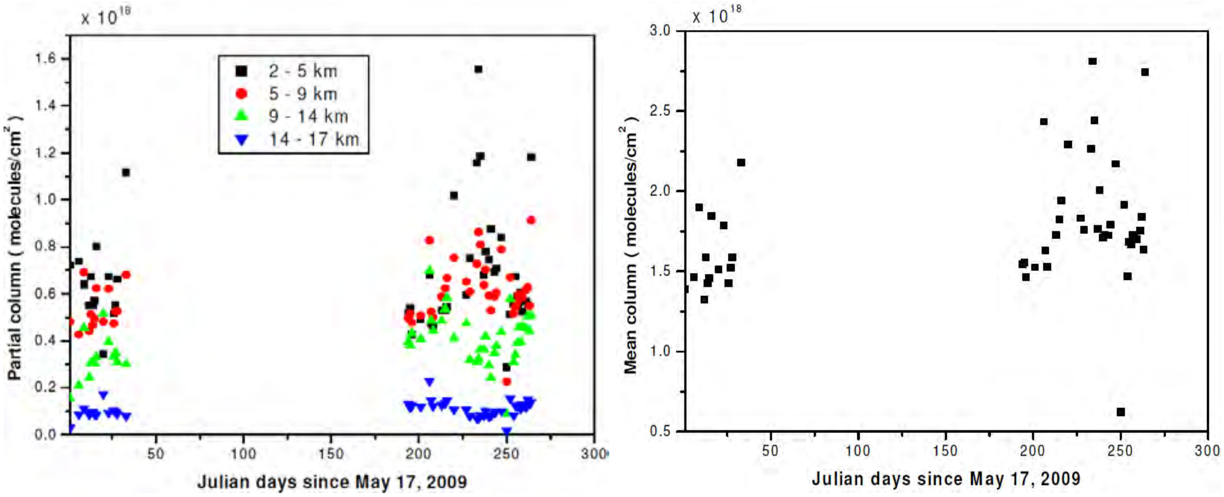

Figure 8.10: Left: comparison of the partial column of some tropospheric layers. Right: time series of the mean column in the troposphere.

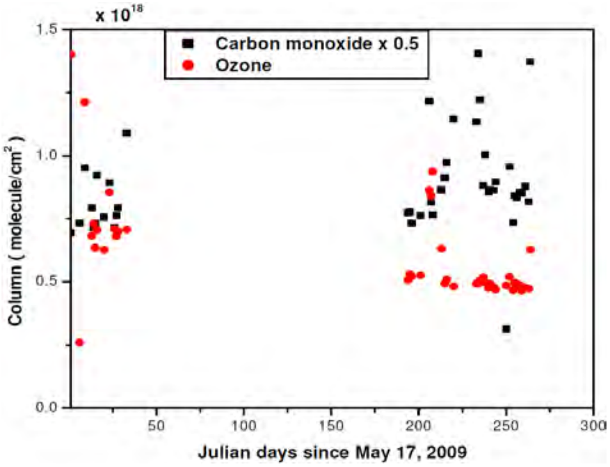

Figure 8.11: Time series of CO and O_3 in the troposphere (up to 15 km)

effectively transported upwards by deep convection and can reach high altitude in the tropical troposphere. The measurement has shown that a relatively elevated ozone column on December 8, 2009, is in phase with the CO peak, indicating the direct effect of biomass burning. During this period the forest fires in the West maximize. High concentration of ozone precursors from these fires are vented into the upper troposphere by deep convection around this period and are then advented into the central part of the country by easterly winds. Fig.8.9, right depicts that in the ninetieth day of measurement, on December 8, 2009, elevated CO were observed during the period of increased biomass burning. Using the fire map obtained from world fire atlas[33], it is shown that there was a biomass burning during the time December 01 - December 08. We performed backward trajectory calculation with Hybrid Single Particle Lagrangian Integrated Trajectory (HYSPLIT) model based on the meteorological data from GDAS, in order to identify the potential source regions of the most pronounced CO plumes observed by the FTIR[34]. The model has shown that the source of the air mass is from the West of Addis Ababa. And thus the possible source of the enhancement of CO seen on December 08 is the addition of the air mass from the West. The CO mixing ratio decreased over the observation period, and reached its lowest value during thirty-eighth day of measurement, January

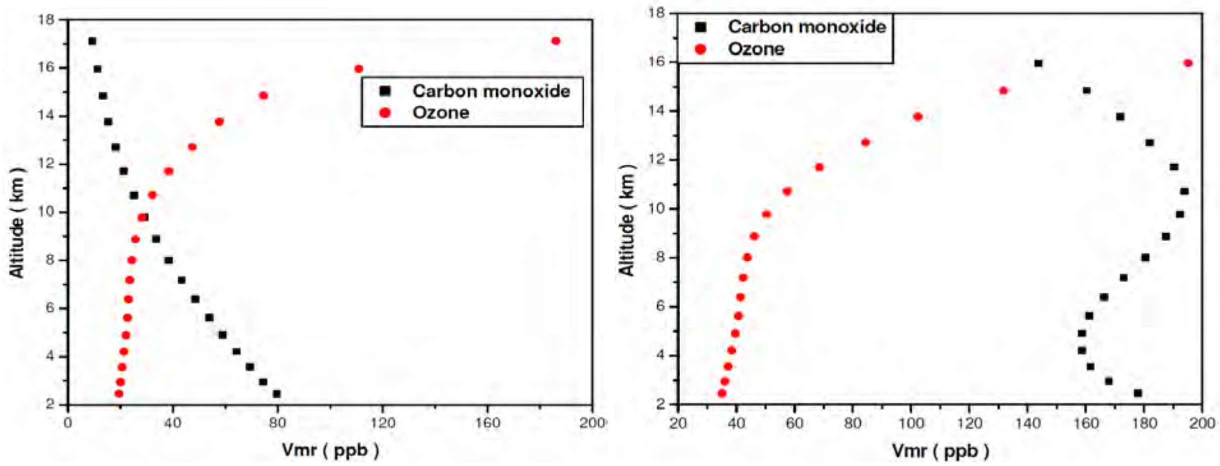

Figure 8.12: Left: anti-correlation between CO and O_3 in the troposphere during enhanced O_3 (January 21, 2010). Right: enhanced CO (December 08, 2009)

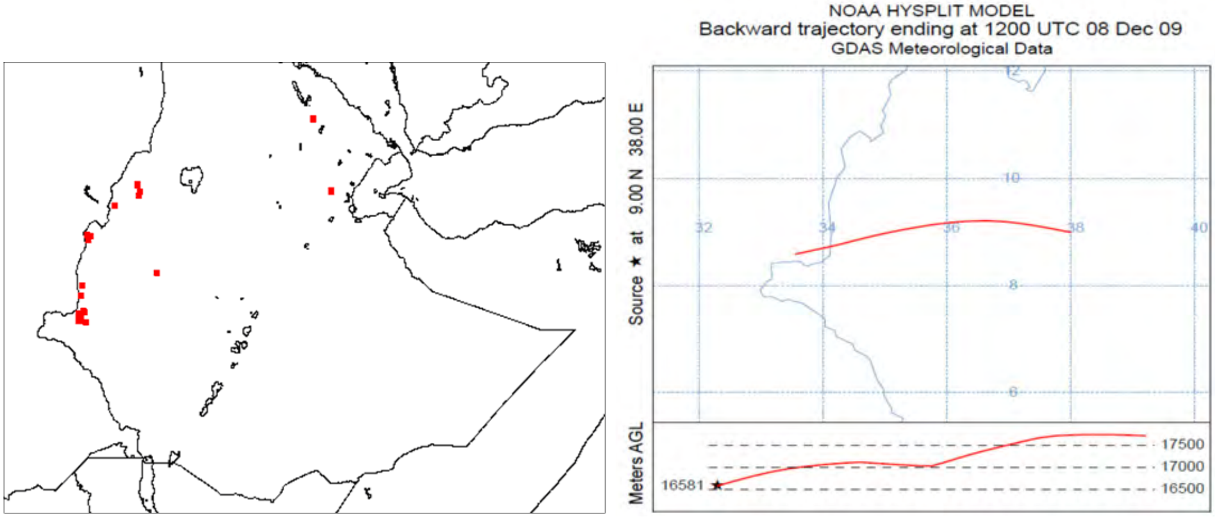

Figure 8.13: Left: biomass burning areas during the period December 01 to December 08, 2009. Right: back trajectory of the air mass for the enhancement observed on December 08, 2009 from NOAA HYSPLIT MODEL.

21, 2010 which is about ∼5 ppbv. It is a clear matter that the variability of CO is affected by stratosphere-troposphere exchange. Stratosphere-troposphere exchange can be identified by the measured O_3 versus CO relation ship because these species are strongly anti-correlated in the upper troposphere as shown in Fig.8.12, right. The O_3 mixing ratio at the tropopause is typically from 10 to 100 ppbv. Pollution and Biomass burning are associated with elevated O_3 and CO, while the background troposphere has relatively little O_3 and CO, so high O_3 (> 150 ppbv) and low CO (< 40 ppbv) uniquely identify stratospheric air in the upper troposphere. Hence, possibly the intrusion of stratospheric air caused the upper troposphere to have elevated O_3 mixing ratio of the day. In addition, the correlation between O_3 and CO shows the production of ozone from its precursor. This causes the decrease CO VMR.

8.6 Seasonal Variation of CO Distribution in the Stratosphere

In February 2010 , it is observed that the lower stratospheric abundance is found to be maximum, reaching 50 ppbv at 18 km. The CO VMR in the lower stratosphere is characterized by a decreasing value with altitude for all months. The vertical variability of CO differs from month-to-month. The lowest CO VMR of 24.3 ppbv is obtained in January 2010 at an altitude around 25 km. The lower stratosphere is relatively well mixed in December 2009 and uniformly mixed in May 2009. The Monthly variation of CO VMR near 25 km is in the range of 1-8 ppbv, indicating less variability with season. Near the tropopause the difference between the VMR among the months is in the range of 0.2-14 ppbv. This indicates that there is a considerable seasonal variation of CO abundance in the lower most stratosphere. Just as the lower stratosphere, mid-stratosphere minimum and maximum CO mixing ratios occurred in January 2010 and February 2010 with values of 24.3 ppbv and 37 ppbv respectively. Seasonal variation of these altitudes show a similar

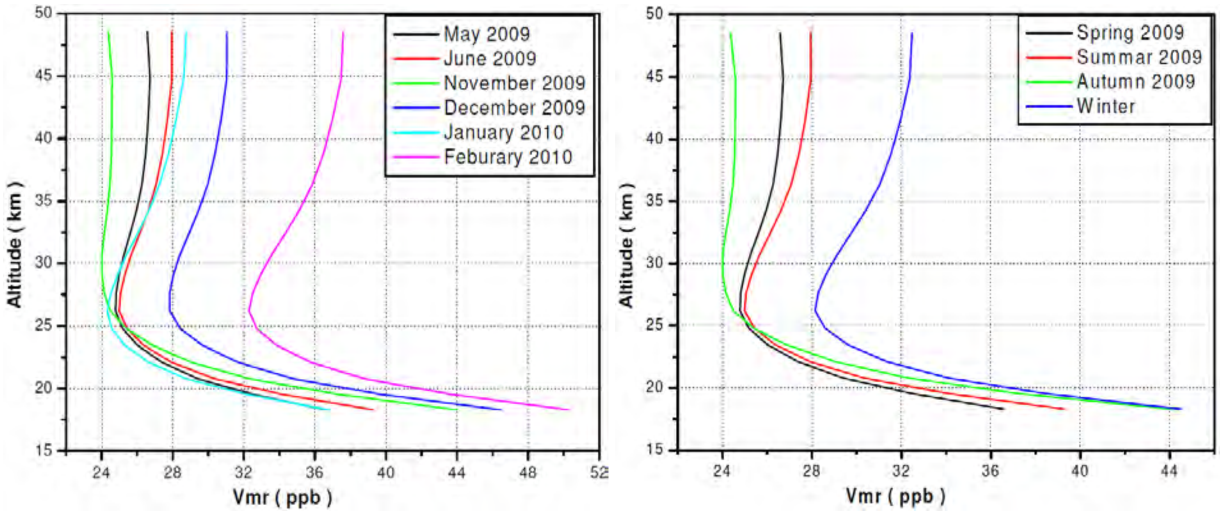

Figure 8.14: Left: monthly averages of CO mixing comparison. Right: seasonal variation of CO mixing ratio

pattern with amplitude difference of less than 13 ppbv. In addition, vertical variability of CO abundance is less for the upper stratosphere. CO is almost uniformly distributed for this altitude range of a given month. The maximum mixing ratio is achieved during the measurement of February 2010, which is ∼ 37 ppbv around 49 km. This CO production is closely linked to a similar production of CH_4, the major chemical source of CO at these altitudes. This value has a difference of nearly 12 ppbv with the maximum obtained in November 2009 and less than 12 ppbv for the other months. And thus there is less monthly variability of CO in the upper stratosphere. In general, tropospheric mean mixing ratio shows that May 2009 value is found to be the lowest (41.6 ppbv) and maximum (58.9 ppbv) in February 2010. In addition, winter has shown the maximum mean VMR (31.8 ppbv). In the stratosphere, minimum (31 ppbv) and maximum (41 ppbv) mean VMR are obtained during the measurement of May 2009 and January 2010, and February 2010 respectively.

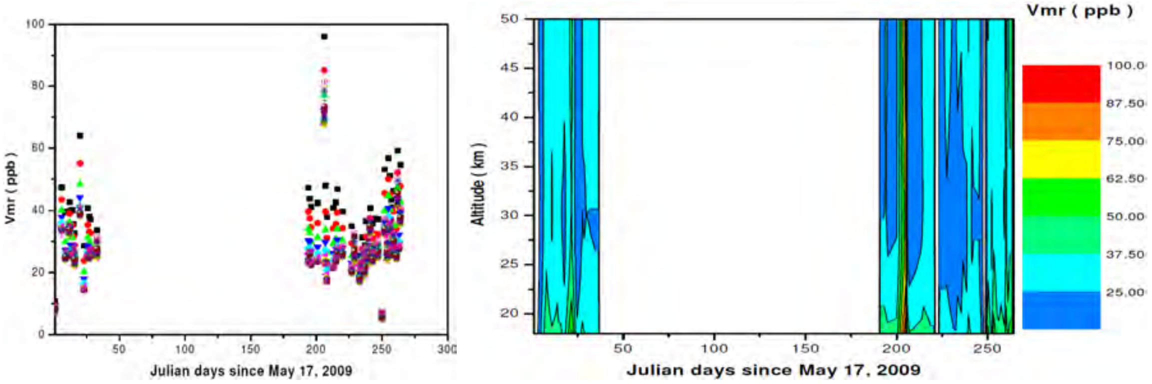

Figure 8.15: Left: time series of CO VMR of stratospheric layers. Right: contour plot of CO mixing ratio in the stratosphere.

8.7 Stratospheric Time Series

It is found that the vertical resolution of the FTIR is weak for the stratosphere and for the reason discussed earlier almost all the column is below the the tropopause. For these reasons detailed discussion of the stratosphere is not presented here. It can be seen that stratospheric CO mixing ratio increased significantly during the ninetieth day of measurement, December 8, 2009. This day has the same effect in the troposphere as explained earlier. But in the stratosphere the possible source of CO are the oxidation of methane and stratosphere-troposphere exchange, i.e there may be intrusion of tropospheric air mass. Using the HYSPLIT model it is determined that there is a convective movement of the air mass at the tropopause. This contributed to the enhancement of CO mixing ratio of the day. The stratospheric mixing ratio of CO is below 52 ppbv for all days of measurement except December 8, 2009 (81 ppbv). The maximum VMR shown on this day can be confirmed from the time series of methane that it is followed by a reduction of CH_4 mixing ratio suggesting methane has also contributed to the enhancement observed on the day. The maximum column amount of CO in the stratosphere is about $12.6 \times 10^{16} molecules/cm^2$. When the total column is compared to the stratosphere, it is found that the stratosphere accounts for less than 5%.

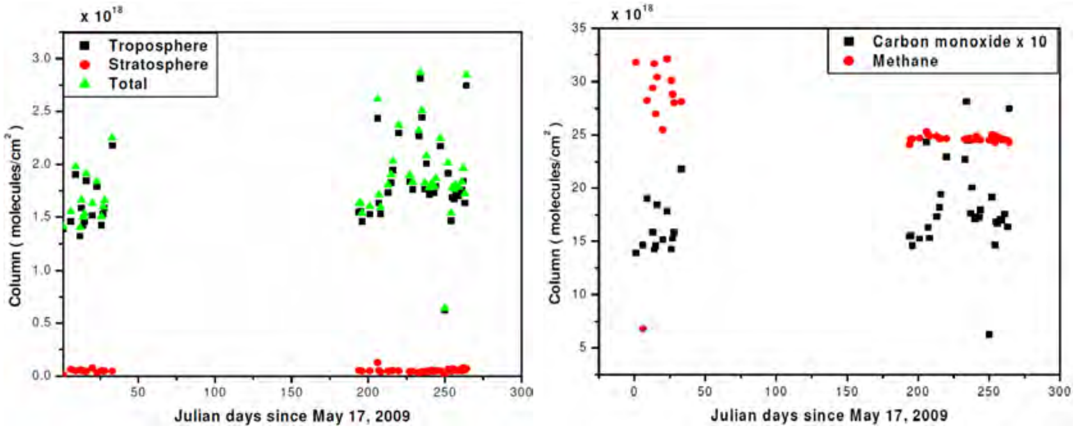

Figure 8.16: Left: comparing the partial column of the troposphere and stratosphere with the total column. Right: time series of CO and CH_4

Chapter 9

CONCLUSION

Tropospheric and stratospheric CO measurements were made using ground-based FTIR spectrometer over Addis Ababa (9.01°N, 38.76°E), Ethiopia. Besides the detection of atmospheric spectra (nearly 49 measurement days), the instrument characteristics were determined regularly (on average about every 15 days). The instrument was found to be well aligned during the whole measurement period. Eventhough it has been given different possible sources of error, the total measurement error is determined to be at a reasonable value which does not affect our result significantly.

The quality of CO vertical profile information extracted from ground-based FTIR observation at Addis Ababa has been demonstrated. The measurements contain ~ 3 independent pieces of information that allow to retrieve the CO abundances in the lower to middle troposphere, in the upper troposphere to lower stratosphere and in the middle to upper stratosphere almost independently.

CO VMR is found to decrease with altitude for all months of measurement. Among others, the vertical variation of the profile of CO is maximum in January 2010 and lowest in November 2009. The effect of intense biomass burning is seen in January 2010. Since CO is a short lived gas, it is expected to vary with season. A seasonal maximum of 179 ppbv in Winter and minimum of 42 ppbv appear in late Spring. The seasonal variation is not much significant in the upper troposphere.

Eventhough it is too early to compare inter annual variation, the measurement allowed us to compare the mean CO VMR of late May 2009 and late May 2010. Accordingly, May 2010 shows a relative increase in the CO VMR with a difference of nearly 50 ppbv in the lower troposphere ($<$ 4km).

Maximum CO VMR is detected in the lower most troposphere reaching 437ppb. Days of winter have a relative maximum of CO VMR. The plume observed on December 08, 2010 is due to the forest fire occurred in the West which is then transported by easterly wind. Stratosphere-troposphere exchange also played a great role of the decreased CO VMR on January 21, 2010. The CO VMR is about 47 ppbv with a corresponding mean partial column of $1.8 \times 10^{18} molecules/cm^2$. More than 92% of CO is located below 14km.

Lower stratospheric CO is less variable while there is considerable variation in the middle and upper stratosphere with month. Stratospheric CO mixing ratio is minimum in May 2009 (41.6ppb) and maximum in February 2010 (58.9ppbv). Winter has shown maximum VMR of 31.8 ppbv.

The stratospheric mixing ratio of CO is below 52 ppbv for all days of measurement except December 8, 2009 (81 ppbv). Time series of CH_4 indicates enhancement of CO. The amount CO present in the stratosphere is less than 5% of the total column.

Bibliography

[1] L.S. Rothman, D. Jacquemart, A. Barbe, D. Chris Benner, M. Birk, L.R. Brown, M.R. Carleer, C. Chackerian Jr., K. Chance, L.H. Coudert, V. Dana, V.M. Devi, J.M. Flaud, R.R. Gamache, A. Goldman, J.M. Hartmann, K.W. Jucks, A.G. Maki, J.Y. Mandin, S.T. Massie, J. Orphal, A. Perrin, C.P. Rinsland, M.A.H. Smith, J. Tennyson, R.N. Tolchenov, R.A. Toth, J. Vander Auwera, P. Varanasi, G. Wagner, *The HITRAN 2004 molecular spectroscopic database*, Elsevier Ltd., 96, 139 to 204, 2005.

[2] H.Israël and G.W.Israël, Trace elements in the atmosphere, Ann Arbor Science, 1974.

[3] Deltev Moller, *Atmospheric Environment Research*, Springer-Verlag Berlin Heidelberg, 1999.

[4] Thomas G.Spiro and William M.Stigliani, *Chemistry of the environment*, Prentice Hall, 2002.

[5] NDACC, *Network for the Detection of Atmospheric Composition and Change*, http://www.ndacc.org/.

[6] N.H. March, *New ground-based FTIR measurements at Ile de La Reunion: observations, error analysis, and comparisons with independent data*, ACP, 8, 3483 to 3508, 2008.

[7] Kshudiram Saha, *The Earths Atmosphere: Its Physics and Dynamics*, Springer- Verlag Berlin Heidelberg, 2008.

[8] John Marshall and Alan Plumb, *Circulation of the Atmosphere and Ocean: an introductory text*, Massachusetts Institute of Technology, 2006.

[9] B.A.Thrush and F.R.S., *The Chemistry of the stratosphere*, A 296, 149, 1980.

[10] O.Badr and S.D.Probert, *Sinks and Environmental Impacts for Atmospheric Carbon Monoxide*, Applied energy, 50, 339 to 372, 1995.

[11] John A. Taylor, Patrick R. Zimmerman b David J. Erickson III, *A 3-D modelling study of the sources and sinks of atmospheric carbon monoxide*, Elsevier, 88, 1996, 53 to 71.

[12] R. L. Herman, C. R. Webster, R. D. May, D. C. Scott, H. Hu, E. J Moyer, P. O. Wennberg, T. F. Hanisco, E. J. Lanzendorf, R. J. Salawitch, Y. L. Yung, J. J. Margitan and T. P. Bui, *Measurements of CO in the upper troposphere and lower stratosphere*, Elsevier Science Ltd, 1, 173 to 183, 1999.

[13] J.K. Jain, *Fundamentals of Molecular Spectroscopy, second edition*,McGraw-Hill Book Company, UK, 1972.

[14] G.M.Barrow, *Introduction to Molecular Spectroscopy*, McGraw-Hill Book Company, University of California, 1962.

[15] K. N. Liou, *An Introduction to Atmospheric Radiation Second Edition*, Elsevier Science, 2002.

[16] Lars-Erik Ȧmand and Claes J. Tullin, *The Theory Behind FTIR analysis*, Department of Energy Conversion Chalmers University of Technology Gȯteborg, Sweden, 1996.

[17] Siegfried Wartewig, *IR and Raman Spectroscopy*, WILEY-VCH GmbH and Co. KGaA, 2003.

[18] P.Griffiths and de Haseth, *Fourier Transform Infrared Spectrometer*, John Wiley and Sons, 1986.

[19] NASA's Goddard Space Flight Center, *http://www.nasa.gov/centers/goddard*.

[20] David A. Naylor and Margaret K. Tahic, *Apodizing functions for Fourier transform spectroscopy*, J. Opt. Soc. Am. A, Vol. 24, No. 11, November 2007.

[21] Margaret K. Tahic and David A. Naylor, *Apodization Functions for Fourier Transform Spectroscopy*, Optical Society of America, 2005.

[22] Jyrki Kauppinen and Jari Partanen, *Fourier Transforms in Spectroscopy*, Wiley-VCH Verlag GmbH, 2001.

[23] HAMAMATSU, *Characterization and use of infrared detectors*, http://www.hamamatsu.com.

[24] Mikko Ahro, Jyrki Kauppinen, and Ilkka Salomaa, *Detection and correction of instrumental line-shape distortions in Fourier spectroscopy*, APPLIED OPTICS by Vol. 39, No. 33 by 20 November 2000.

[25] H. Fischer, M. Birk, C. Blom, B. Carli, M. Carlotti, T. von Clarmann, L. Delbouille, A. Dudhia, D. Ehhalt, M. Endemann, J. M. Flaud, R. Gessner, A. Kleinert, R. Koopman, J. Langen, M. Lopez-Puertas, P. Mosner, H. Nett, H. Oelhaf, G. Perron, J. Remedios, M. Ridolfi, G. Stiller, and R. Zander, *MIPAS: an instrument for atmospheric and climate research*, ACP, 8, 2151 to 2188, 2008.

[26] F. Hase, J.W. Hannigan, M.T. Co1ey, A. Goldman, M. Höpfner, N.B. Jones, C.P. Rinsland, S.W. Wood, *Intercomparison of retrieval codes used for the analysis of high-resolution, ground-based FTIR measurements*, Elsevier Ltd., 87, 25 to 52, 2004.

[27] Frank Hase, Thomas Blumenstock, and Clare Paton-Walsh, *Analysis of the instrumental line shape of high-resolution Fourier transform IR spectrometers with gas cell measurements and new retrieval software*, Optical Society of America, 1999.

[28] Justus Notholt Geoff Toon, Nicholas Jones, David Griffith, Thorsten Warnekea, *Spectral line finding program for atmospheric remote sensing using full radiation transfer*, Elsevier, 97, 112 to 125, 2006.

[29] Clive D.Rodgers, *Inverse methods for atmospheric sounding*, World Scientific Publishing Co Ltd., 2000.

[30] Matthias Schnieder, *Continuous Observation of Atmospheric Trace Gases by Ground-based FTIR Spectroscopy at Izaña Observatory, Tenerife Island*, Forschungszentrum Karlsruhe GmbH, Karlsruhe, 2002.

[31] V. Etyemezian, M. Tesfaye, A. Yimer, J.C. Chow, D. Mesfin, T. Nega, G. Nikolich, J.G. Watson, M. Wondmagegn, *Results from a pilot-scale air quality study in Addis Ababa, Ethiopia*, Atmospheric Environment, 39, 7849 to 7860, 2005.

[32] Crutzen, P. J. and G. R. Carmichael, *Modeling the influence of fires on atmospheric chemistry, Fire in the Environment*, pp. 89-106, John Wiley, New York, 1993.

[33] ASTR world fire atlas, *wfaa-dat.esrin.esa.int.*

[34] HYSPLIT - Hybrid Single Particle Lagrangian Integrated Trajectory Model, http://www.ready.arl.noaa.gov.

Declaration

This thesis is my original work, has not been presented for a degree in any other University and that all the sources of material used for the thesis have been dully acknowledged.

Name: Gezahegn Sufa

Signature:

Place and time of submission: Addis Ababa University, July 2010

This thesis has been submitted for examination with my approval as University advisor.

Name: Dr. Gizaw Mengistu

Signature: